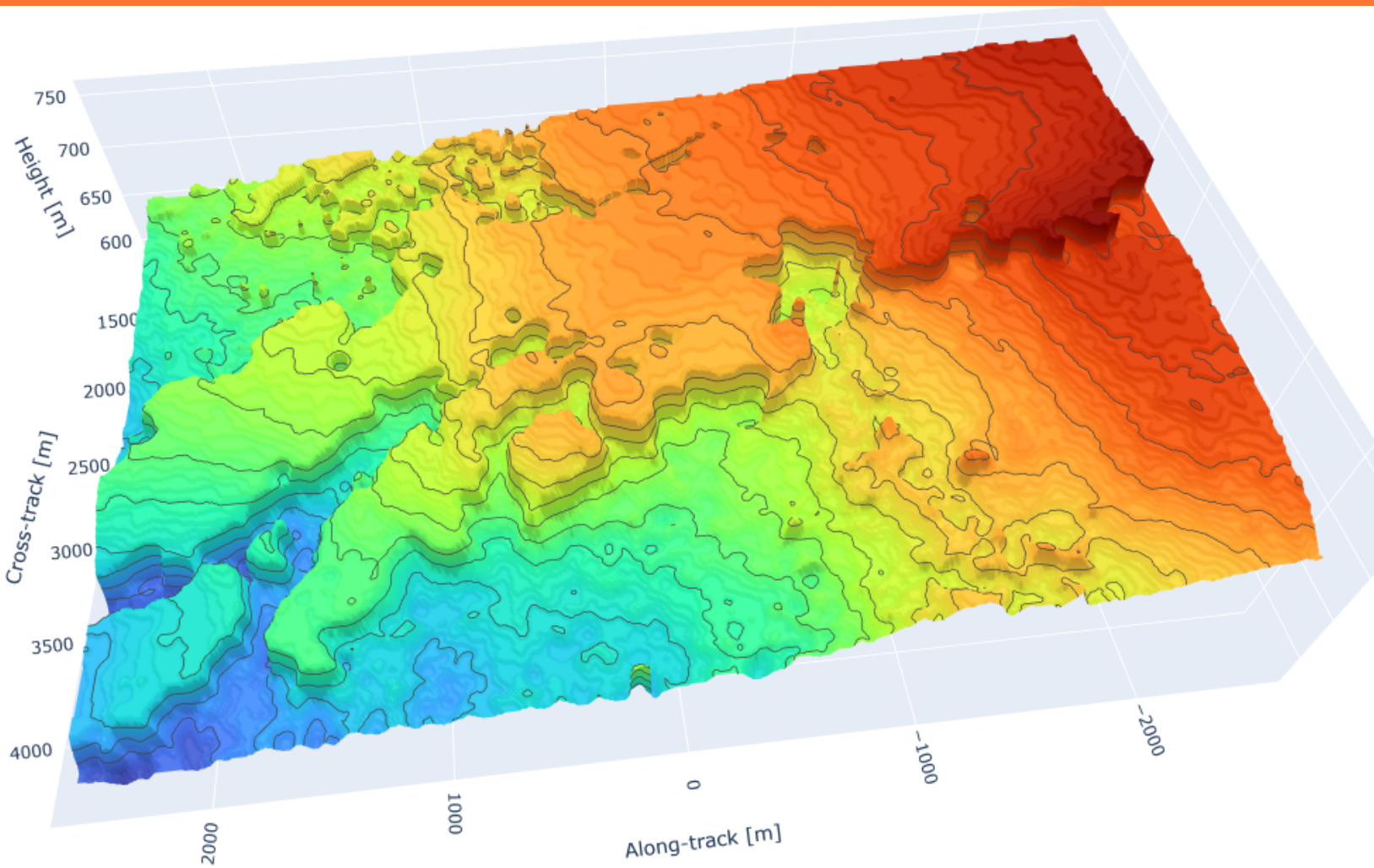


Tomographic SAR Mapping of Ice Sheets



Authors:

Niels Peter Kierkegaard Christensen, Gustav Troelsen Vindeløv, Julius Gräs Kokholm

Authors:

Julius Gräs Kokholm, (s203984)
Niels Peter Kirkegaard Christensen, (s203980)
Gustav Troelsen Vindeløv, (s183822)

DTU Space

December 2024

Title:

Tomographic SAR Mapping of Ice Sheets

Special course

ECTS: 10

Title image:

Height of deepest signal in meters above the ellipsoid using the MUSIC spectral estimator. Generated using the segmentation employed in section 4.9. Illustrative of the general scattering dynamics of the scene. The colormap illustrates height and not signal power.

Education: Master of Science

Supervisor:

Jørgen Dall

DTU Space

Remarks:

This report is submitted as partial fulfillment of the requirements for graduation in the above education at the Technical University of Denmark. This project replaces 30220 for s203984 and s203980.

Technical University of Denmark DTU Space

Elektrovej building 327
2800 Kongens Lyngby
Denmark

Abstract

In this report we present the implementation of a tomographic synthetic aperture radar (TomoSAR) processor for mapping ice sheets. The processing chain includes azimuth focusing via the Direct Back-Projection (DBP) algorithm, phase calibration through an iterative Phase Center Double Localization (PSDL) algorithm, and tomographic focusing with three different spectral estimators to form tomographic cubes. The spectral estimators used are Fourier beamforming, Capon and MUltiple SIgnal Classification (MUSIC); the first two are non-parametric estimators and the latter two are super-resolution estimators.

We have tested our TomoSAR processor on SAR data from May 7 2012 acquired during the European Space Agency (ESA) IceSAR 2012 campaign in Greenland, near Kangerlussuaq. This data was collected by the Technical University of Denmark (DTU) using the P-band POLarimetric Airborne Radar Ice Sounder (POLARIS) SAR instrument, and is provided as level 0c data.

We have analyses the resulting tomograms in multiple ways, including: phase screens caused by sensor position errors, the interferometric phase and coherence and the underlying scattering mechanics affecting them, and the influence of non-evenly distributed flight tracks on beam patterns and vertical resolution. It is found that phase calibration is a central component to achieve correct tomograms in terms of absolute height, while the flight tracks significantly influence the vertical resolution. Tomographic sections and the maximum penetration depth from within the ice sheet are also investigated. With this, the imaged scene is characterized in terms of the amount of surface and volume backscatter from different regions, and this is used to identify two interesting subsurface features. This allow us to compare our findings with results from pre-existing tomograms of the same location found in published literature. We argue that our implementation is able to produce suitable tomograms from the data in question, and show that our results agree with those in the literature, to within an error explained by differences in implementation choices.

Contents

Introduction	1
1 Theory	2
1.1 SAR acquisition geometry and imaging considerations	2
1.1.1 SAR geometry	2
1.1.2 Speckle	3
1.1.3 SCH coordinate system	4
1.2 Single- and multi-baseline SAR imaging	6
1.2.1 SAR Interferometry	6
1.2.1.1 Covariance and coherence	7
1.2.2 Tomographic SAR	9
1.2.2.1 Multi-baseline signal model and phase contributions	9
1.2.2.2 TomoSAR focusing	11
1.3 Scattering dynamics and penetration	15
1.4 Phase calibration	16
1.4.1 Problem formulation and geometry	16
1.4.2 Phase linking	17
1.4.3 Double localization algorithm	18
2 Introduction to the data	20
2.1 The POLARIS instrument	21
2.2 TanDEM-X	23
3 Algorithm implementation and processing chain	25
3.1 DC filtering	26
3.2 Azimuth focusing and co-registration via DBP	28
3.3 Coherent combination of SLC images	30
3.4 Phase calibration via iterative PCDL algorithm	31
3.4.1 Optimization strategy	32
3.4.2 Validation on simulated data	32
3.4.2.1 Point targets	33
3.4.2.2 Simulated distributed target	34
3.4.3 Parameter for PCDL phase calibration of real data	35
3.5 Tomographic processing	36
4 Results and comparison	37
4.1 Refraction	37
4.2 The scene	37
4.3 Phase calibration of real data	38
4.4 Coherence and interferometric phase	40
4.5 Simulated tomograms	42
4.6 Vertical resolution and super-resolution techniques	43

4.7	Tomographic sections	46
4.8	Feature analysis	49
4.9	Scattering depth and deepest return	52
4.10	Future Works	54
5	Conclusion	58
	References	60
A	SCH Coordinate Conversions	61
A.1	SCH to ECEF	61
A.2	ECEF to SCH	62

Introduction

The scientific community has recorded evidence of unprecedented melting of ice sheets [1]. The investigation of the characteristics of ice sheets in terms of structure and dynamic processes is of fundamental importance to understand their changes and gain information about their interrelation with dramatic environmental processes such as climatic changes and sea level rise. Radio-glaciology is a very important discipline that aims at inferring this kind of information through the use of microwave remote sensing.

Synthetic Aperture Radar (SAR) represents a major tool for studying the ice layers, since it provides a dense temporal and large spatial coverage and is ideal for all kinds of weather. Additionally, the employment of SAR reduce the necessity of carrying out expensive in situ campaigns, which are also limited in terms of spatial resolution. These qualities make SAR useful for investigate the arctic and antarctic ice sheets, including their interactions with past climatic events[2].

SAR processing of ice sounding data is presently a standard technology for this type of investigations. With ice sounders, an image of the strata of glacier subsurface along the flight transect can be obtained by operating a very low frequency airborne nadir-looking radar and measure the specular reflections from low altitude (typically few hundreds of meters) over the glacier surface. In this way, very deep strata like the bedrock can be imaged, and the thickness of the various layers can be estimated. Surface clutter masking the signal of interest is still a major obstacle although it can be reduced by flying low. Moreover, the coverage is quite limited due to the nadir-looking mapping geometry and the low flight altitude[3].

Side-looking SAR measurements are complementary to ice sounders. Long wavelength SAR and ice sounders are both capable of measuring return signals from the internal structure of the illuminated medium. They differ in that ice sounders measure specular reflection from a nadir-looking geometry, while SAR measures backscatter from a side-looking geometry.

The forthcoming Earth Explorer mission BIOMASS, selected in May 2013 by the European Space Agency (ESA), represents a very important opportunity for future cryospheric investigations, due to the potential of P-band SAR to penetrate the illuminated medium. The IceSAR 2012 campaign, performed in the framework of BIOMASS studies, was conceived to investigate the capabilities of P-band SAR of providing suitable products of ice flow and subsurface structure. In this paper, the focus is on the use of multi-baseline data collected during IceSAR 2012 to investigating ice subsurface structure using multi-baseline SAR tomography (TomoSAR) techniques, comparing different imaging approaches, and presenting the main results. TomoSAR is a step further in interferometric processing and can be regarded as a tool to directly see into the 3-D structure of a scene. With more than two acquisitions of the same scene from slightly different views, different vertical wavenumbers of the object under investigation are measured. The backscatter profile of the scene in the vertical direction and SAR multi-baseline data form a Fourier pair, and the former can be reconstructed by using spectral estimation techniques[4].

In this work, a tomographic SAR processor has been implemented, tested, and compared to exiting results from the same dataset for validation purposes. The report is structured as follows. In the section *Theory* the relevant theory used to make a TomoSAR processor is described. In the section *Introduction to the data* the datasets are explained as well as how they are made. In the section *Algorithm implementation and processing chain* goes into depth in technical explanations and choices made in the creation of the the TomoSAR processor. In the section *Results and comparison* the different products that the TomoSAR processor can produce is described and compared to previous made TomoSAR processors. In the section *Conclusion* the main points of this report is summarized and an outlook on future works is discussed.

Chapter 1

Theory

1.1 SAR acquisition geometry and imaging considerations

1.1.1 SAR geometry

In this chapter, the general SAR acquisition geometry will be described in order to lay a basis for the multi-baseline techniques presented later.

Assume that a radar moves along a straight line at an altitude H as showed in Figure 1.1. The flight trajectory is defined as x or azimuth and is referred to as the along-track direction. The radar looks sideways in the cross-track direction. By emitting pulses in this direction and sampling the returning ground echo at a frequency of f_s , the radar can measure the response from individual range cells on the ground for that particular location along the trajectory. As the SAR moves along its trajectory, it will emit these pulses at a repetition frequency of f_{PRF} , thus scanning the terrain as it moves by.

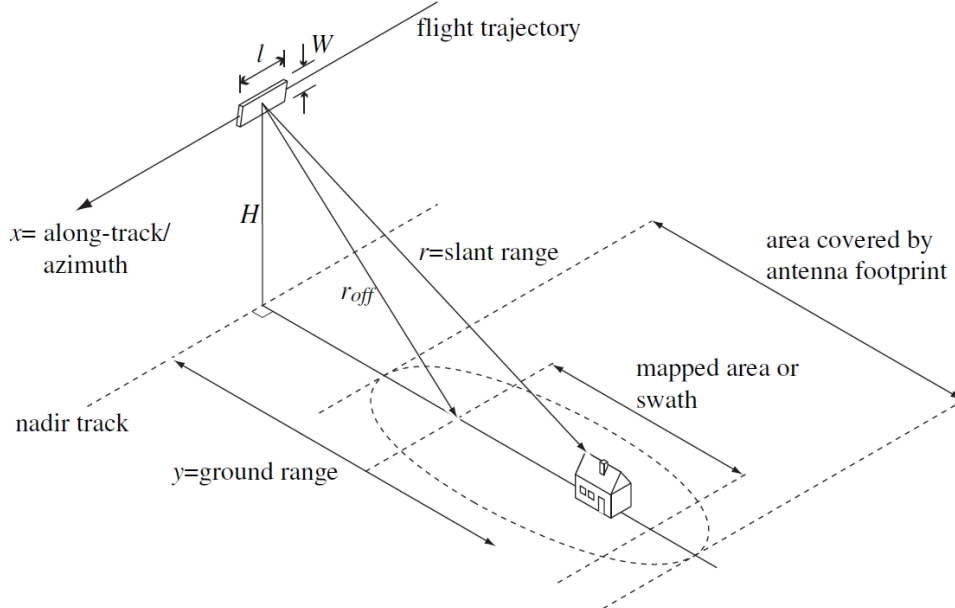


Figure 1.1: The geometry for taking SAR images.[5]

An image can be generated from the received echoes, spanning two coordinates; range, r , and azimuth, x . Each pixel of the image contains the measured signal from a particular range cells at a particular point

along the trajectory. The mapping from real world objects to raw SAR image is shown in Figure 1.2. The separation between pixels in each direction, range and azimuth, is referred to as the range spacing, dR , and azimuth spacing, dAz , respectively.

It should be noted that a radar does not measure range directly, but instead the time delay, which is related through

$$r = \frac{1}{2}c\Delta t \quad (1.1)$$

Here, c denotes the speed of light and Δt is the time delay of the echo. This means that we have a time signal in range, since echoes from objects far away return later than from objects closer to the radar.

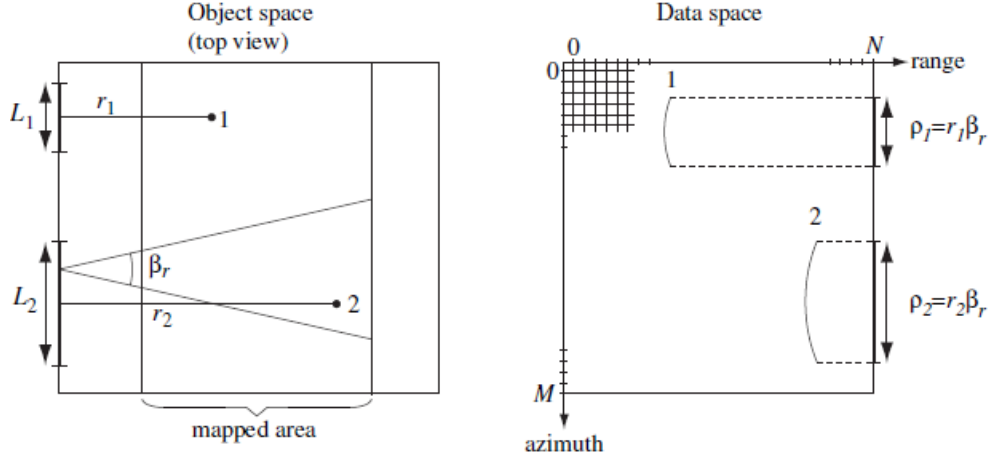


Figure 1.2: Relation between the real world (object space) and the raw image (data space).[5]

The resolution in range is given by the pulse length, τ , as

$$\rho_r = \frac{c}{2B} \quad (1.2)$$

where B is the pulse bandwidth, which is $1/\tau$ for a simple sinusoidal pulse. The resolution can be improved via digital pulse compression by applying a frequency modulation to the transmitted pulse, thus increasing the bandwidth.

For a single pulse, the azimuth resolution is given by

$$\rho_{az} = \frac{\lambda}{l}r \quad (1.3)$$

where r is the range, and $\beta \approx \frac{\lambda}{l}$ is the antenna beam width given by the physical length of the antenna, l , and the carrier wavelength, λ . This is the resolution for a regular side-looking aperture radar (SLAR) also referred to as real aperture radar. But as the name suggests, SAR utilizes a synthetic aperture formed by combining the phase information from multiple different pulses, such that it obtains a synthetic antenna of length L . Each pulse is separated in time, so processing must be applied to combine the echoes coherently.

1.1.2 Speckle

A phenomenon native to SAR imagery is that of speckle. It appears in SAR images as granular noise, and is due to the interference of waves reflected from many elementary scatterers.

When a radar illuminates a surface that is rough on a scale of radar wavelengths, the return signal consists of waves backscattered from many elementary scatterers within the scene. The waves received by the SAR from these individual scatterers, although coherent in frequency, are no longer coherent in phase. Instead,

the received signal is the coherent sum of waves from all elementary scatterers within the resolution cell. A strong signal is received if the waves interfere constructively, and a weak signal if the waves are out of phase. The concept of coherently summing these scattering signals is illustrated in Figure 1.3, where X and Y denote the real and imaginary part of the resulting complex signal, while R and ϕ_b is the amplitude and phase of the same signal.

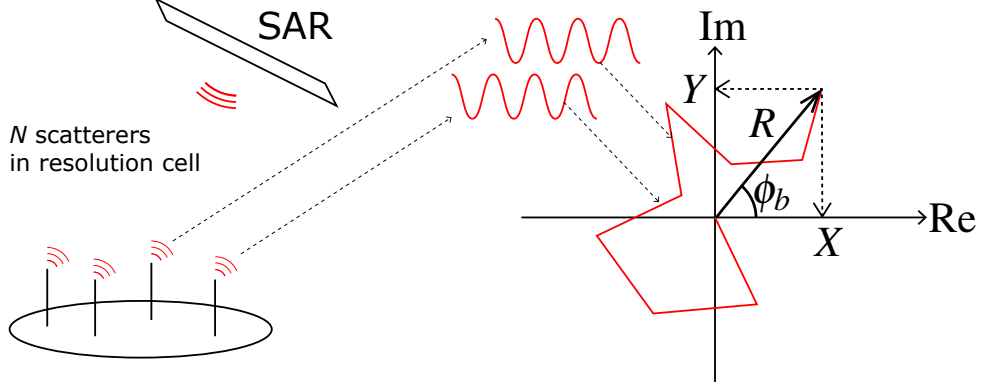


Figure 1.3: Illustration of coherent sum of scatterers from SAR resolution cell. Each elementary scatterer contributes with a (statistically) random phase to the combined received signal. Figure inspired by [6].

Speckle introduces a pixel-to-pixel variation in SAR images, even if the image is acquired over a seemingly homogeneous region. This variation does, however, have specific statistical properties if the following assumptions hold

1. The phase contribution from each elementary scatterer is independent and uniformly distributed between $0-2\pi$.
2. For each elementary scatterer the magnitude and the phase is uncorrelated.
3. The total number of scatterers, N , within the resolution cell is large.
4. No dominant scatterer is present in the image.

In particular, the backscattered signal $s = X + jY = R \exp(j\phi_b)$ follows a circular symmetric complex Gaussian distribution. The amplitude $|s|$ is Rayleigh distributed, the intensity $|s|^2$ is exponentially distributed, while the phase $\angle s$ is uniformly distributed between 0 and 2π . [6]

This pixel-to-pixel intensity variation in SAR images has a number of consequences, the most obvious one being that the use of a single pixel intensity value as a measure of target's reflectivity would be erroneous. This is also the reason why speckle is defined as a noise-like influence, though it is not actual noise.

A common approach to reduce speckle is to average several independent estimates of the image. This is referred to as multi-looking. Spatial multi-looking is done by averaging L independent pixels in the same neighborhood. The L -look processing reduces the standard deviation of speckle by a factor of \sqrt{L} , but at the expense of resolution. The intensity $|g|^2$ of the multilooked image follows a gamma distribution.

1.1.3 SCH coordinate system

In the above section, the general SAR geometry has been presented in the native range-azimuth coordinate system of the radar, however in this work the more convenient SCH-coordinate system will be employed. Spherical Cross-track Height (SCH) coordinates, or radar mapping coordinates, is a curvilinear spherical coordinate system that best approximates the ellipsoid in the along track direction of the radar platform. The coordinate system is easily referenced to geocentric or geographic coordinates and it provides a convenient

and accurate way to parameterize the flight path by distance along the reference path. As shown in Figure 1.4 the S - and C -coordinates are the along-track, following the locally approximated ellipsoid, and cross-track positions, respectively, while H is the corresponding height above the ellipsoid. The origin is defined at some geographic reference location¹, (θ_0, λ_0) , and the orientation of the S -axis is specified by the reference heading, η_0 , with respect to the local north at the reference location.

The SCH system is useful since coordinates are related to the ellipsoid, and thus account for Earth's curvature. On the flip side, the SCH system is not rectangular, and thus ranges and angles can only be calculated after converting to a rectangular system. A convenient rectangular system is the local tangential plane or, as referred to in this work, the intermediate coordinate system denoted (x', y', z') , which is given by

$$\begin{bmatrix} x' \\ y' \\ z' \end{bmatrix} = \begin{bmatrix} (R_a + H) \cos\left(\frac{C}{R_a}\right) \cos\left(\frac{S}{R_a}\right) \\ (R_a + H) \cos\left(\frac{C}{R_a}\right) \sin\left(\frac{S}{R_a}\right) \\ (R_a + H) \sin\left(\frac{C}{R_a}\right) \end{bmatrix} \quad (1.4)$$

where (S, C, H) are the mapping coordinates and R_a is the radius of curvature of the ellipsoid at the reference location in the heading direction, given by the Euler curvature

$$R_a = \frac{R_N(\lambda_0) R_M(\lambda_0)}{R_N(\lambda_0) \cos^2(\eta_0) + R_M(\lambda_0) \sin^2(\eta_0)} \quad (1.5)$$

with $R_N(\cdot)$ and $R_M(\cdot)$ being the radius of curvature in the prime vertical and in the meridian, respectively. A detailed description of SCH coordinates are given in [7], and transformations between SCH coordinates and Earth-Centered, Earth-Fixed (ECEF) coordinates are included in Appendix A.

In addition to the SCH to/from ECEF transformations, we also convert between ECEF and geographic (θ, λ, h) -coordinates, but such transformations are not described in this work, as they are considered rudimentary.

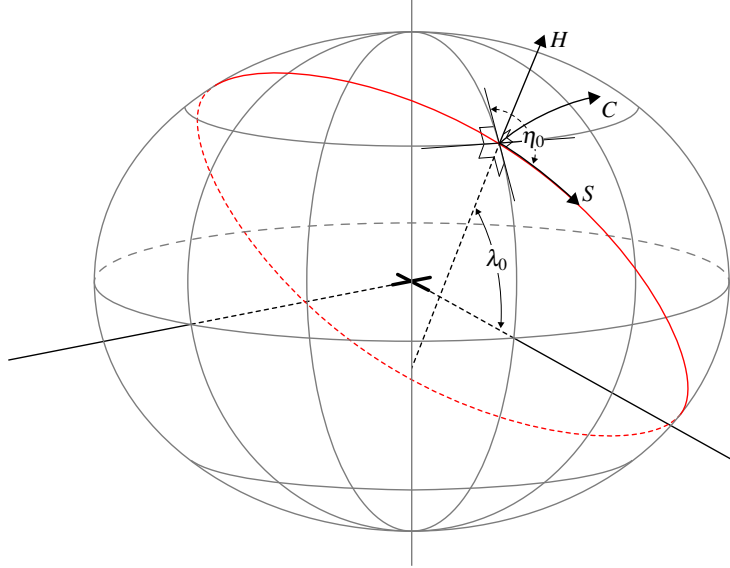


Figure 1.4: The SCH coordinate system defined in relation to the ellipsoid. The origin of the coordinate system is given by a geographic reference location, (θ_0, λ_0) , and the orientation is determined by the reference heading, η_0 , with respect to the local north at the reference location.

¹The notation used for latitude and longitude varies in scientific literature. In this section, we use the naming convention found in [7], meaning θ denotes the geographic longitude, and λ denotes the geographic latitude.

1.2 Single- and multi-baseline SAR imaging

While individual SAR acquisitions can be used to generate images from the return signal (often referred to a single-look complex (SLC) images), addition information can be extracted by combining the signals obtained from two or more acquisitions. This is referred to as single-baseline SAR interferometry (InSAR) or multi-baseline InSAR (MB-InSAR). The following section will introduce the guiding principles of InSAR for the simplest case with one baseline. Following that, the application of MB-InSAR for tomography is described in detail.

1.2.1 SAR Interferometry

Every pixel in a SLC image represents a complex signal with an amplitude and a phase term. Consider now two corresponding pixels between SLC images acquired from two different acquisitions (different in time and space), and let the complex value of these two pixels be expressed as s_1 and s_2 . An interferogram can be formed by combining the two signals

$$s_{\text{int}} = s_1 s_2^* = |s_1 s_2^*| \exp(j\phi_{\text{int}}) \quad (1.6)$$

where $|\cdot|$ is the modulus, $*$ is the complex conjugate, j is the imaginary unit, and ϕ_{int} is the interferometric phase. The interferometric phase can be related to surface topography and deformation, but it also contains other phase contributions. A general expression for the interferometric phase is

$$\phi_{\text{int}} = \left[-\frac{4\pi}{\lambda} (R_0^1 - R_0^2) - \underbrace{2\pi f_c (\tau_{\text{atmo}}^1 - \tau_{\text{atmo}}^2)}_{\phi_{\text{atmo}}} + \underbrace{\phi_b^1 + \phi_b^2}_{\phi_{\text{decorr}}} \right] \text{mod } 2\pi \quad (1.7)$$

where R_0 is the slant range, λ is the wavelength of the transmitted signal with the corresponding frequency f_c , τ_{atmo} is the propagation time delay due to the atmosphere, and ϕ_b is due to speckle (shown in Figure 1.3). Individual phase contributions can be separately estimated by accounting for all the other contributors. For example, Figure 1.5 shows how dual-pass single-baseline InSAR can be used to estimated topographic height. This is done by isolating ϕ_{topo} in (1.7). Assuming that the separation between the two passes is small (not necessarily zero) in both time and space, then ϕ_{defo} and ϕ_{atmo} can be neglected. This is because the deformation phase, ϕ_{defo} , is temporally dependent, while the atmospheric phase, ϕ_{atmo} , is spatio-temporally dependent. Likewise ϕ_{decorr} (caused by differences in the coherent sum of individual scatterers within the resolution cell) will be reduces, but not entirely removed. The flattening phase, ϕ_{flat} , is removed by accounting for the curvature of the Earth.

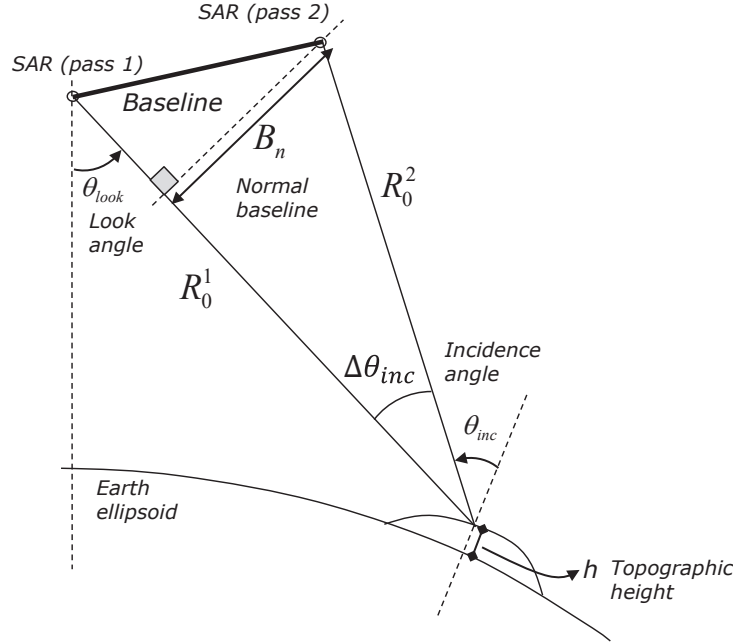


Figure 1.5: Illustration of how single baseline InSAR is used for topographic measurements. From [8].

Using InSAR to measure topography over ice will give rise to a penetration bias. This is because radar waves generally propagate some distance into ice and backscatter due to volumetric scattering inside the medium (See Section 1.3). While this can be a nuisance when investigating only the surface topography, it can be exploited for 3D tomography if we are able to steer the focused beam in the elevation direction. This can be achieved with multiple baselines as discussed in Section 1.2.2.

1.2.1.1 Covariance and coherence

It is seen from (1.7) that the interferometric phase is influenced by the speckle terms ϕ_b^1 and ϕ_b^2 . In Section 1.1.2 it was stated that SLC images has certain statistical properties due to speckle, given some relevant assumptions. In order to investigate how these statistical properties might influence the interferograms on a pixel-to-pixel basis, we use the concept of covariance and coherence. They will be introduced for an arbitrary number of acquisitions N (number of flight tracks), so that they are generally applicable, whether for single-baseline InSAR (where $N = 2$ acquisitions are used) or multi-baseline InSAR (with $N > 2$ acquisitions).

For complex Gaussian distributed data the maximum likelihood (ML) estimate of the unknown data covariance matrix \mathbf{R} is given by the sample covariance matrix [9] as

$$\hat{\mathbf{R}} = \frac{1}{L} \sum_{l=1}^L \mathbf{y}(l) \mathbf{y}^H(l) \quad (1.8)$$

where $\frac{1}{L} \sum_{l=1}^L$ is the normalized sum over L independent looks (i.e. a local spatial average), \mathbf{y} is the sample vector, and superscript H is the hermitian conjugate. The sample vector \mathbf{y} is defined from the complex signal, s , measured on each of the flight tracks

$$\mathbf{y} = [s_1, \dots, s_N]^T \quad (1.9)$$

with N being the total number of flight tracks, and T denoting the transpose. The covariance matrix is thus defined per pixel as the outer product between the complex signals measured for that pixel from different acquisitions and the complex conjugate of the same signals.

For some applications the matrix inverse of the covariance matrix is used (e.g. Capon beamforming, Section 1.2.2.2.2). If $\hat{\mathbf{R}}$ is ill-conditioned (due to singularity etc.), it can cause numerical instability in the inversion. One method of mitigating this is diagonal loading as discussed in [10]. This involves adding a small positive term to the diagonal of $\hat{\mathbf{R}}$ before inversion

$$\tilde{\mathbf{R}} = \hat{\mathbf{R}} + \alpha \mathbf{I}_N, \quad \alpha \geq 0 \quad (1.10)$$

where α is a small scaling factor and \mathbf{I}_N is the unit matrix of size $N \times N$.

Coherence is introduced as

$$\gamma_{i,j} = \frac{E[s_i s_j^*]}{\sqrt{E[|s_i|^2]}\sqrt{E[|s_j|^2]}} \quad (1.11)$$

where subscripts $i, j \in \{1, \dots, N\}$ denote the track number. The true expectation value $E[\cdot]$ is not known, so in practice the coherence is estimated as

$$\hat{\gamma}_{i,j} = \frac{\sum_{l=1}^L s_i s_j^*}{\sqrt{\sum_{l=1}^L |s_{i,i}|^2} \sqrt{\sum_{l=1}^L |s_{j,j}|^2}} \quad (1.12)$$

over L number of looks. From this it is seen that the coherence is really just the normalized elements of the sample covariance matrix

$$\hat{\gamma}_{i,j} = \frac{\hat{R}_{i,j}}{\sqrt{\hat{R}_{i,i}} \sqrt{\hat{R}_{j,j}}} \quad (1.13)$$

where $\hat{R}_{i,j}$ are elements of $\hat{\mathbf{R}}$. The magnitude of the coherence, $|\hat{\gamma}_{i,j}|$, measures the statistical similarity between acquisitions, and is used as a quality indicator for how reliable the interferometric phase is. It ranges from 0 to 1, with values near 1 indicating strong correlation between the two SAR pixels, and values near 0 indicating decorrelation. It is trivially seen that $|\hat{\gamma}_{i,i}| = 1$, which simply states that pixels from a single acquisition are fully correlated with themselves (i.e. identical).

For InSAR applications the coherence magnitude is an important parameter to consider, as it indicates whether observed phase differences are likely due to physical differences or phase noise. Various factors influence the coherence magnitude, as is shown in Figure 1.6. For measurements of ice, the volume decorrelation is expected to have a large impact on the coherence magnitude.

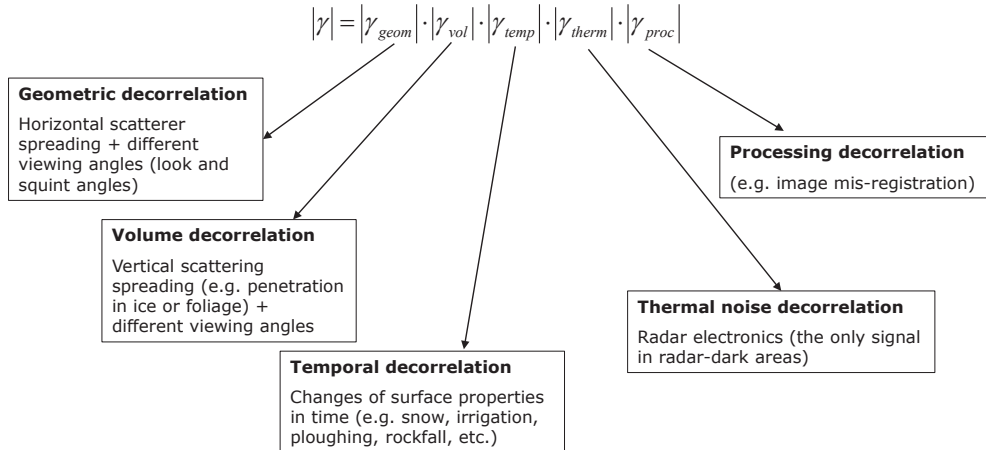


Figure 1.6: Factors that influence the coherence magnitude of pixels in an interferogram. Illustration is from [8].

1.2.2 Tomographic SAR

SAR tomography (TomoSAR) is a MB-InSAR technique used to observe the 3D structure of the illuminated volumetric media. The way TomoSAR produces 3D resolution capabilities is similar to 2D SAR imaging. A conventional SAR system transmits short pulses and receives the echoes backscattered by the illuminated scene. The received signal is sampled in both range and azimuth, allowing targets to be resolved within this range/azimuth plane (2D). However, the third dimension (perpendicular to the range/azimuth plane, remains completely unresolved with this scenario.

A TomoSAR survey is conducted by illuminating the same scene several times from slightly different points of view by flying the SAR sensors along multiple trajectories. This effectively forms a synthetic aperture in the elevation direction. Sampling the signal in this third dimension makes it possible to focus the received signal not only in the range/azimuth plane, as in conventional 2D SAR imaging, but also in elevation. A sketch of the concept is shown in Figure 1.7, where TomoSAR voxels are represented by orange ellipses.

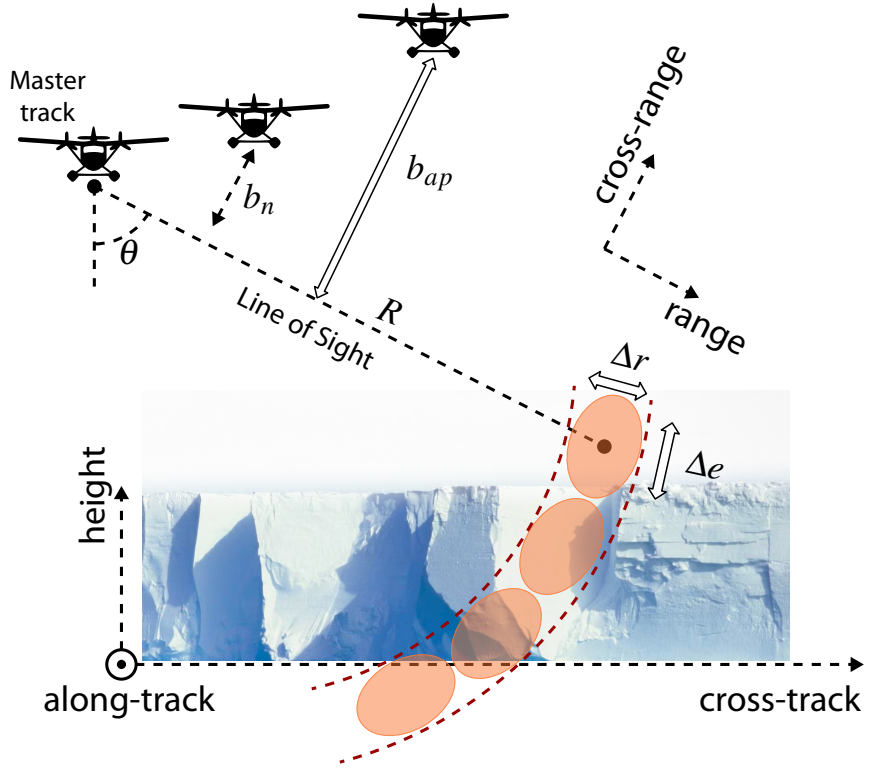


Figure 1.7: TomoSAR geometry and tomographic voxels in the height/cross-track plane. Inspired by [11].

1.2.2.1 Multi-baseline signal model and phase contributions

In this section the tomographic signal model is introduced in order to provide grounds for the tomographic processing methods applied in this worked and later described.

We assume an acquisition scenario as presented on Figure 1.1. Furthermore, for the sake of simplicity, a flat earth is assumed, such that the along-track and cross-track coordinates becomes rectangular. These rectangular along-track and cross-track coordinates will hereby be denoted (x, y) . Following this notation, the received signal for the n -th acquisition within the aperture will be given as

$$I_n^{SLC}(x, y) = \int_{\Delta r} s(y', z') \exp \left(j \frac{4\pi}{\lambda} R_n(y', z') \right) dy' dz' \quad (1.14)$$

Where $s(y', z')$ denotes the complex backscattered signal from each individual scatterer within the resolution cell, Δr , λ is the wavelength, and $R_n(y', z')$ is the slant-range from the radar to each scatterer. Thus, the signal will be the integral or sum of the individual scatterers within the resolution cell.

In order to extract height information from the signal, we have to extend the expression for the range. Choosing an arbitrary master track, M , and an arbitrary reference point, typically associated with known terrain, (y_{ref}, z_{ref}) , we can write the following expression for the range to a given scatterer:

$$R_n(y', z') \simeq R_n(\text{ref}) + r' + \frac{b_n}{R_M(\text{ref})} v' \quad (1.15)$$

where r', v' is the slant-range and cross-range/elevation coordinate of the scatterer with respect to the reference point, and b_n is the normal baseline between the n -th track and the master track (see Figure 1.7). If the baseline vector between the master track and the n -th track is decomposed into two components; one running in parallel with the slant-range direction and one perpendicular to it, the normal baseline is defined as the perpendicular component. This can be calculated as $b_n = (\theta_n - \theta_M)R_M(\text{ref})$, where θ_n is the look angle for a given track.

We define the projection of scatterers along the cross-range axis as

$$P(v') = \int_{\Delta r} s(r', v') \exp\left(j \frac{4\pi}{\lambda} r'\right) dr' \quad (1.16)$$

a term which is identical for all sensors within the aperture, we can then write the expression for the signal on the form

$$I_n^{SLC}(v) = \int_{\Delta r} P(v') \exp\left(j \frac{4\pi}{\lambda} R_n(y_{ref}, z_{ref})\right) \exp(j k_n^v v') dv' \quad (1.17)$$

where k_n^v is the vertical wavenumber given as

$$k_n^v = \frac{4\pi b_n}{\lambda R_M(\text{ref})} \quad (1.18)$$

If we want to express target elevation in terms of height, z , above/below the reference point (see Figure 1.8), we define the vertical wavenumber with respect to height as

$$k_n^z = \frac{4\pi b_n}{\lambda R_M(\text{ref}) \sin \theta} \quad (1.19)$$

As the term $\exp\left(\frac{4\pi}{\lambda} R_n(y_{ref}, z_{ref})\right)$ is known, it can be corrected for, leaving us with the final expression for the terrain corrected tomographic signal;

$$I_n^{tc}(z) = \int_{\Delta r} P(z') \exp(j k_n^z z') dz' \quad (1.20)$$

with superscript tc being short for "terrain corrected". Looking at this, it can readily be seen that a target at a height not equal to the reference height will contribute to a linear phase shift over the aperture. This is the basis of tomographic processing, as this height can be extracted through different spectral estimation techniques, which form the basis for tomoSAR processing. [12]

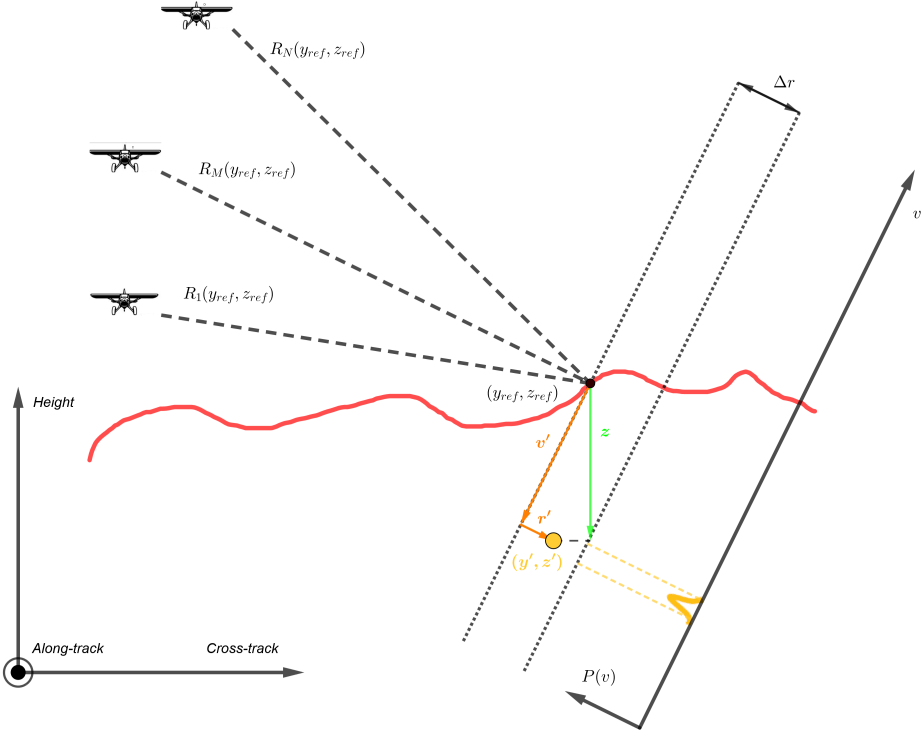


Figure 1.8: TomoSAR acquisition scenario. The red terrain denotes the reference terrain, while the yellow point denotes a scatterer inside the cell. The slanted rectangle with a width of Δr represents a resolution cell.

1.2.2.2 TomoSAR focusing

As stated above, tomographic information is extracted from the multi-baseline SAR images with spectral estimation techniques or beamformers, allowing for the formation of tomographic cubes. In this work, two nonparametric (Fourier and Capon) and one parametric (spectral MUSIC) techniques are used. The difference between these two techniques is that parametric estimation requires prior knowledge about the signal generation process. This knowledge is then used to improve the spectral resolution [9][13]. Both Capon and MUSIC are known as super-resolution techniques, as they reduce sidelobes and enhance resolution. This proves very useful for TomoSAR [14], but it is duly noted that super-resolution techniques lack the direct power spectrum interpretation of traditional Fourier beam-forming [9], leading to poor radiometric accuracy, which is especially pronounced for the MUSIC pseudo-spectrum.

1.2.2.2.1 Fourier The simplest spectral estimator is the Fourier beamformer [10]. This method simply consist of performing a discrete time Fourier transform on the tomographic signal across the tomographic aperture. For the single look (SL) case, the processed signal for an aperture consisting of N acquisitions is simply given as

$$f_{\text{Fourier}}^{\text{SL}}(z) = \frac{1}{N} \sum_n^N I_n^{tc} e^{jk_n^z z} \quad (1.21)$$

which is when equal spacing between the normal baselines is exactly equal to the discrete time Fourier transform. In the more suitable multi-looked (ML) case, the output of the Fourier beamformer can be written on vector form, by employing the sample covariance-matrix, $\hat{\mathbf{R}}$, yielding

$$f_{\text{Fourier}}^{\text{ML}}(z) = \frac{1}{N^2} \mathbf{a}^H(z) \hat{\mathbf{R}} \mathbf{a}(z) \quad (1.22)$$

where $\mathbf{a}(z)$ is the steering vector given as

$$\mathbf{a}(z) = [1, e^{jk_2^z z} \dots e^{jk_N^z z}]^\top \quad (1.23)$$

1.2.2.2.2 Capon As described in [9] the Capon spectral estimator is an adaptive estimator unlike Fourier. Weights are applied to minimize the variance (average power) without distorting the signal in the desired direction. For that reason it is also known as a Minimum Variance Distortionless Response (MVDR) spectral-estimator. In most scenarios, the Capon estimator will perform better than the Fourier beamformer in terms of spatial resolution, particularly for closely spaced targets. It is also worth noting that the spatial resolution of the capon spectral estimator depends on the noise level. For high SNR the peaks found using Capon become more narrow. Indeed, the Capon spectral-estimator can be equal to that of MUSIC (see section 1.2.2.2.3) when $\text{SNR} \rightarrow \infty$, while it degrades at low SNR [15].

The Capon psedo-spectrum is given by

$$\hat{f}_{\text{Capon}}(z) = \frac{1}{\mathbf{a}^\text{H}(z)\tilde{\mathbf{R}}^{-1}\mathbf{a}(z)} \quad (1.24)$$

where $\mathbf{a}(z)$ is the steering vector defined in (1.23), superscript H is the hermitian conjugate, and $\tilde{\mathbf{R}}^{-1}$ is the inverse of the diagonally loaded covariance matrix given in (1.10).

1.2.2.2.3 MUSIC The MULTiple SIgnal Classification (MUSIC) algorithm is a parametric method for estimating frequencies of signals embedded in white additive noise. As states in [9][16] this method uses an eigen-decomposition of the covariance matrix, $\hat{\mathbf{R}}$, given in (1.8). Let M be the number of samples (baselines), N_s the number of distinct signals contained in the noise, and $\lambda_1 \geq \lambda_2 \geq \dots \geq \lambda_M$ denote the eigenvalues of $\hat{\mathbf{R}}$ arranged in non-increasing order. Without multiplicative noise and assuming $M > N_s$, then the following is valid

$$\begin{cases} \lambda_k > \sigma^2 & \text{for } k = 1, \dots, N_s \\ \lambda_k = \sigma^2 & \text{for } k = N_s + 1, \dots, M \end{cases} \quad (1.25)$$

where σ^2 is the white Gaussian noise variance. The eigenvectors associated with eigenvalues λ_k can now be split into two subsets according to (1.25). Thus

$$\begin{aligned} \hat{\mathbf{S}} &= [\mathbf{s}_1, \dots, \mathbf{s}_{N_s}] \quad (M \times N_s) \\ \hat{\mathbf{G}} &= [\mathbf{g}_1, \dots, \mathbf{g}_{M-N_s}] \quad (M \times (M - N_s)) \end{aligned} \quad (1.26)$$

spans the signal and noise subspace of $\hat{\mathbf{R}}$, with $[\mathbf{s}_1, \dots, \mathbf{s}_{N_s}]$ being the eigenvectors corresponding to the first N_s eigenvalues, $\lambda_1 \geq \dots \geq \lambda_{N_s}$, and $[\mathbf{g}_1, \dots, \mathbf{g}_{M-N_s}]$ being the eigenvectors corresponding to the remaining $M - N_s$ eigenvalues, $\lambda_{N_s+1} \geq \dots \geq \lambda_M$. The MUSIC pseudo-spectrum is now obtained from

$$\hat{f}_{\text{MUSIC}}(z) = \frac{1}{\mathbf{a}^\text{H}(z)\hat{\mathbf{G}}\hat{\mathbf{G}}^\text{H}\mathbf{a}(z)} \quad (1.27)$$

where $\mathbf{a}(z)$ is the steering vector given in (1.23) and H is the hermitian conjugate.

An example of the three spectral estimation techniques assuming a perfect and uniform acquisition geometry is shown on Figure 1.9. It is clearly seen that the Fourier beamformer is not able to resolve all three targets, while both the Capon and MUSIC spectral estimators have very large peaks at the nominal target positions, the latter having the best resolution.

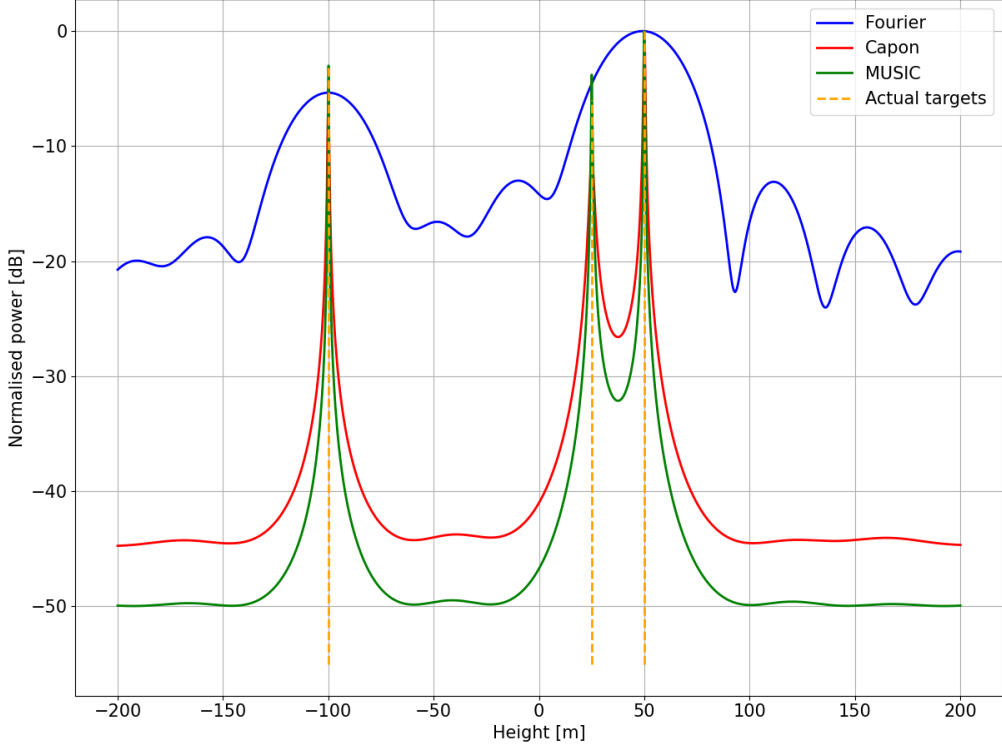


Figure 1.9: Example showing the three different spectral estimation techniques. Perfect terrain correction and acquisition geometry with a uniform vertical baseline spacing of 4 m and 10 tracks are used. The three targets are assumed to be at range 5000 m, while the reference sensor is located at height 4000 m. Random Gaussian noise has been added, to provide a SNR of 15. The covariance matrix used is created from 225 samples of the signal. Generated by modified code from [17].

1.2.2.2.4 Height ambiguity and vertical resolution The two most important parameters, when designing a tomographic aperture is the height of ambiguity and vertical resolution. [10][18] Height ambiguities arise, because the phase of the signal over the aperture due to a target at a given height is cyclic. Thus, signals from two targets at different height will appear identical, if the height difference causes a phase difference of $n2\pi$ where $n \in \mathbb{R}$.

The phase of a signal with unity amplitude and height z is

$$\phi_n(z) = \frac{4\pi b_n}{\lambda R_M(y_{ref}, z_{ref}) \sin \theta} z \quad (1.28)$$

Assuming an equidistant normal baseline spacing, Δb , then the ambiguous height is

$$z_a = \frac{\lambda R_M(y_{ref}, z_{ref}) \sin \theta}{2\Delta b} \quad (1.29)$$

It can be shown from (1.28) that $[\phi_n(z)]_{\text{mod } 2\pi} = [\phi_n(z + z_a)]_{\text{mod } 2\pi}$ thus illustrating the phase ambiguity. As indicated by (1.29) the height of ambiguity is a function of baseline spacing, where larger spacing will lead to a small height of ambiguity. The height of ambiguity is directly related to the aliasing phenomena of the spectrum of a discretely uniformly sampled function. However, when the signal is non-uniformly sampled, which it is, if the vertical and thus normal baseline spacing is not equidistant, the height ambiguity phenomenon becomes much more complex, meaning that artifacts appears at the same location as the alias signal, however with a different amplitude. This can make the ambiguous signal "vanish", but also give rise to other artifacts e.g. reduced resolution and increased noise floor, as illustrated on Figure 1.10. [19]

The second important parameter, the vertical resolution, is given as

$$\Delta z = \frac{2\pi}{\Delta k_z} \quad (1.30)$$

where Δk_z is the difference between the maximum and minimum k_z -value. The vertical resolution is a function of both aperture length, wavelength, and range, meaning that the vertical resolution gets worse as the range and wavelength are increased, while it improves, as the tomographic aperture is increased. While the vertical resolution is inherent to the shape of the Fourier point target response and thus only applies directly to the Fourier beamformer, it still has an impact on the super-resolution techniques.

From this, the main concerns when designing a tomographic aperture is easily identified. First, a large enough aperture length will have to be chosen in order to provide sufficient vertical resolution, while it will have to be sampled with a small enough sample spacing, so that the height of ambiguity lies outside the expected vertical range of the scene.

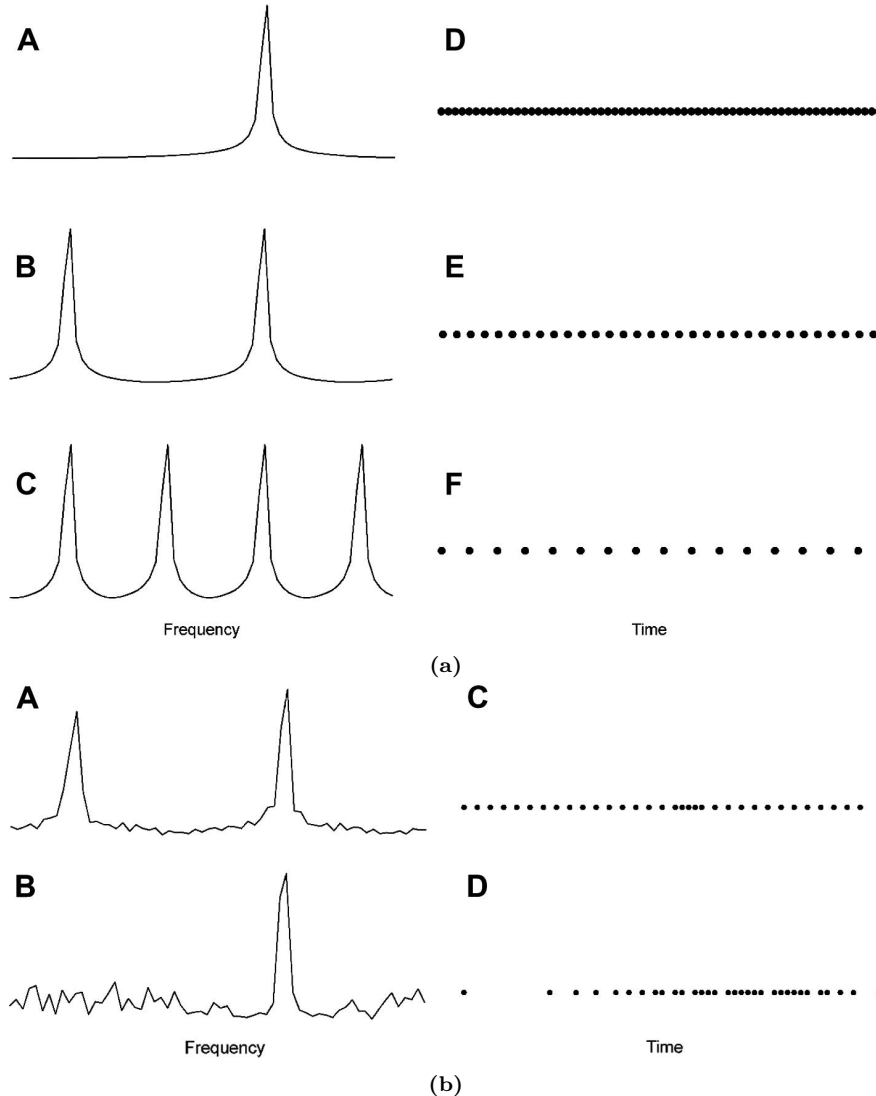


Figure 1.10: (a): Spectrum as it would appear if sampled at the Nyquist rate, one half the Nyquist rate, and one quarter the Nyquist rate. (b): Spectrum using two different non-uniform samplings. Both figures are from [19].

1.3 Scattering dynamics and penetration

In this work, we will be processing tomographic data acquired over ice. Ice as a medium is partially transparent to microwaves. This is different from other media such as soil or water. It allows radar waves to penetrate into ice. The waves propagate for some distance before absorption and volumetric scattering attenuates the (return) signal to an undetectable level. The same holds true for snow packs.

The penetrating capability of microwaves allow long-wavelength radars to "see" into these media, but it also means that the apparent phase center of the returned signal will lie somewhere within the media, at a depth determined by the material properties at that location. This is illustrated in Figure 1.11.

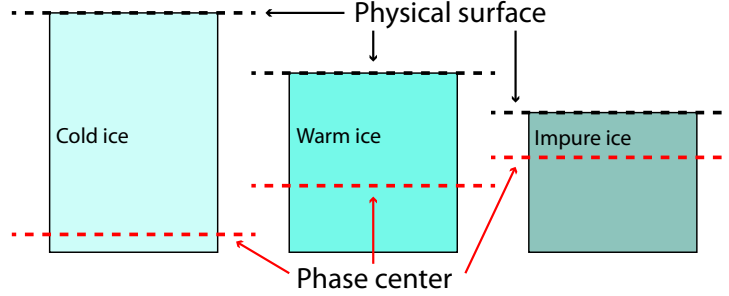


Figure 1.11: Illustration of microwave phase centers in relation to the physical surface in different ice types.

The way microwaves propagate through a medium depends on the complex permittivity, ε , of that medium

$$\varepsilon = \varepsilon' + j\varepsilon'' \quad (1.31)$$

with the real part ε' often referred to as the dielectric constant and the imaginary part ε'' called the loss factor. According to [20] the scattering depth, δ_p , of radar waves in a homogeneous medium equals the depth at which the signal power is attenuated to e^{-1} of the power at the surface. This depth is found as

$$\delta_p = \frac{\lambda}{4\pi} \frac{1}{\sqrt{\left\{ \left[1 + \left(\frac{\varepsilon''}{\varepsilon'} \right)^2 \right]^{\frac{1}{2}} - 1 \right\} \cdot \frac{\varepsilon'}{2}}} \quad (1.32)$$

where λ is the radar wavelength in free space. The penetration depth as a function of frequency is shown in Figure 1.12 for both pure ice and impure ice² at two different temperatures. The values displayed are for vertical incidence angles. Off-nadir penetration depths are found by multiplying with the cosine of the incidence angle. While the figure does not show penetration depth for P-band radar waves, it can be shown that the curves level out towards lower frequencies. This short analysis shows that penetration depths in the range of 10-100 m is to be expected.

²"Impure ice" in [20] refers to sea ice with a salinity of 35 ppm. It is used as a suitable measure for glacial ice also.

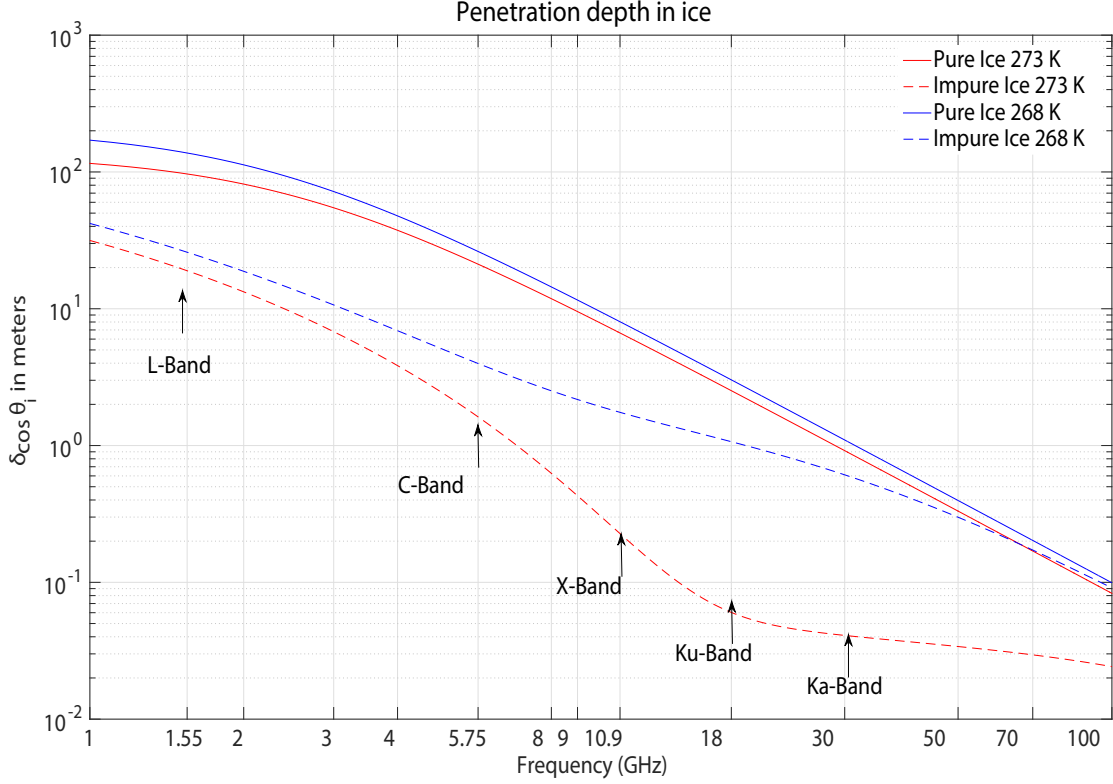


Figure 1.12: Penetration depth of common radar bands into pure ice (solid lines) and impure ice with a salinity of 35 ppm (dashed lines), at 273 K (red curve) and at 268 K (blue curve). The angle of incidence is vertical. Figure is from [20].

1.4 Phase calibration

All of the above theory has been presented under the assumption that the position of the imaging sensor, i.e. the radar, is known perfectly. However, in a real imaging setting, the sensor positions is not known exactly. This uncertainty in sensor position will manifest itself in phase errors, so called phase screens, which are based on the geometry of the sensor position errors at a given along-track position and target elevation, thus giving rise to unique phase screens for each along-track position. The consequences of these phase screens range from a reduction in the vertical resolution of the subsequent tomographic images to total vertical defocusing. Even sub-wavelength errors in the sensor positions can lead to significant phase screens. Therefore, a method which estimates these phase screens for the purpose of removal is needed before tomographic processing can be applied. This procedure is called phase calibration, and in this work, we have chosen to implement the phase calibration method called *Phase Center Double Localization* (PCDL) which is presented in [12]. The advantage of this particular method is the fact that the phase screens can be estimated without the need of external information or point-like targets, but is solely from the data itself.

1.4.1 Problem formulation and geometry

Visiting the tomographic signal model introduced in Equation (1.20), but this time casting it in terms of cross-range coordinate v instead of height z and assuming sensor position errors in the cross-track height plane, (dY_n, dZ_n) , we can write the signal model under errors as

$$I_n^{tc} = \exp(j\alpha_n) \int_{\Delta r} P(v') \exp(jk_n^v v') dv' \quad (1.33)$$

where α_n is a phase screen given as

$$\alpha_n = \frac{4\pi}{\lambda}(-\sin \theta_n dY_n + \cos \theta_n dZ_n), \quad (1.34)$$

where θ_n is the look angle for the n -th track to the given pixel. The phase screen originates from the fact that the term $\exp\left(j\frac{4\pi}{\lambda}R_n(y_{ref}, z_{ref})\right)$ in eq. (1.16) (which is corrected for in order to obtain eq. (1.20)) is erroneous under the presence of sensor position errors, since the observed range to the reference target will then be

$$R_n(y_{ref}, z_{ref}|(dY_n, dZ_n)) = R_n(y_{ref}, z_{ref}) - \sin \theta_n dY_n + \cos \theta_n dZ \quad (1.35)$$

thus giving rise to the phase screen. As stated before, we want to estimate these phase screens, so they can be removed.

The cardinal problem to be solved in the PCDL phase calibration method is that of double localization. The double localization problem formally stated as the problem of jointly solving for both sensor position errors and target cross-track height based on the set of distances from the sensors to the targets given the corresponding set of sensor and target positions, (Y_n, Z_n, y_p, z_p) . If a master sensor is chosen, whose position is assumed to be known perfectly, such that $dZ_M = dY_M = 0$, and a reference target (tie point), v^T , is chosen, whose elevation is assumed to be zero, it can be shown that the double localization problem results in a system of $N_e = (N - 1)P$ linear equations with $N_x = 2(N - 1) + P - 1$ unknowns, where N is the number of sensor, and P is the number of targets. The linear equations will be on the form

$$dR_n^p - dR_M^p = -\sin \theta_n^p dY_n + \cos \theta_n^p dZ + \frac{b_n^p}{R_M^p} v^p \quad (1.36)$$

where $dR_n^p = R_n^p - R_n^p|_{(dY_n, dZ_n)}$ i.e. the difference between the distances to a target given true sensor positions and the distances given the nominal sensor positions including errors. Furthermore, it can be shown that as long as $N_e \geq N_x$, which is the case, when $N, P \geq 3$, the system can be solved uniquely down to roto-translation of the coordinate system used to represent sensor and target positions. [12]

A short summary of the nomenclature used in the context of phase calibration is shown in Figure 1.13.

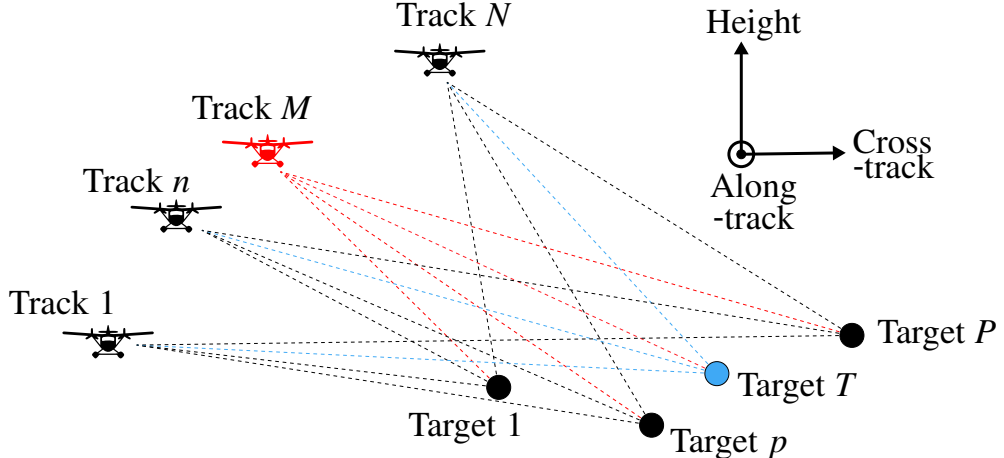


Figure 1.13: Nomenclature of tracks and targets used in this work. The scene is viewed in the cross-track/height-plane. The sensors are denoted by their track number $n = 1, \dots, N$. Targets are likewise numbered as $p = 1, \dots, P$. The reference sensor is further labeled as M and the tie point as T .

1.4.2 Phase linking

Information about differences in the distance from sensors to targets can be derived with great accuracy from the interferometric phase, $\phi_{nm} = \angle(I_{nm})$, where I_{nm} is interferogram between the n -th and m -th sensor, i.e.

$I_{nm} = I_n^{tc}(I_m^{tc})^*$. For a point target, the interferometric phase between sensors n and m will quite simply be given by the geometric distances as

$$\phi_{nm} = \frac{4\pi}{\lambda}(dR_n^p - dR_m^p) \quad (1.37)$$

where we have neglected any atmospheric phase contributions. A useful property of point targets is that of phase triangulation. Phase triangulation means that the interferometric phase between two sensors for a given target can be expressed in terms of the interferometric phases between sensor and a master sensor, expressed as

$$\phi_{nm} = \phi_{nM} - \phi_{mM} \quad (1.38)$$

However, when dealing with volumetric targets, which will be the case for the most part in a typical TomoSAR acquisition scenario, the property of phase rectangularity breaks down. However, it has been shown³ that for multi-baseline data, a set of equivalent point-like interferometric phases with respect to a common master track can be derived from the interferograms between the different acquisitions. A set of such phases can be obtained as the set of phases, φ , which maximizes the following function

$$F_p(\varphi) = \mathcal{R} \left\{ \sum_n^N \sum_m^N w_{nm} \langle I_{nm} \rangle \exp[j(\varphi_n - \varphi_m)] \right\} \quad (1.39)$$

where \mathcal{R} denotes the real part, $\langle I_{nm} \rangle$ denotes the multi-looked interferogram, and finally w_{nm} is a set of weights used to promote certain attributes. When maximizing the function, φ_M is set to zero.

The set of phases φ is called the *linked phases*.

It can be shown that for small-baseline interferograms, the linked phases can be modeled the same way as the phase for a point target derived from Equation (1.37), namely

$$\varphi_n = \alpha_n + k_n^v v \quad (1.40)$$

where v is the elevation of phase center of the volumetric scatterer estimated by the linked phases. Thus, a set of weights which promotes smaller baselines is needed. One such set of weights is given in [12] as

$$w_{nm} = \frac{|\langle I_{nm} \rangle|}{\langle I_{nn} \rangle \langle I_{mm} \rangle} \quad (1.41)$$

which is also used in this work.

1.4.3 Double localization algorithm

Finally, an expression for the double localization problem in terms of linked phases can be written by inserting Equation (1.34) in Equation (1.40) yielding

$$\varphi_n^p = \frac{4\pi}{\lambda}(-\sin \theta_n^p dY_n \cos \theta_n^p dZ_n) + k_n^p v^p \quad (1.42)$$

which will be the equation to be solved in order to obtain the sensor position errors and target elevations. One thing to note about the linked phases, however, is that they are wrapped, meaning that they are given modulo 2π , and therefore the system of equations in (1.42) cannot be solved linearly from the linked phases without some sort of phase unwrapping. However, they might be solved directly in the complex domain, by optimizing some figure of merit. One drawback of this approach is the fact that operating in the complex domain will lead to ambiguities in the estimated sensor position errors. An example of sensor position ambiguities arising from a particular figure of merit used in [21] is shown at Figure 1.14. It is clear that even sensor position errors smaller than a wavelength might not be corrected unambiguously.

³See [12].

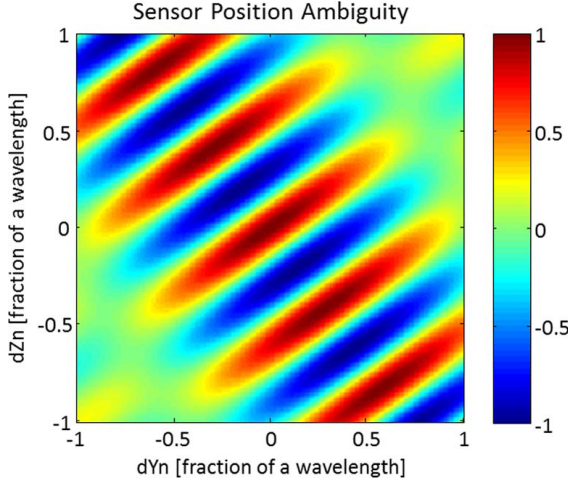


Figure 1.14: Illustration of sensor position error ambiguities [12].

Despite this fact, this approach is preferable as Equation (1.42) can be solved iteratively and rather efficiently by alternately optimizing two figures of merit. These two figures of merit are functions of sensor errors and target elevation, allowing the sensor positions and target elevation to be solved for on each iteration. This is the approach proposed in [12] which will also be adopted in this work. The exact algorithm implemented will be presented later in Section 3.4.

Finally, it is worth repeating that while PCDL phase calibration approach will yield the correct phase screens, the exact sensor position errors cannot readily be extracted due to the ambiguities arising when solving the double localization problem in the complex domain. Furthermore, the double localization problem is formed down to a roto-translation of the coordinate system, and therefore the tomographic cube formed after counter-rotation with the estimated phase screens will also be subject to this roto-translation. If desired, these can be corrected afterwards using a-priori information about e.g. expected terrain slopes of the reference terrain, however it will not be possible to resolve this given the data alone.

Chapter 2

Introduction to the data

In this work, SAR images from multiple flight tracks obtained with the POLARIS instrument by the Technical University of Denmark (DTU) are processed to test and validate the implemented tomographic processing facility. The data was gathered at the K-transect near Kangerlussuaq in Greenland (See Figure 2.1). The POLARIS SAR data is combined with a digital elevation models (DEM) from TanDEM-X recorded by the German Aerospace Center (DLR).

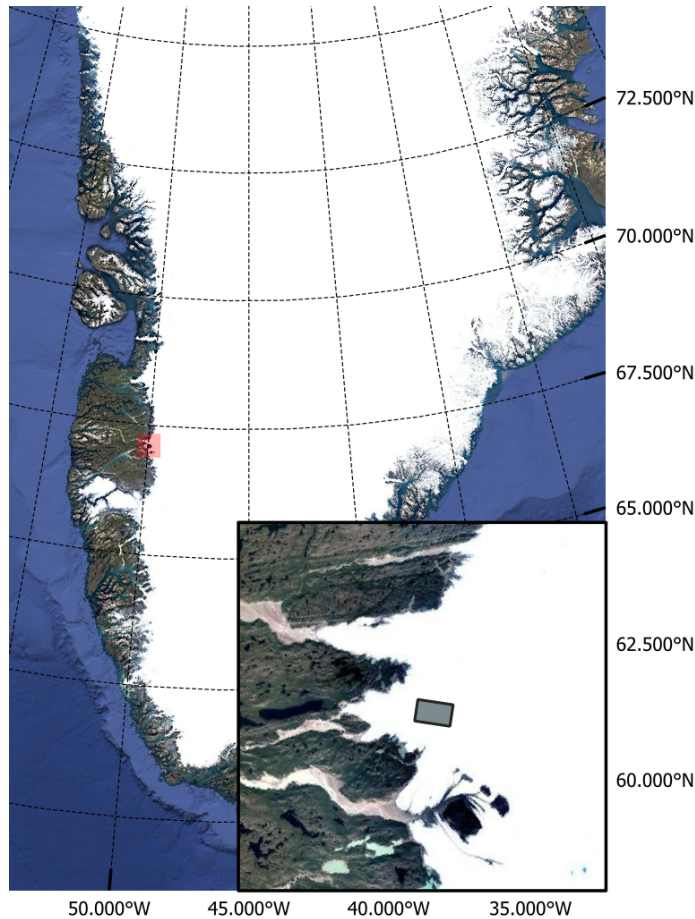


Figure 2.1: Map of the site. The extent of the scene after focusing is marked by the gray rectangle. Images from Google Maps.

2.1 The POLARIS instrument

The POLarimetric Airborne Radar Ice Sounder (POLARIS) is a scientific instrument designed for studying ice sheets and glaciers and is described in details in [22][23]. It is employed in glaciology and cryospheric research to map the internal structure of ice, and is useful for understanding ice dynamics, detecting sub-glacial features, and assessing the impacts of climate change in polar and glacial regions. POLARIS can operate in either of two modes; as an nadir-looking ice sounder or a side-looking SAR. The data used in this work was obtained with the latter mode. In this mode, the range of look angles covered by the instrument is approximately 20° to 45° , corresponding to a swath of 2.5 km in ground range at the nominal altitude. Furthermore, the POLARIS instrument can be configured to work in polarimetric mode, where polarimetric data is gathered using the full antenna aperture with navigation data referencing the phase center of the full aperture, and in multi-aperture mode, where data from each of the four sub-elements constituting the full are gathered independently with navigation data referenced to the phase center of each of the sub-elements. However, in multi-aperture mode, only single polarization (HH) data is acquired. The tomographic data acquired during the campaign was gathered using the multi-aperture mode.

The radar is mounted on the Norlandair TF-POF Twin Otter aircraft. An image of POLARIS mounted on the aircraft can be seen in Figure 2.2. In order to maintain and reproduce stable flight tracks, a system called EMAP4, developed at the DTU Space Geodynamics division, was used. The system uses GNSS to calculate and present in real-time to the pilots the current deviations from a desired track, as well as steering information to return to the track.



Figure 2.2: The setup of POLARIS [24].

The activities of the ESA IceSAR 2012 campaign focused on the K-transect in Southwest Greenland, located east of Kangerlussuaq. This area has a smooth topography that decreases from the inner part to the edge of the ice sheet, and can be divided into eight regions, as illustrated in Figure 2.3. The IceSAR campaign gather data over two of these sites; S10 in the accumulation zone and SHR in the ablation zone. We have focused our attention on the SHR site, as it provides clearer subsurface features to verify against. Data was gathered both on 07/05/2012 and 11/06/2012, but due to summer melt, the less penetration will be expected in June. Therefore, only the data from May was used in this work.

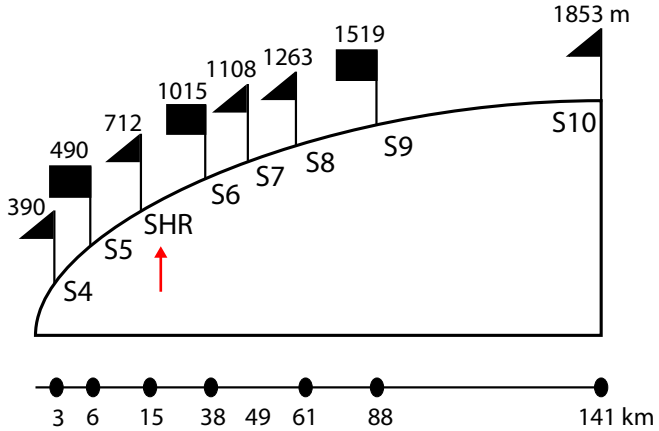


Figure 2.3: The SHR site is located in the ablation zone, below the equilibrium line altitude. Inspired by [14].

The tomographic data was acquired from different flight tracks by flying POLARIS ten times around the site of interest in a so-called racetrack. The race track is divided into a North-East North-West (NENW) segment and a South-West South East (SWSE) segment. Each segment is approximately a straight line and POLARIS was looking left along both. This work uses data from the NENW segment.

Positions along the flight tracks are provided in navigation files. These positions are given in geographic coordinates and have been converted to SCH coordinates through the transformations described in Appendix A. Figure 2.4 shows all of the 10 flight tracks. Notice the vary small vertical baseline.

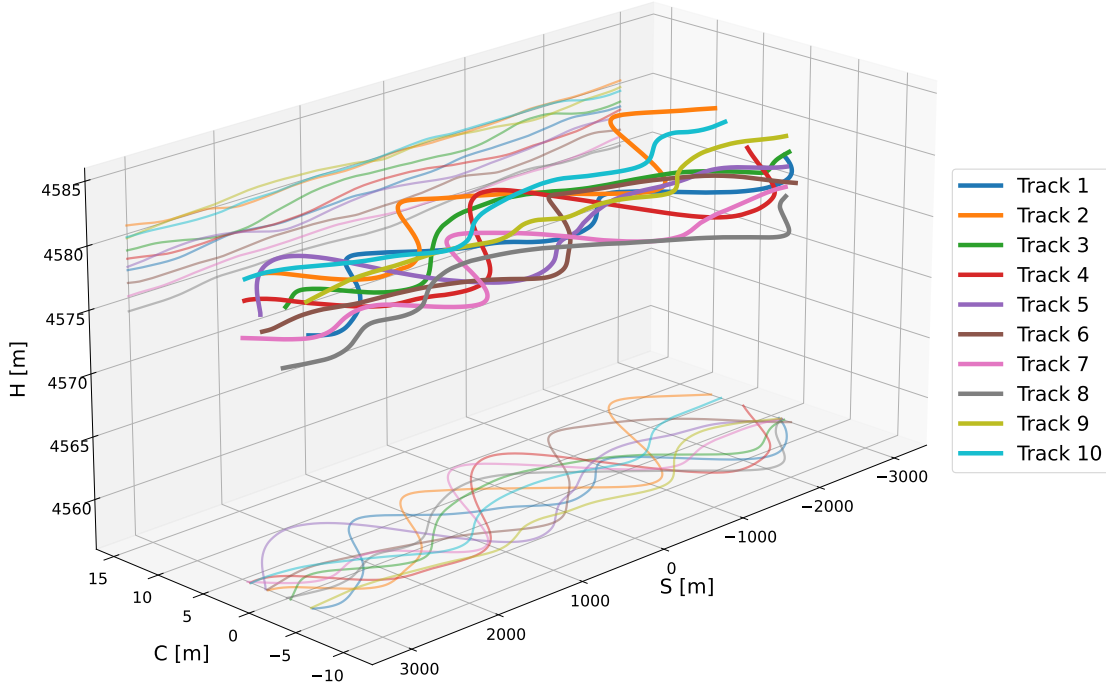


Figure 2.4: The 10 flight tracks from the SHR site flying NENW on May 7 2012. Track coordinates are the radar center positions in SCH coordinates.

The data used in this work is not the raw data. DTU has processed the data to level 0c, which means that the following processing has been done:

1. Relative calibration (gain, amplitude, phase and spectral equalization) of the received channels using data from the internal calibration loop in the radar.
2. Detection and blanking of saturated samples (caused by partial surface echoes) in the deep channel data.
3. Pulse compression of the received echoes, with weighting for sidelobe suppression.
4. Interpolation of navigation data to coincide with radar echo timestamps

In operation, POLARIS transmitted pulses at a carrier frequency of 435 MHz. It had a configuration of four antenna elements receiving individually, meaning that for each flight track four sets of measurements was made. With 10 tracks flown, the total number of acquisitions is 40. A summary of relevant POLARIS parameters can be found in Table 2.1.

Parameter	Value
Nominal sensor altitude	4 km
Incidence angles	25° - 45°
Carrier frequency	435 MHz
Wavelength	68 cm
Pulse bandwidth	85 MHz
Sampling frequency	125 MHz
Slant range resolution	1.8 m
Azimuth resolution after focusing	2 m
Number of tracks	10
S grid spacing after focusing	2 m
C grid spacing after focusing	2 m
Nominal temporal baseline	20 min
Polarization	HH

Table 2.1: Parameters of the ICESAR 2012 experiment for SHR site. Updated from [14].

2.2 TanDEM-X

TanDEM-X (TerraSAR-X add-on for Digital Elevation Measurements) is an Earth observation radar mission that consists of a SAR interferometer (InSAR) consisting of two almost identical satellites flying in close formation. A typical separation between the satellites of 120m to 500m allows global Digital Elevation Model (DEM) to be generated.

The main objective of the TanDEM-X mission is to create a precise 3D map of the Earth's land surfaces that is homogeneous in quality and unprecedented in accuracy. The data acquisition was completed in 2015 and production of the global DEM was completed in September 2016.

The TanDEM-X 90 m DEM [25] is a product variant of the global Digital Elevation Model (DEM) acquired in the frame of the German TanDEM-X mission between 2010 and 2015, and has a reduced pixel spacing of 3 arcseconds (90 m at the equator). It covers all Earth's landmasses from pole to pole. In this work we use a subset of the 90 m DEM centered on the Russell glacier to overlap the data acquired by POLARIS. It is visualized in Figure 2.5.

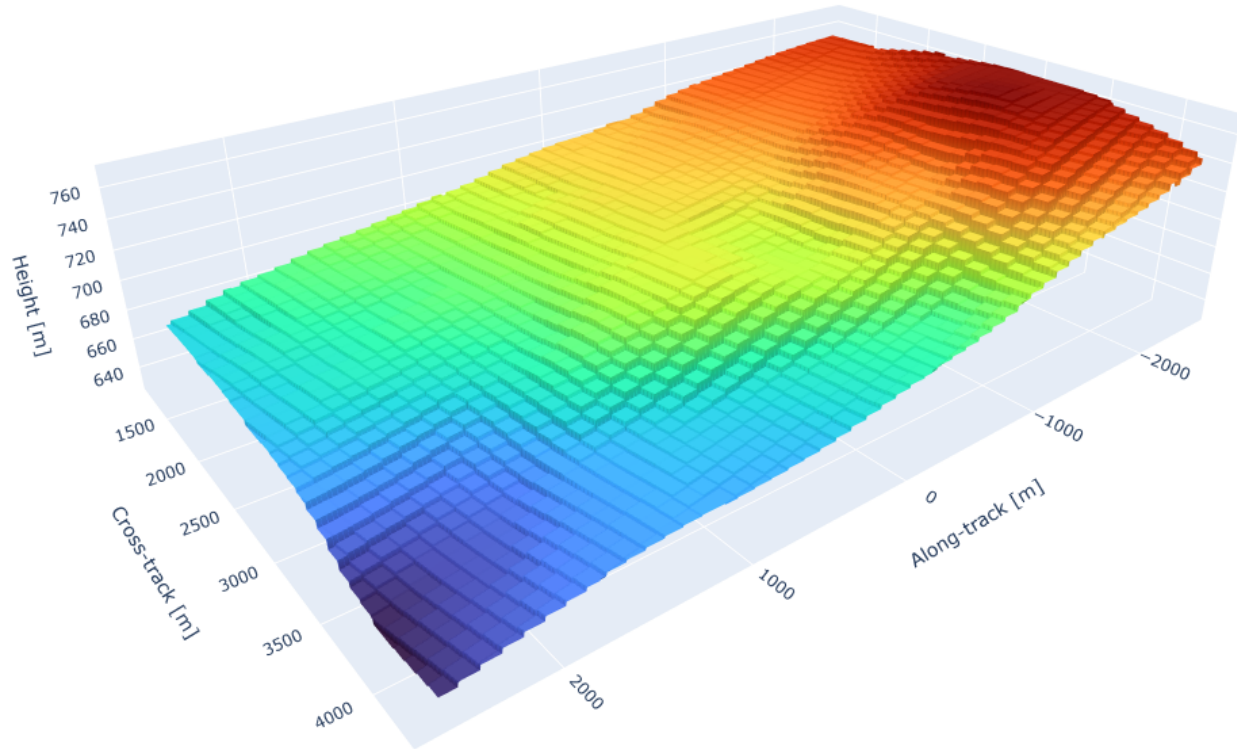


Figure 2.5: The 90 m DEM after interpolation to the chosen SC-grid. The nearest neighbor interpolation method has been used. Height axis is not to scale.

Chapter 3

Algorithm implementation and processing chain

In this chapter, the processing chain from the level 0c data to fully focused tomographic cubes will be discussed. For this work, all processing steps presented in this chapter and subsequent results have been implemented from scratch in Python. On Figure 3.1 a flow diagram of the processing chain is shown. First, the unfocused level 0c data is filtered using a spectral domain filter in order to remove a DC-component in the azimuth Doppler-spectrum, which is present on all SLC images. Second, the images are co-registered and focused to a 2 m resolution in the azimuth-direction using the Direct Back-Projection (DPB) algorithm. During this step, the geometry of the data changes from radar range and azimuth coordinates to SCH-coordinates. This focusing is carried out on all 40 images, meaning that the four element for each acquisition will be focused separately. After focusing, the four images from each acquisition are combined in phase to form the full radar aperture. Third, the resulting ten SLC images are then phase calibrated to remove phase screens caused by sensor position errors using the Phase Centre Double Localization (PCDL) algorithm. Finally, tomographic focusing can be carried out on the phase calibrated images yielding the vertically focused tomographic cubes.

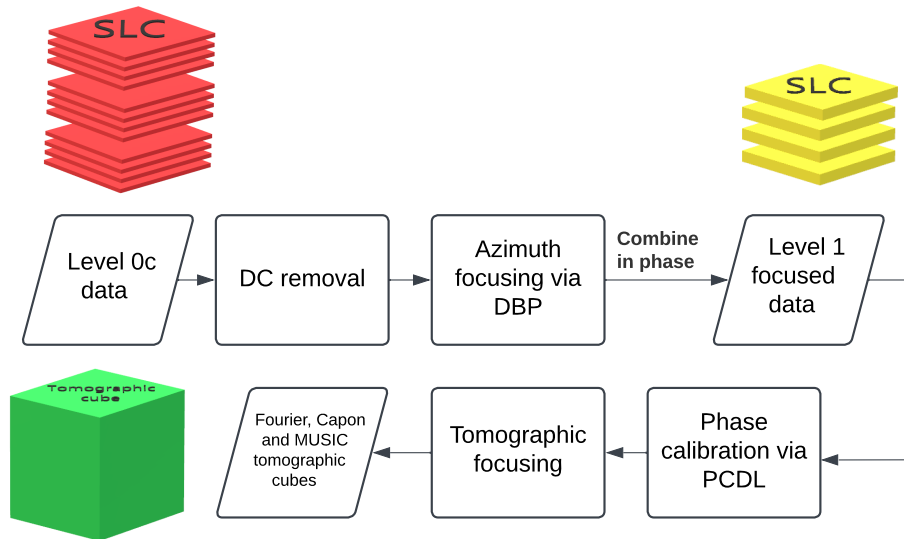


Figure 3.1: Processing chain from level 0c data to fully focused tomographic cubes.

3.1 DC filtering

The given level 0c data requires an additional pre-processing step, as a large DC response is observed in the Doppler spectrum. This is easily seen by taking the along-track FFT for each range bin, and then averaging the spectrum across all range bins. This yields the Doppler centroids shown in Figure 3.2a. The DC component could be due to ringing phenomena arising from the aircraft hull or wings [24]. It is cancelled out by applying a filter on the form

$$w_n^{DC} = 1 - w_n^{Hanning} \quad (3.1)$$

where $w_n^{Hanning}$ is the Hanning window defined in (3.7) with a width of 20 samples. The filter is centered around zero Doppler and applied in the spectral domain. Plotting the Doppler centroid again (Figure 3.2b) it is seen that the DC component is sufficiently removed.

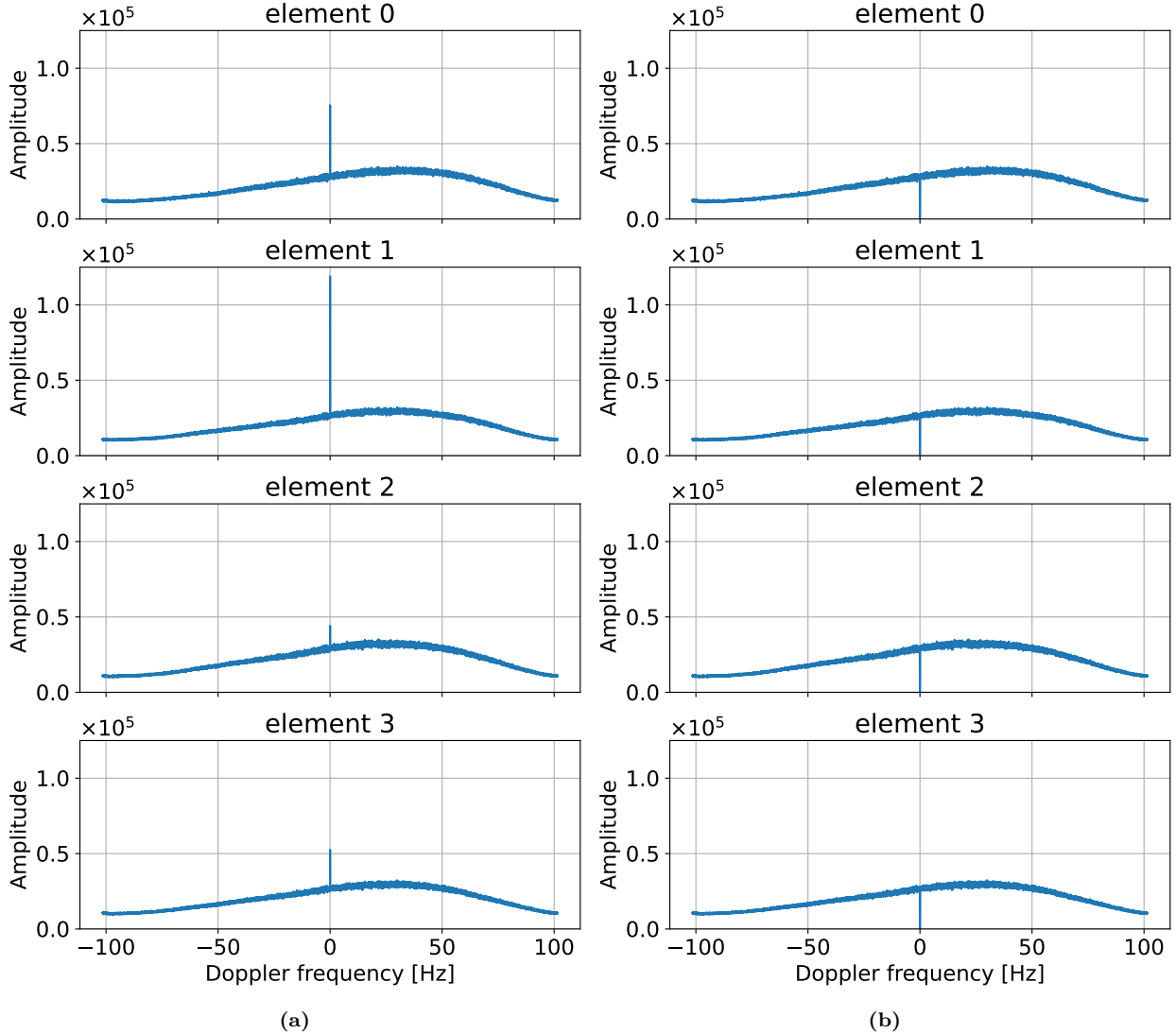


Figure 3.2: Doppler centroid for all four antenna elements from the first track.

(a) Unfiltered spectrum showing DC component.

(b) Filtered spectrum with DC component removed.

The significance of removing this component is seen through the phase of the level 0c data. Figure 3.3a shows the phases before DC filtering. For a SLC SAR image of distributed scatterers the phase is expected to be

random and uniformly distributed between $-\pi$ and π . Histograms show that the phase is indeed uniformly distributed, but it is clearly not random. Rather, we see a fringe-pattern which becomes more pronounced with increasing range. This suggests some constant DC component which is accumulating onto the phase for each range bin. After applying the filter, phases are as shown in Figure 3.3b. The fringes have disappeared and the distribution is random and uniform.

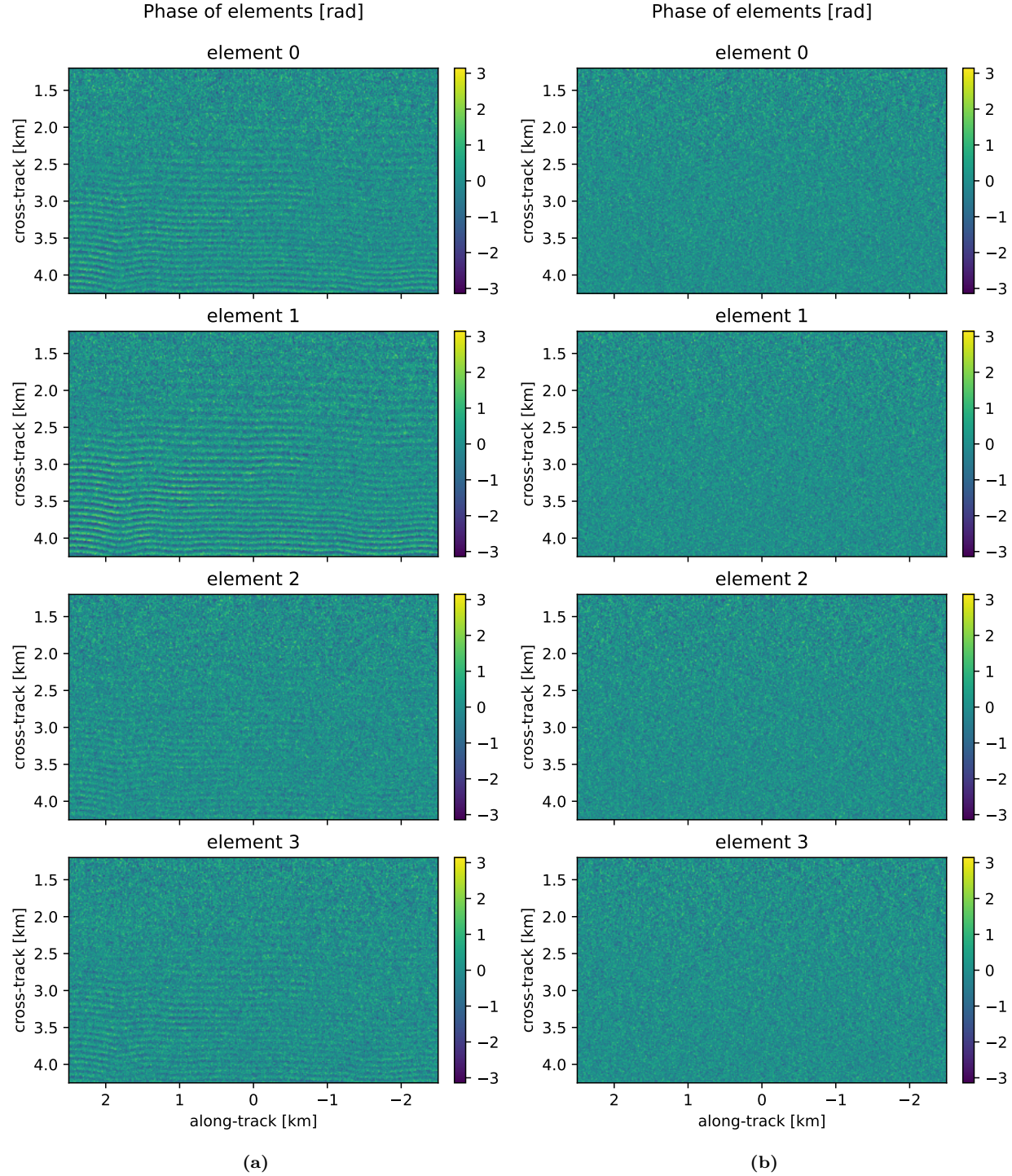


Figure 3.3: Phase of the SLC level 0c data for all four elements from Track 1.
(a) Before DC filtering. **(b)** After DC filtering.

3.2 Azimuth focusing and co-registration via DBP

In this work, the azimuth focusing and co-registration of image pixels is achieved by using the Direct Back-Projection, DBP, algorithm [26][23]. The DBP is an advantageous algorithm, as it automatically corrects the SAR images for topography and co-registers the SAR pixels from different acquisitions, if it is supplied with an external DEM. Furthermore, the algorithm automatically corrects for flight tracks which are not perfectly straight. The downside of the algorithm is that these benefits come at the expense of processing complexity and, most predominantly, processing time when compared to other focusing algorithms like e.g. the range-doppler algorithm.

The DBP is a time-domain algorithm. Given sensor positions in the *SCH*-coordinate system, $\mathbf{P}_r = (S_r, C_r, H_r)$, and a grid with pixel height given by the external DEM, the focusing of a given pixel in the grid consists of the following steps:

1. Look up the SCH coordinate of the grid pixel to be focused, $\mathbf{P}_p = (S_p, C_p, H_p)$.
2. Interpolate sensor coordinates in the intermediate coordinate system (See Section 1.1.3) to the along-track position $S_r = S_p$, thus defining the phase center at the center of the grid pixel, and calculate the broadside-range $R_b = R(S_p, C_p, H_p | S_r = S_p)$.
3. Calculate aperture length; $L_S = \frac{R_b \lambda}{2\rho_S}$, where ρ_S is the along-track resolution^a.
4. For all sensor along-track positions where $|S_r - S_p| < L_S/2$:
 - (a) Calculate range to grid pixel $R(S_p, C_p, H_p | S_r)$ using the intermediate coordinate system and convert to round-trip delay $\tau_p = 2R(S_p, C_p, H_p | S_r)/c_0$, where c_0 is the speed of light.
 - (b) Interpolate radar signal $s_0(S_r, \tau_p)$ from the complex radar image.
5. Calculate the focused pixel at grid pixel $\mathbf{P}_p = (S_p, C_p, H_p)$ using:

$$s(S_p, C_p, H_p) = \sum_{|S_r - S_p| < L_S/2} w_n s_0(S_r, \tau_p) \exp(2j\pi f_c(\tau_r - \tau_b)) \quad (3.2)$$

where w is a Hamming weight applied for side-lobe reduction given as

$$w_n = 0.54 - 0.46 \cos(2\pi n/N), \quad n \in [0, N-1] \quad (3.3)$$

where $N = L_S/\Delta S_r$ with ΔS_r being the along-track sample spacing^b.

^a ρ_S is chosen to be 2 m in this work.

^bFor the acquired POLARIS data, $\Delta S_r \approx 0.38$ m.

The reason why this algorithm can be computationally challenging is the fact that for each grid pixel $L_S/\Delta S_r$ interpolations will have to be carried out. We have used a truncated *sinc*-interpolator [21], but other interpolation techniques can also be employed. The truncated sinc interpolator is based on the fact that a band-limited signal, $s(\tau)$, which is sampled at a sampling frequency larger than the Nyquist frequency can be perfectly reconstructed from its samples using the following

$$s(\tau) = \sum_{n=-\infty}^{\infty} s_n \text{sinc}\left(\frac{\tau - \tau_n}{T_s}\right) \quad (3.4)$$

where T_s is the sampling period, $s_n = s(nT_s)$, $\tau_n = nT_s$, and $\text{sinc}(x)$ is the normalized *sinc*-function

$$\text{sinc}(x) = \frac{\sin(\pi x)}{\pi x}. \quad (3.5)$$

Equation (3.4) requires an infinitely sampled signal, and can therefore not be implemented in practice. Instead, for a given time of interest τ_p , the sum can be truncated so it becomes a sum over $2L + 1$ samples

spaced around τ_p . The truncated *sinc*-interpolator employed in this work is then expressed as

$$s(\tau_p) = \sum_{n=-L}^L w_n^{Hanning} w_n^{Amp} s_n \text{sinc}\left(\frac{\tau_p - \tau_n}{T_s}\right) \quad (3.6)$$

where $w_n^{Hanning}$ is a Hanning-window applied to suppress Gibbs-phenomena given as

$$w_n^{Hanning} = 0.5 + 0.5 \cos\left(\frac{\pi n}{L}\right), \quad n \in [-L, L], \quad (3.7)$$

and w_n^{Amp} as an amplitude weight to compensate for amplitude propagation decay given as

$$w_n^{Amp} = \left(\frac{\tau_n}{\min(\tau)}\right)^4 \quad (3.8)$$

In our implementation, we have chosen $L = 7$, meaning the sum is carried out over $2L + 1 = 15$ samples.

The unfocused images are sampled with a sampling frequency of $f_s = 125$ MHz in the range direction and an along-track sample spacing of approximately 0.38 m. These images are upsampled 8 times in the range direction using an FFT-upsampler. They are then focused to a 2×2 m SCH-grid at 2 m azimuth resolution, where $S_p \in [-2500 \text{ m}, 2500 \text{ m}]$ and $C_p \in [1200 \text{ m}, 4250 \text{ m}]$. The along-track axis has been truncated for two reasons. First, the most interesting features is located within -2500 m and 2500 m. Furthermore, this ensures that the full synthetic aperture can be formed for all grid pixels, ensuring uniform azimuth resolution. On Figure 3.4 the SLC amplitude image for Track 1 element 1 is shown before and after azimuth focusing using the DBP algorithm.

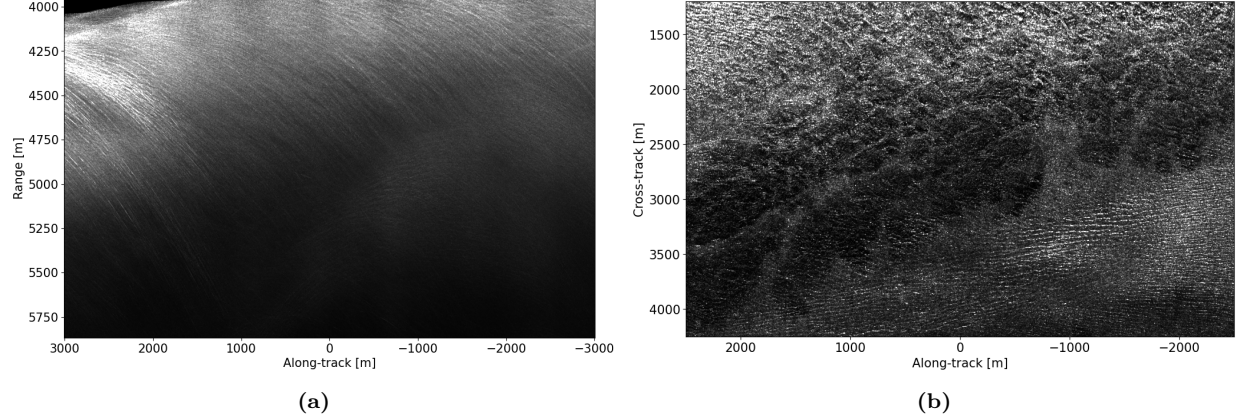


Figure 3.4: (a), SLC amplitude image for track 1 element 1 before azimuth focusing.
(b), SLC amplitude image for track 1 element 1 after azimuth focusing.

It is assumed that penetration of the radar waves into the ice occurs at the scene. One important thing to note is that refraction occurs at the air/ice interface, meaning that the propagation path length for targets under the ice sheet will be shorter than for targets in air. This situation is shown on Figure 3.5. If this is not taken into account it will lead to some kind of defocusing of the final image. However, according to [14] this defocusing has little influence for small penetration depths and small synthetic apertures. For this reason we have chosen to ignore the effects of refraction in our focusing algorithm, thus accepting possible defocusing at the benefit of simpler implementation. It should also be noted that we employ a larger synthetic aperture than that employed in [14], which will lead to stronger defocusing. Even so, we have still chosen to ignore refraction effects.

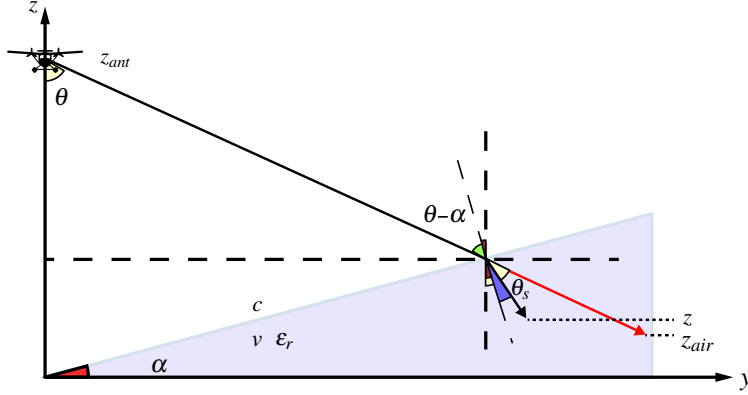


Figure 3.5: Illustration of the imaging scenario given refraction at the air/ice interface. Reconstructed from [14].

3.3 Coherent combination of SLC images

After all the 40 individual SLC images have been focused, the images from the four individual antenna elements from each acquisition is combined in phase in order to get the benefit of the full antenna aperture. The level 0c data has been compensated for one-way cable delay [23]. This correction will have to be removed before the coherent combination can be carried out. The phase shift applied before the summation is shown on Table 3.1.

Element	Phase shift [deg]
1	0
2	109.2
3	226.6
4	334.5

Table 3.1: Phase shift applied to the four elements before coherent combination.

On Figure 3.6 the single-element and four-element coherence is shown between acquisition 1 and 2. Here, it is clearly seen that the coherence is significantly improved by the coherent combination of elements, with the exception of certain areas where decorrelation likely occurs due to volume scattering. The overall improvement is likely due to the signal to noise ratio being improved when the full antenna aperture is used.

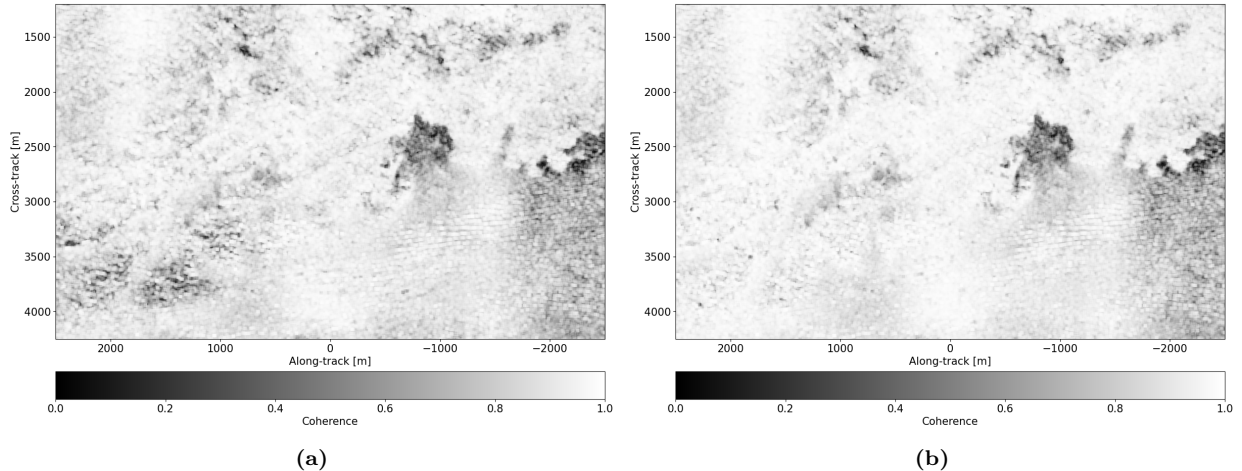


Figure 3.6: (a) Coherence for acquisition 1 and 2 using only element 1. (b) Coherence for acquisition 1 and 2 using all antenna elements.

3.4 Phase calibration via iterative PCDL algorithm

In this section, our implementation of the PCDL algorithm used to iteratively solve eq. (1.42) in order to estimate phase screens will be presented and discussed. For this task the iterative procedure proposed in [12] has been employed. Assuming that the linked phases have been calculated as described in Section 1.4.2, the algorithm consists of the following steps.

We start by introducing two phase residuals for the k -th iteration, given as

$$A_n^p|_k = \varphi_n^p - \alpha_n^p(dY_n|_{k-1}, dZ_n|_{k-1}) \quad (3.9)$$

$$B_n^p|_k = \varphi_n^p - k_n^p v^p|_k \quad (3.10)$$

where p denotes a given target, n denotes a given sensor, φ is the linked phases, and $\alpha_n^p(dY_n|_{k-1}, dZ_n|_{k-1})$ is the phase screen given the sensor position errors ($dY_n|_{k-1}, dZ_n|_{k-1}$), and v^p is the cross-range location of targets.

The two phase residuals are used to determine target elevation and sensor position errors, respectively. The algorithm works by estimating these phase residuals for each along-track position individually, meaning that sensors and targets at the first along-track position are calibrated, before it moves on to the second position and so forth. For the very first iteration of the first along-track position, we initialize the algorithm by choosing a tie-point, p^T . For this tie-point we set $v^T = 0$ hence obtaining

$$\varphi_n^T = \alpha_n^T \Rightarrow A_n^p|_{k=0} = \varphi_n^p - \varphi_n^T \quad (3.11)$$

Following this initialization, the algorithm will run the following three steps for each iteration k , until the first figure of merit $F_t(v^p)$ has converged to a chosen criteria:

1. First, the target elevations is be found by optimizing the following figure of merit for each target

$$F_t(v^p) = \mathcal{R} \left\{ \frac{1}{N} \sum_n^N \exp(j(A_n^p|_{k-1} - k_n^p v^p)) \right\} \quad (3.12)$$

such that

$$v^p|_k = \arg \max_{v^p} (F_t(v^p)) \quad (3.13)$$

2. Next, the phase residual, $B_n^p|_k$ is updated with the new estimate for target positions.

Then the sensor position errors are estimated by optimizing the following figure of merit for each sensor

$$F_s(dY_n, dZ_n) = \mathcal{R} \left\{ \frac{1}{P} \sum_p^P w^p \exp \left(j \left(B_n^p|_k - \frac{4\pi}{\lambda} (-\sin \theta_n^p dY_n + \cos \theta_n^p dZ_n) \right) \right) \right\} \quad (3.14)$$

such that

$$(dY_n, dZ_n)|_k = \arg \max_{(dY_n, dZ_n)} (F_s(dY_n, dZ_n)) \quad (3.15)$$

The weights, w^p , are used to prioritize targets with better phase center height estimation and are simply given by

$$w_p = F_t(v^p|_k) \quad (3.16)$$

3. Finally $\alpha_n^p(dY_n|_k, dZ_n|_k)$ is calculated using

$$\alpha_n^p(dY_n|_k, dZ_n|_k) = -\sin \theta_n^p dY_n|_k + \cos \theta_n^p dZ_n|_k, \quad (3.17)$$

and the phase residual $A_n^p|_k$ is updated for the next iteration.

When the position errors and phase center elevations have converged for the first along-track position, the algorithm is then run on the next. This time no tie-point is chosen. Instead, the algorithm is initiated for

subsequent along-track positions using the estimated phase-screens from the previous along-track position. This is because it is assumed that phase-screens from one along-track position to the next are strongly correlated with the phase-screens for the neighboring along-track positions due to aircraft inertia.

3.4.1 Optimization strategy

As part of the phase calibration procedure, several optimization problems have to be solved. First, the linked phases are to be determined by maximizing the function in eq. (1.39). Second, the figures of merit in eqs. (3.12) and (3.14) are to be maximized during the iterative procedure described above. For all these optimization problems, we have employed the method of gradient descent, or more correctly gradient ascent, as we are interested in finding the maximum of the given functions in all cases. Gradient ascent is a iterative method for optimizing functions with multiple variables, and can be written as [27]

$$\mathbf{x}_k = \mathbf{x}_{k-1} + \gamma \nabla f(\mathbf{x}) \quad (3.18)$$

where \mathbf{x} is a vector containing the independent variables, $\nabla f(\mathbf{x})$ denotes the gradient of the function $f(\mathbf{x})$, and γ is a constant step size, which determines the rate of ascent.

A drawback of the algorithm is that it is unable to distinguish local maxima from global maxima, however in the case of eq. (1.39), the function been shown to be restrained, when φ_M is kept at zero. eq. (3.14) is inherently ambiguous, so in this case, we have chosen to initialize the sensor position errors at zero, thus the function will be maximized to the peak closest to the origin. The figure of merit eq. (3.12) is not restrained in the same way, so the global maxima is found by first performing a coarse grid search for the maximum and then initializing the algorithm from the result of this. This has proven to be an effective method, but it performs very poorly in the presence of strong elevation ambiguities.

For good measure, the expression for the derivatives and step-sizes used are listed in Table 3.2. The step-sizes have been chosen through experimentation on synthetic examples.

Function	Derivative(s)	Step-size
$F_p(\varphi)$	$\frac{dF_p(\varphi)}{d\varphi_n} = \mathcal{R} \left\{ \sum_m^N j w_{nm} \langle I_{nm} \rangle \exp(j(\varphi_n - \varphi_m)) \right\}$	0.1
$F_t(v^p)$	$\frac{dF_t(v^p)}{dv^p} = \mathcal{R} \left\{ \frac{1}{N} \sum_n^N -jk_n^p \exp(j(A_n^p _{k-1} - k_n^p v^p)) \right\}$	1
$F_s(dY_n, dZ_n)$	$\frac{dF_s(dY_n, dZ_n)}{ddY_n} = \mathcal{R} \left\{ \frac{1}{P} \sum_p^P \frac{4\pi}{\lambda} \sin \theta_n^p \exp \left(j \left(B_n^p _k - \frac{4\pi}{\lambda} (-\sin \theta_n^p dY_n + \cos \theta_n^p dZ_n) \right) \right) \right\}$	0.001
	$\frac{dF_s(dY_n, dZ_n)}{ddZ_n} = \mathcal{R} \left\{ \frac{1}{P} \sum_p^P -\frac{4\pi}{\lambda} \cos \theta_n^p \exp \left(j \left(B_n^p _k - \frac{4\pi}{\lambda} (-\sin \theta_n^p dY_n + \cos \theta_n^p dZ_n) \right) \right) \right\}$	

Table 3.2: Derivatives and step-sizes used in the phase calibration implementation.

3.4.2 Validation on simulated data

The algorithm has been validated in two steps. First, the PCDL iterative algorithm has been tested on simulated point targets without phase-linking and later on simulated volumetric targets with phase-linking included. For both simulations a flat Earth has been assumed. For both simulations, the sensor positions are those shown on Figure 3.7.

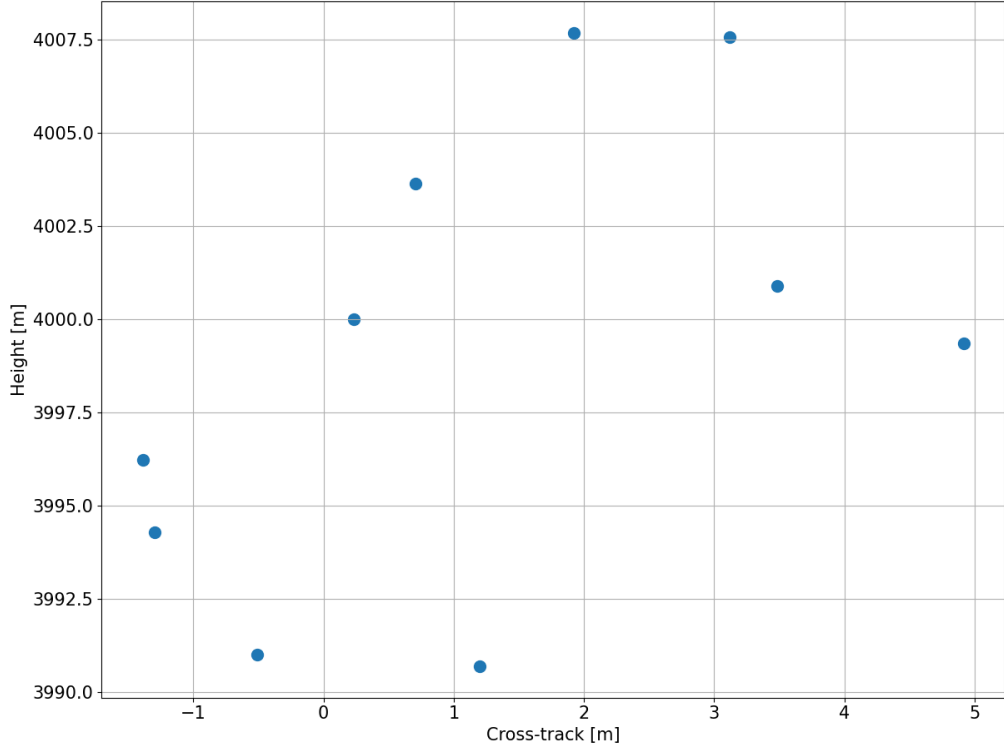


Figure 3.7: Simulated sensor positions for the test

3.4.2.1 Point targets

In this simulation, 100 point targets following a predefined curve at an arbitrary height has been generated. Refraction is not modeled for targets with negative height. The targets has been located at $y \in [\approx 1600 \text{ m}, \approx 3900 \text{ m}]$, and the nominal sensor height is 4000 m.

In order to generate phase screens, random uniformly distributed sensor position errors from $-\lambda$ to λ has been added to the true sensor positions, resulting in erroneous terrain correction of the simulated signals following eq. (1.33). The iterative PCDL algorithm has then been run on the simulated data in order to recreate the correct vertical section or tomogram. Target 60 has been chosen as tie-point. On Figure 3.8 the results of the validation is shown. The tomograms has been generated using the single-look Fourier beamformer (see section 1.2.2.2.1). The amplitude has been normalized for each target. It is clear that the algorithm manages to recreate the tomogram in terms of the vertical profile of the point targets, but the residual roto-translation is also present.

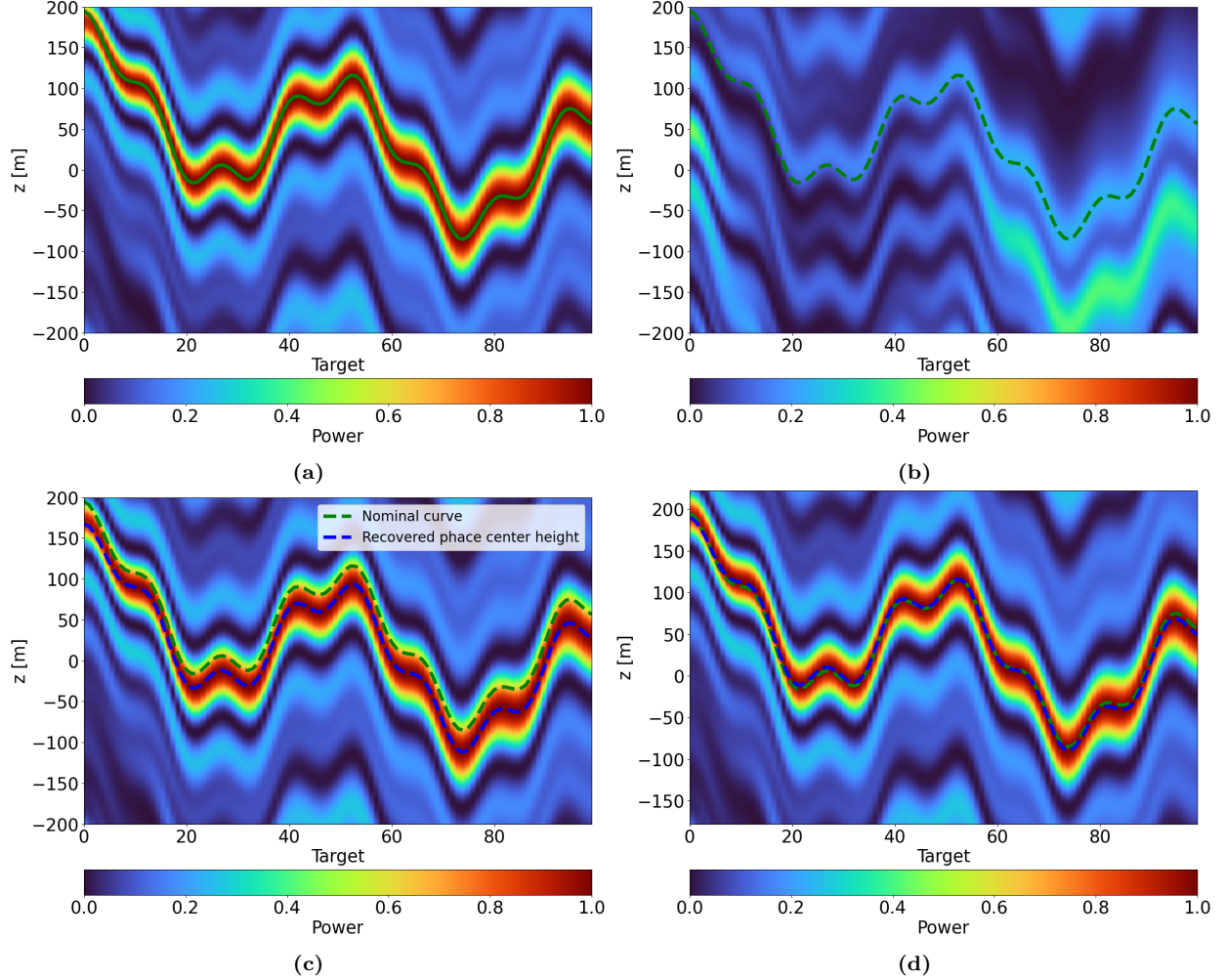


Figure 3.8: (a): Tomogram without sensor position errors. (b): Tomogram with sensor position errors and no phase calibration. (c): Tomogram after phase calibration. (d): Tomogram after phase calibration and with correction for tie-point height.

3.4.2.2 Simulated distributed target

In the second simulation, the sensor positions errors follow a random uniform distribution between $\pm \frac{1}{2}\lambda$. The volumetric target has been simulated by integrating 100 targets for each cross-track position, each with a random height within a nominal curve following a uniform distribution. Furthermore, each point have a random uniformly distributed cross-range off-set from the center of the range cell at the given height of ± 1 m. Finally, the amplitude of each point is given by a normal distribution with $\sigma = 1$ and $\mu = 2$, which is further modulated with an exponential decay given as $\exp\left(\frac{z-\max(\text{curve})}{2\cdot\min(\text{curve})}\right)$. The signal is simulated for 31 along-track positions, where the same acquisition geometry is assumed, but with different realizations of the random scatterers. On Figure 3.9 the result of the simulated example is shown. The tomograms have been generated using the multi-looked Fourier beamformer with 21×21 looks being used in both the phase-linking algorithm and to generate the covariance matrix used for beamforming. 31 equally spaced points has been chosen as targets for the algorithm. It is seen that without phase calibration the tomogram is completely defocused, whereas the vertical structure is almost perfectly reconstructed apart from some minor discrepancies after phase calibration. The residual roto-translation is also very apparent. This analysis shows that our implemented algorithm behaves as expected.

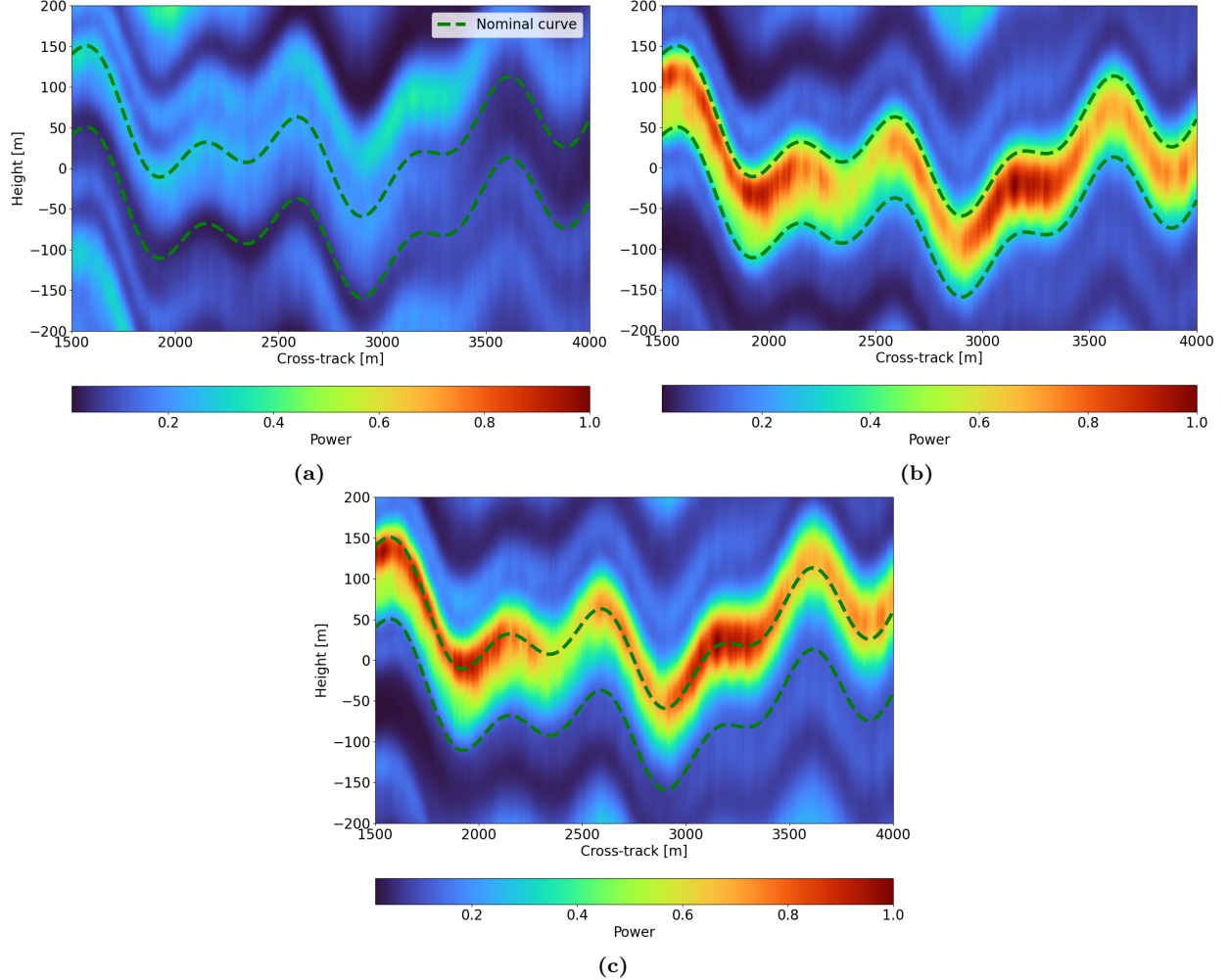


Figure 3.9: (a): Tomogram without correction. (b): Tomogram using true sensor position errors. (c): Tomogram using the PCDL algorithm. Power is normalized to the maximum of the tomograms.

3.4.3 Parameter for PCDL phase calibration of real data

For the phase calibration applied of the real data presented in results, we have chosen 31 equally spaced pixels along each range-line to serve as targets. Furthermore, the interferograms used for phase-linking has been multi-looked with a 30×30 window. As tie point for the first range-line, we have chosen a point, where the surface-signal is strong and volumetric scattering is assumed to be minimal. This means that we with good approximation can assume that φ^T is actually zero, thus eliminating some of the distortion caused by the roto-translation, namely the translation. Track 6, following Figure 2.4 are set as master track. In terms of the rotation, we have chosen to ignore this as well. This will inevitably lead to some errors in the calculated tomographic cube, however we assume that these errors will be small. Furthermore, given the scope of this work, it can be argued that the main focus lies in the implementation of a tomographic processor and analysis of results and not as much in E.g. the extraction of the exact height of certain sub-surface feature, and therefore these errors can be accepted.

3.5 Tomographic processing

When the data has been phase focused and phase-calibrated, the final step of the processing chain, the tomographic processing, can readily be carried out as outlined in Section 1.2.2, as all the components needed are now available. For all tomographic images presented in this work, the DEM-height at a given pixel has been chosen as reference point for the tomographic processing. A multi-looking window of window of 21×21 pixels has been chosen to generate the sample covariance matrix, leading to a resolution of 41×41 m in the along-track/cross-track dimension, while a vertical bin-size of 2 m is used. In the along-track and cross-track dimension, the shown tomographic images are sampled every 5'th pixel corresponding to 10 m in both direction, meaning that all pixels will be correlated in some neighborhood. This oversampling is chosen purely for graphical reason. Track 6, following Figure 2.4 is chosen as master track.

Chapter 4

Results and comparison

In this chapter, the results generated using the implemented tomographic processor will be presented, discussed, and compared to the result presented in [14] using the same dataset. The chapter is organized in the following sections:

- In Section 4.1 our choice to not correct the generated vertical sections for refraction is discussed.
- In Section 4.2 an SLC image of the scene is shown and discussed.
- In Section 4.3 the impact of phase calibration on the real data is presented and discussed.
- In Section 4.4 the coherence and interferometric phase between image pairs are presented and discussed.
- In Section 4.5 simulated Fourier tomograms are compared to real Fourier tomograms in order to access the impact of deviation from nominal flight geometry on the subsequently formed tomograms.
- In Section 4.6 the vertical resolution of the scene is accessed and discussed, and the differences between the Capon and MUSIC spectral estimators are illustrated.
- In Section 4.7 horizontal cuts of the tomographic cubes at different depth are presented, discussed, and compared to similar cuts from [14].
- In Section 4.8 tomograms of the two most predominant subsurface features are presented, and they are compared to optical imagery.
- In Section 4.9 the penetration depth throughout the scene is presented and compared to that in [14].

4.1 Refraction

Throughout this chapter, the shown vertical profiles and height cuts are not corrected for refraction, except in Section 4.9. This means that the presented depths will not be the correct physical depths, but the depths that the scatterers would have, if they were stationed in air. This approach has been chosen, since the scene is located in the ablation zone. This means that a simple approximation of the dielectric properties of the scene is not readily available, as it is not clear how much of the scene is solid ice, wet snow, or dry snow, etc. Therefore, no known errors are corrected, but no new errors are introduced either.

4.2 The scene

As described earlier, the data is acquired at the SHR site at the K-transect. On Figure 4.1 the SLC image for acquisition 1 is presented together with a historical optical image from Google Earth, acquired in August 2012, some months after the SAR data was acquired. The images are shown in the SCH coordinate system,

where the along-track axis is flipped, so that this axis approximately runs from west to east, and the cross-track axis runs from north to south. This will be true for all images presented in this chapter. First, it is observed that the two images seem to resolve the same general features. It is clearly seen that several structures and features are already identifiable from the single acquisition SAR image alone, which will also be identifiable in the tomographic images presented in subsequent sections. Most notably the river-like feature in the south-western part of the image around (Along-track, Cross-track) = (1800 m, 3300 m), and the flower-like feature at (Along-track, Cross-track) = (-900 m, 2500 m). These features also appear on the optical image, especially the river-like feature is very distinct, while the flower-like feature appears very faint.

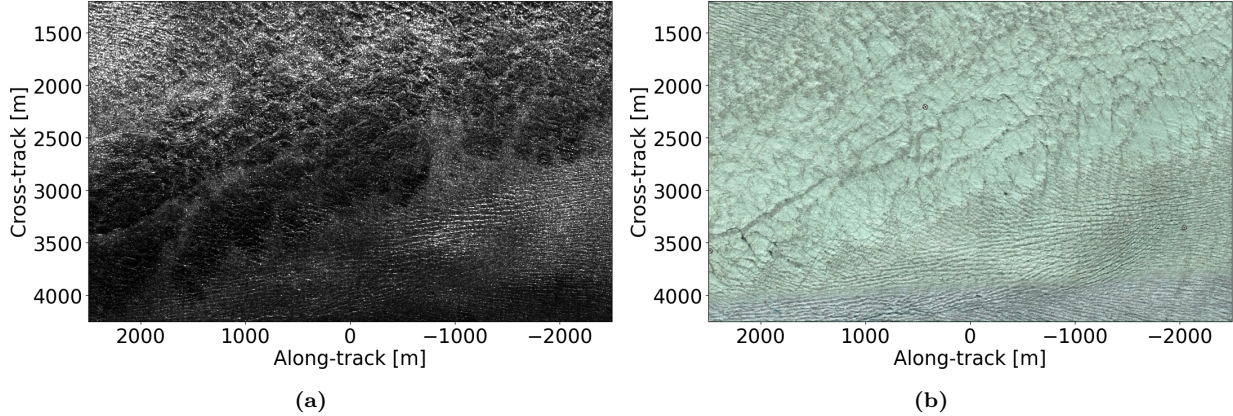


Figure 4.1: (a) The SLC for acquisition 1 containing all elements. (b) Historical optical image from Google Earth from August 2012.

4.3 Phase calibration of real data

In this section, the impact of the phase calibration of the data will be assessed. Figure 4.2 shows tomograms for the along-track position -950 m and cross-track position 2400 m before and after phase calibration with the PCDL algorithm, and using the Capon spectral estimator. It is clear that even before phase calibration, the image is not completely defocused, indicating that the sensor positions are acquired with high precession. However, the phase calibration is observed to lead to a significant improvement of vertical resolution, which is what we would expect. The phase calibrated images will, however, be subject to the roto-translation. That being said, it is not apparent that the surface signal of the phase calibrated images depart more from the reference terrain than the uncalibrated images. On the contrary, it is seen, especially on Figures 4.2c and 4.2d, that the surface signal of the calibrated images are more in agreement with the reference terrain than the uncalibrated images. This misalignment of the uncalibrated images is most likely an artifact of the phase screens present. Last, even though it looks like, the calibrated images represent the scene correctly, it is a fact that they are subject to some errors because of the roto-translation, which has only partially been corrected for. It can be concluded, at least assuming that the DEM represents the surface correctly, that these errors are indeed small. Thus, the phase calibrated images can be assumed to represent the scene with sufficient accuracy even without correction of the roto-translation.

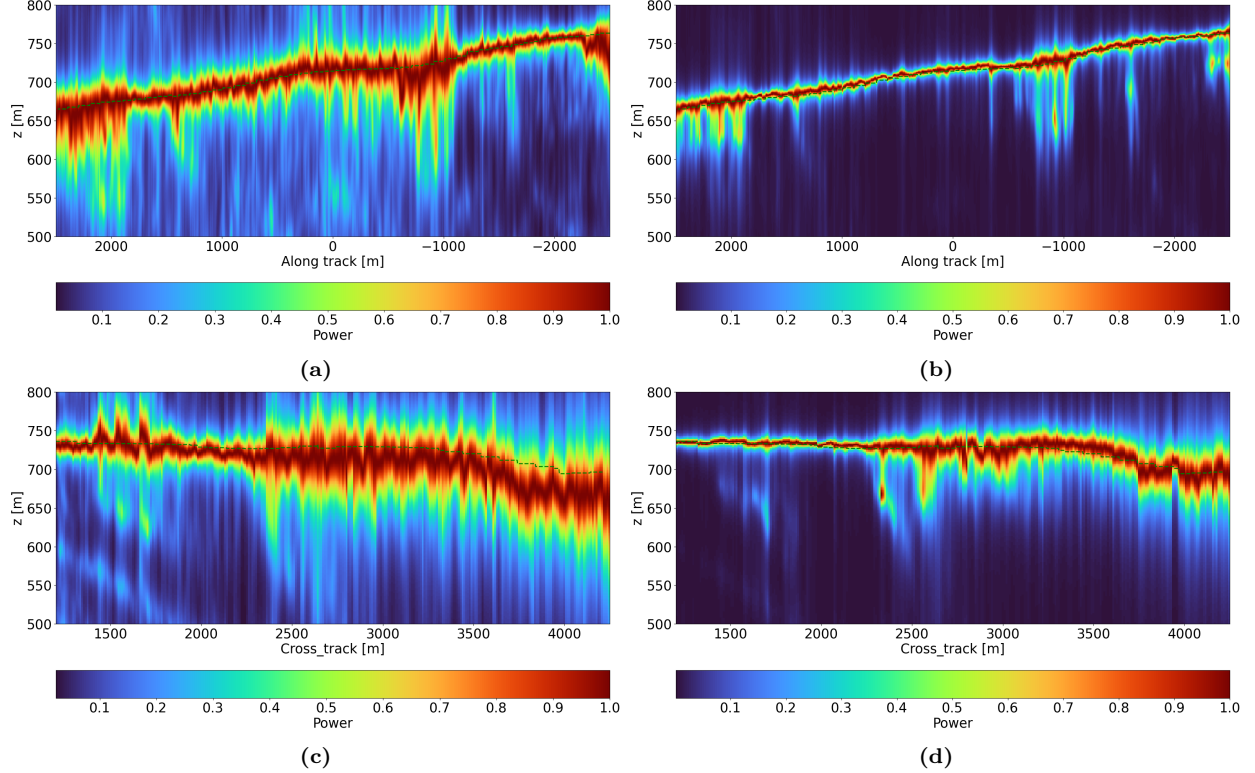


Figure 4.2: Vertical section before and after phase calibration using the Capon beamformer. Power has been normalized at each along-track or cross-track bin. (a),(b): Vertical sections at cross-track 2400 m. (c),(d): Vertical sections at along-track -950 m. The vertical sections correspond to cuts through the flower-like feature.

On Figure 4.3 a histogram of the estimated sensor position errors are shown in terms of fractions of a wavelength. The contribution from the reference sensor, for which the errors are assumed to be zero are removed. Using the PCDL phase calibration approach, it is difficult to conclude anything regarding the real sensor position errors, since the estimated errors are subject to both a roto-translation and ambiguities. However, it might be possible to get a general impression of the magnitude of the errors. It is seen that the errors are generally quite small in terms of a wavelength, and far from the ambiguity distance of half a wavelength. This means that either the errors are indeed very small, or they are larger than half a wavelength and thus subject to ambiguities. However, the fact that no errors approach the ambiguity distance supports the former conclusion. Furthermore, the error magnitudes are observed to be up to approximately 0.15λ corresponding to roughly 10 cm. This is in line with the expected accuracy of the GNSS-solution used to determine the sensor positions, assuming a Real Time Kinematic solution was employed [23][28]. This is especially true, when taking the bias introduced by setting the errors of the master sensor to zero into account.

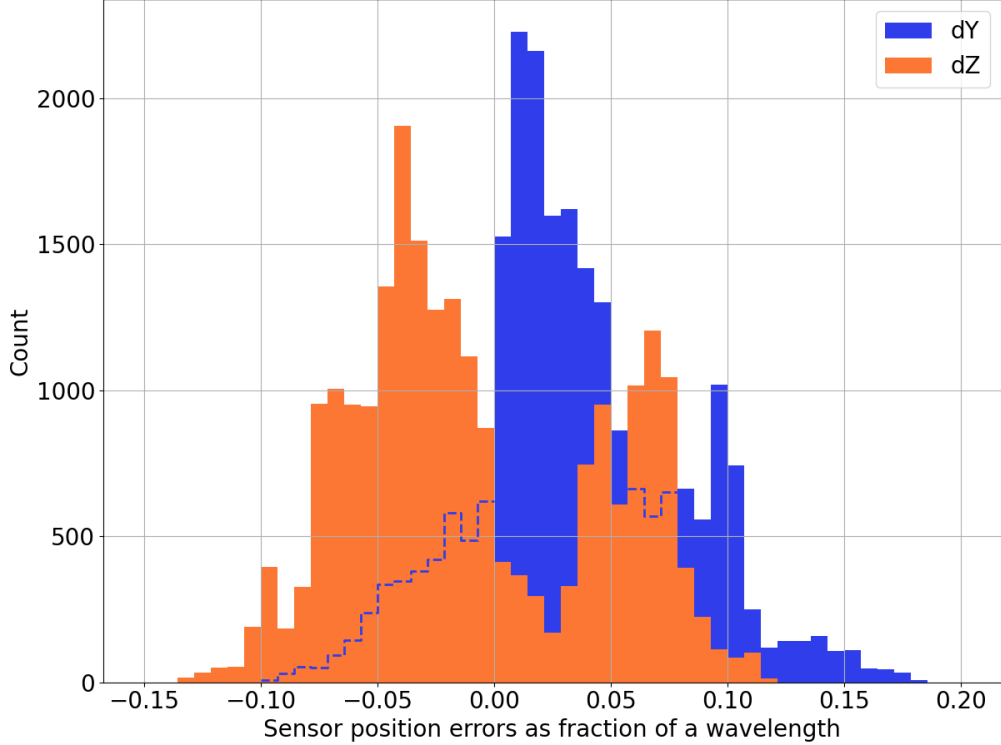


Figure 4.3: Histogram of the estimated sensor position errors in terms of wavelength.
The zero-contribution from the reference sensor has been removed.

4.4 Coherence and interferometric phase

On Figure 4.4 the coherences and terrain-corrected interferometric phases after phase calibration are shown. The plots are generated using 15 multi-looking. It is clear that the scene is generally characterized by high coherence. This is expected, as the imaged scene is a relatively flat and uniform surface without many of the typical phenomena associated with decorrelation. However, subsurface volumetric scattering is expected, which will cause decorrelation at larger baselines. It is seen that for some of the image pairs, decorrelation is clearly present, which in many cases coincides with the river-like and flower-like features described above. This can be interpreted as an indication of volume scattering in these areas. However, the generally high coherence throughout the scene also indicates a shallow penetration depth and strong surface-like targets in large parts of the scene.

Looking at the interferometric phases, it is clear that the phases between image pairs are generally close to zero. This is expected, as the phases has been terrain-corrected. This removes the geometric terms from (1.7) and thus only the atmospheric and decorrelation terms are left (assuming the images has been perfectly terrain-corrected). If we further assume, that atmospheric effects are negligible, then only the decorrelation terms are left. It is seen that the deviations from zero roughly follows the decorrelation patterns. This is expected and further amplifies the conclusion that subsurface volumetric scattering occurs.

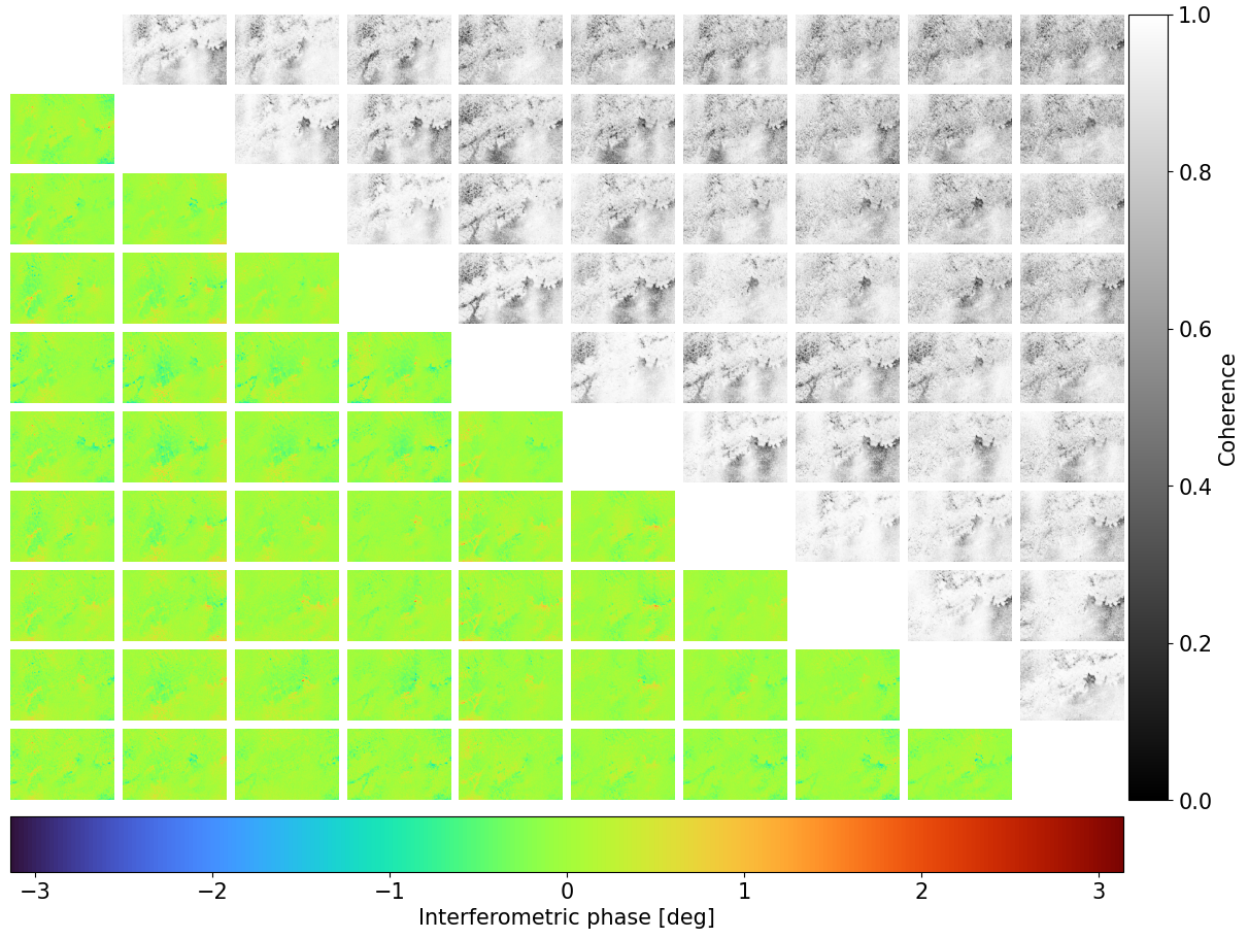


Figure 4.4: Coherence maps above the diagonal and interferometric phases below.
The acquisitions follow the same order as the tracks on Figure 2.4

Another indicator of the underlying scattering mechanisms is the rank of the sample covariance matrix in eq. (1.8). Areas with rank 1 indicates coherent targets associated with surface backscatter. Oppositely, areas with rank 10 (full rank) corresponds to completely decorrelated targets. Intermediate ranks signify some amount of decorrelation as is expected from volume backscatter. It should be noted that although rank analysis indicates whether decorrelation occurs, it does not distinguish between different causes like volumetric decorrelation and temporal decorrelation.

In practice the rank of the sample covariance matrix is assessed as in [24]. This means the rank is calculated for each pixel as the number of eigenvalues larger than 10% of the highest eigenvalue. The resulting rank map is shown in Figure 4.5. It is seen that the rank of most pixels ranges within 1 to 3. This is consistent with the above mentioned high coherence, indicating regions with mostly surface backscatter and shallow penetration (tenths of meters).

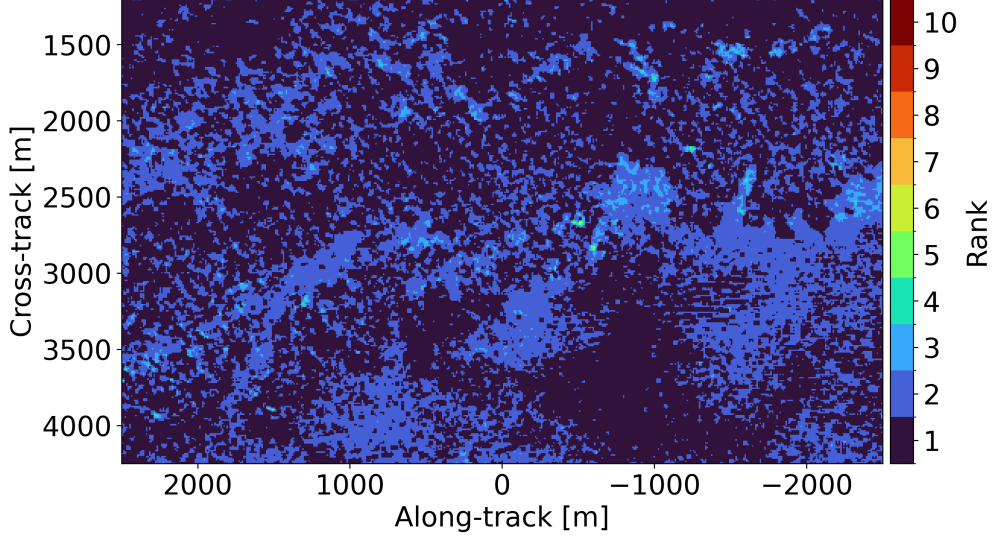


Figure 4.5: Rank of the covariance matrix for each pixel. Rank 1 corresponds to coherent targets (point-like), whereas rank 10 corresponds to complete decorrelation (noise).

4.5 Simulated tomograms

As already shown, the flight tracks, and thus normal baselines, are subject to strong fluctuations throughout the imaged scene. These departures from the ideal acquisition geometry will have an effect on the resulting tomographic images and can lead to artifacts, which might be misinterpreted as targets. In order to assess this, point target responses have been simulated at different cross-track distances. For the simulations, the SCH-geometry has been maintained, so that the curvature of the Earth, although most likely negligible, is included in the simulation. In the simulations, a point target with unit amplitude has been assumed to be present at a height of 700 m, which is also set as the reference point height for all along-track positions. Tomographic processing has then been applied to the simulated signals, employing the Fourier beamformer. On Figure 4.6 the simulated vertical profiles and vertical profiles from the data at cross-track distances, 1500 m, 2500 m, 3500 are shown. These cross-track distances have been chosen in order to represent the imaging scenario at both near, mid, and far range. It is clearly seen how the vertical resolution degrades as a function of range. Furthermore, it is clear how several artifacts are present aside from the expected sidelobes. It is observed that the data-based tomograms are very much in agreement with the simulated point target responses. This behavior is expected under the assumption of a strong surface signal, which makes the the vertical sections approach the point target response. Especially so, given the poor vertical resolution caused by the very small vertical baseline of the experiment. Furthermore, for Figure 4.6e some subsurface signals can be perceived at around along-track 2000 m and - 1000 m, however it is also apparent that the Fourier beamformer does not provide sufficient resolution to resolve the subsurface features in the shown examples. With this, it has been shown that the implemented tomographic processor behaves as it is expected to, through simulation, when it is applied to real data.

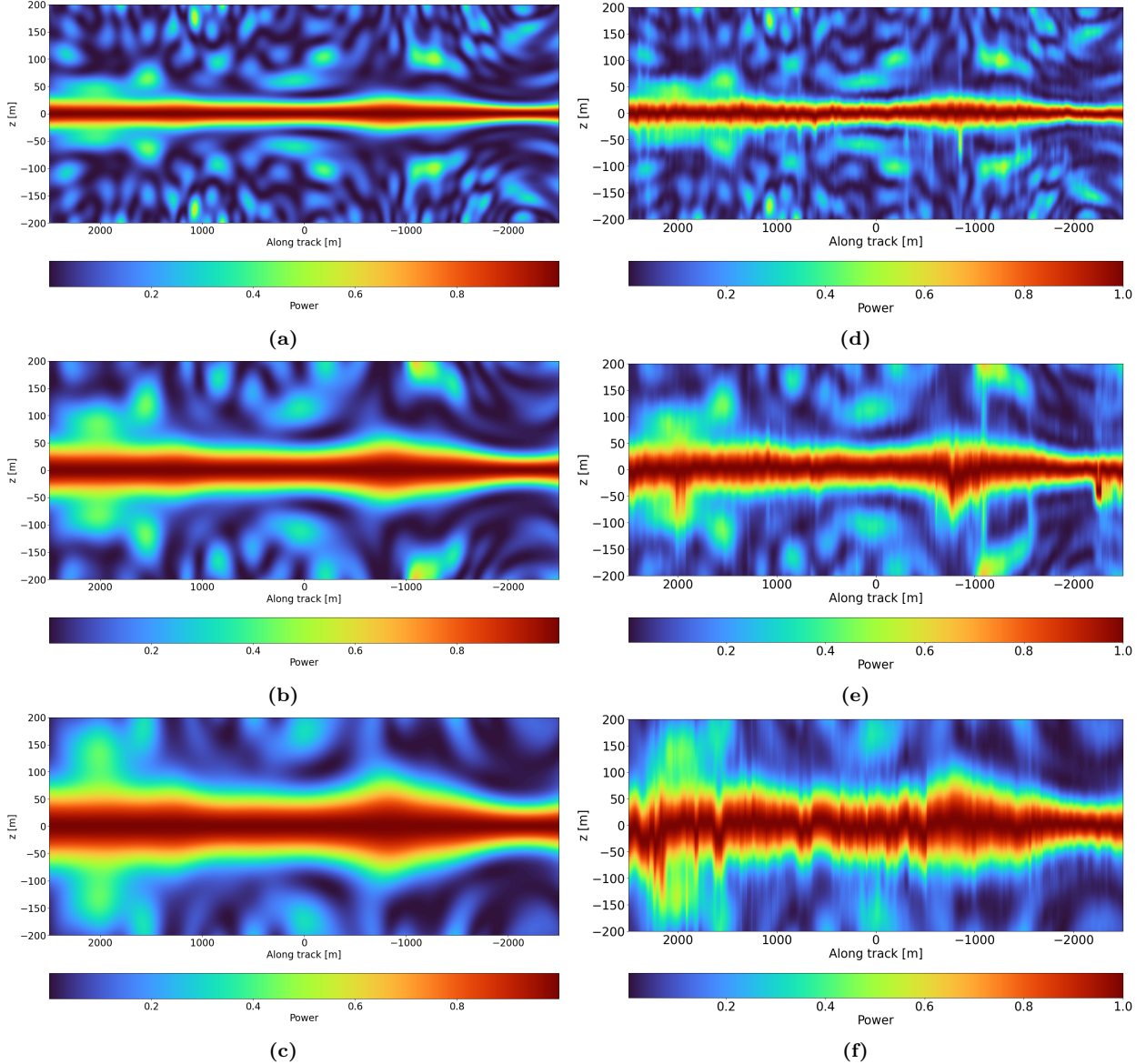


Figure 4.6: (a),(b),(c): Simulated tomograms for cross-track distances 1500 m, 2500 m, and 3500. (d),(e),(f): Data-based tomograms for the same cross-track distances. The vertical height is given with respect to the reference terrain at the given along-track position in order to be comparable to the simulated examples.

4.6 Vertical resolution and super-resolution techniques

In this section, the effectiveness of the implemented Capon and MUSIC super-resolution techniques are discussed. As already shown, the standard Fourier beamformer does not provide sufficient vertical resolution to resolve the subsurface targets. This is both due to the relatively shallow depth of the subsurface targets, putting larger demands on the vertical resolution, but mostly due to the P-band nature of the POLARIS instrument combined with the relatively short baseline used during the acquisitions. Combined with the large variability in Δk_z due to the large deviations from the nominal flight tracks, this results in a vertical resolution, which is quite poor and varies largely throughout the scene. On Figure 4.7 the vertical resolution for the scene is shown. It is seen that the vertical resolution is generally quite poor, considering the expected

penetration depths of about 10-100 m. It even exceeds 250 m in certain areas. Furthermore, it is clear that the vertical resolution is above 100 m in quite a significant portion of the image, especially in the southern part of the image. This illustrates the need for super-resolution techniques. However, even super-resolution techniques will be affected by the poor resolution.

On Figure 4.8 vertical sections generated by the Capon and MUSIC spectral estimator are shown for two along-track lines in the near-range and far-range part of the image, corresponding to the high and low vertical resolution zones. For the MUSIC spectral estimator, the two largest eigenvalues has been assumed to represent the signal subspace, corresponding to a strong point-like surface signal and a weaker volumetric subsurface signal. Looking at the four vertical sections, it is clear that for cross-track 2000 m, a subsurface signal is present at along-track position 2500 m to 1000 m, which both spectral estimators are able to resolve very distinctly. However, the situation is quite different at cross-track 4000 m. Here, the difference between the upper and lower bounds of the signal is much larger with a significant portion of the signal being above the reference terrain, although a subsurface signal is also clearly indicated. This is a result of poor vertical resolution in this region, which hinders the analysis of subsurface signal in this region, as the surface signal generates large sidelobes, that may mistakenly be interpreted as a subsurface signal.

It is observed that the two spectral estimators are generally in agreement, but it is clear that the MUSIC spectral estimator has a better resolution than the Capon estimator, which follows the established theory. However, while the Capon estimator does still contain some radiometric information, the MUSIC estimator does not. This is seen for the vertical sections on Figures 4.8e and 4.8f; the Capon spectral estimator contains a continuous signal throughout the full volumetric scattering region, while the volumetric scattering region using the MUSIC spectral estimator is characterized by a strong surface signal and another stronger signal at the bottom of the region. This is an artifact originating from the fact that MUSIC is a parametric estimator, where in our case, the algorithm has been told that two signals are present. While the general shape of the scattering region is retained, the radiometric information within the region is mostly lost. Thus, the MUSIC spectral estimator is good at indicating, where a signal is present, but it does so without providing radiometric information.

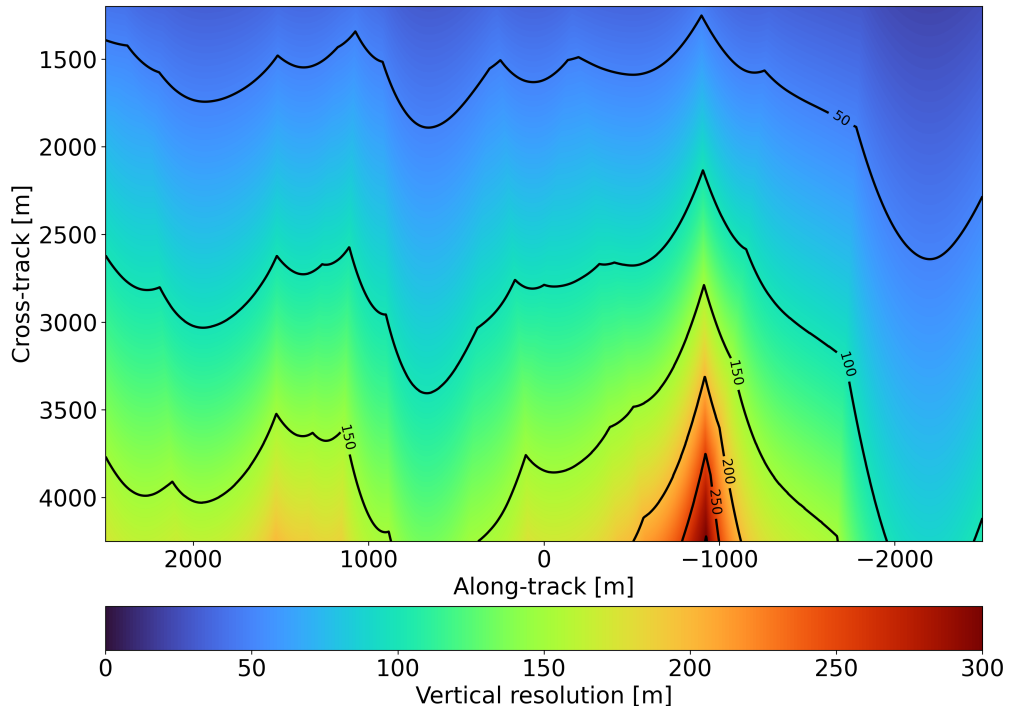


Figure 4.7: Vertical resolution map for the imaged scene.

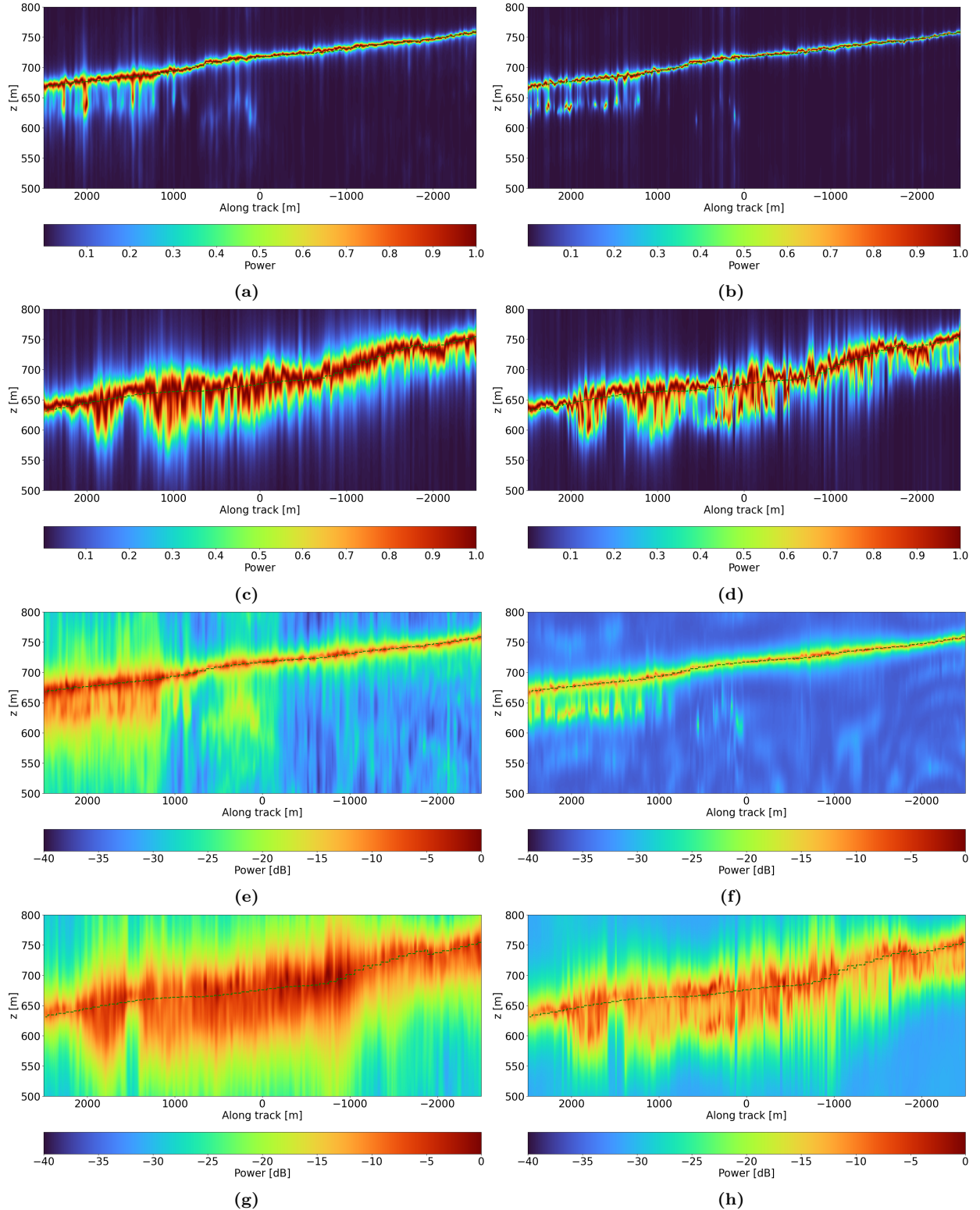


Figure 4.8: (a),(b),(e),(f): Vertical sections generated by the Capon and MUSIC spectral estimators respectively at cross-track 2000 m, corresponding to a high resolution zone. (c),(d),(g),(h): Vertical sections generated by the Capon and MUSIC spectral estimators respectively at cross-track 4000 m, corresponding to a low resolution zone. For the linear sections, vertical power has been normalized at each along-track bin, while for the dB-sections, the power has been normalized to the maximum power of the entire section. The green line denotes the DEM height.

4.7 Tomographic sections

On Figures 4.9 to 4.11 vertical spectral power in dB is shown at different heights with respect to the reference terrain for both the Capon and MUSIC spectral estimator. The power is normalized to the maximum of each tomographic cube. First, it is clear that the dominating signal for both spectral estimators is the surface signal. It is generally observed that the spectral power diminished, as the height above the surface is increased, which is to be expected, as no targets are assumed to be present above the surface, and thus only sidelobes originating from the surface or subsurface signal are expected above surface. This is more distinctly observed for the MUSIC pseudo-spectrum, however the trend is also observed for the Capon spectral estimator. Furthermore, a correlation between the very low-resolution areas shown on Figure 4.7 and the power at 40 m and 80 m is clearly observed in the MUSIC power images. This follows the expectation that poor resolution will result in broader signal responses, giving rise to increased sidelobes in the low-resolution regions of the scene.

Subsurface scattering occurs at the north-western part of the scene and in south-eastern part of the scene, while a large belt in the middle of the scene is dominated by surface scattering, apart from the distinct river-like and flower-like features. It is observed that the subsurface features stand out very distinctly at especially 40 m of depth, while at 80 m of depth, the signal grows fainter, as we go below the the scattering depth. The very limited penetration in large parts of the image can be due to wet snow, impure ice, or other melt phenomena, as surface melt is expected to be present in May at SHR, which severely limits the penetration depth of the radar waves. Whether this reduced penetration is indeed caused by melt phenomena alone, is not clear, as a similar distribution of surface-like and subsurface scattering are observed three years [29], indicating a more complex reason. However, a sufficient analysis is not readily possible without detailed knowledge about the physical structure of the glacier at the site. Furthermore, it is clear that the MUSIC and Capon spectral estimators are again very much in agreement throughout the scene, resolving the same general features (albeit with the differences as discussed previously). Finally, although the results are not completely identical, it is clear that our tomographic processor generates the same general features as presented in [14] and shown on Figure 4.12. This serves to validate our tomographic processor. A direct comparison is difficult, as many factors in the processing chain influence the final results. Most notably, the choice of DEM, azimuth resolution and focusing grid, choices in phase-calibration (e.g. how to deal with the roto-translation), and choice of multi-looking window in the tomographic processing has an impact on the final results. Therefore, the fact that comparable features and structure are seen can be considered a good indication of proper performance.

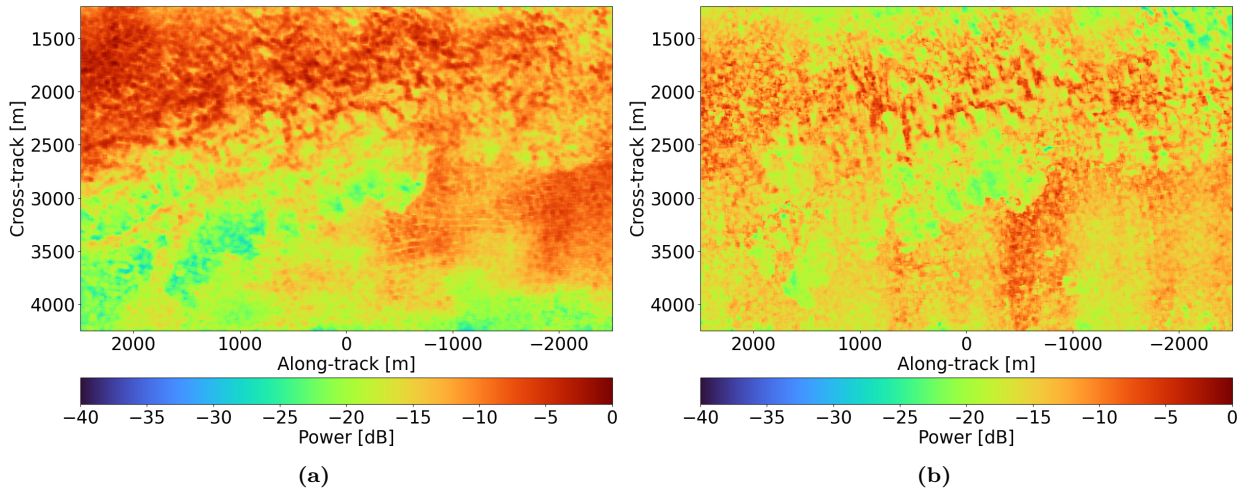


Figure 4.9: (a): Surface signal using the Capon spectral estimator. (b): Surface signal using the MUSIC spectral estimator.

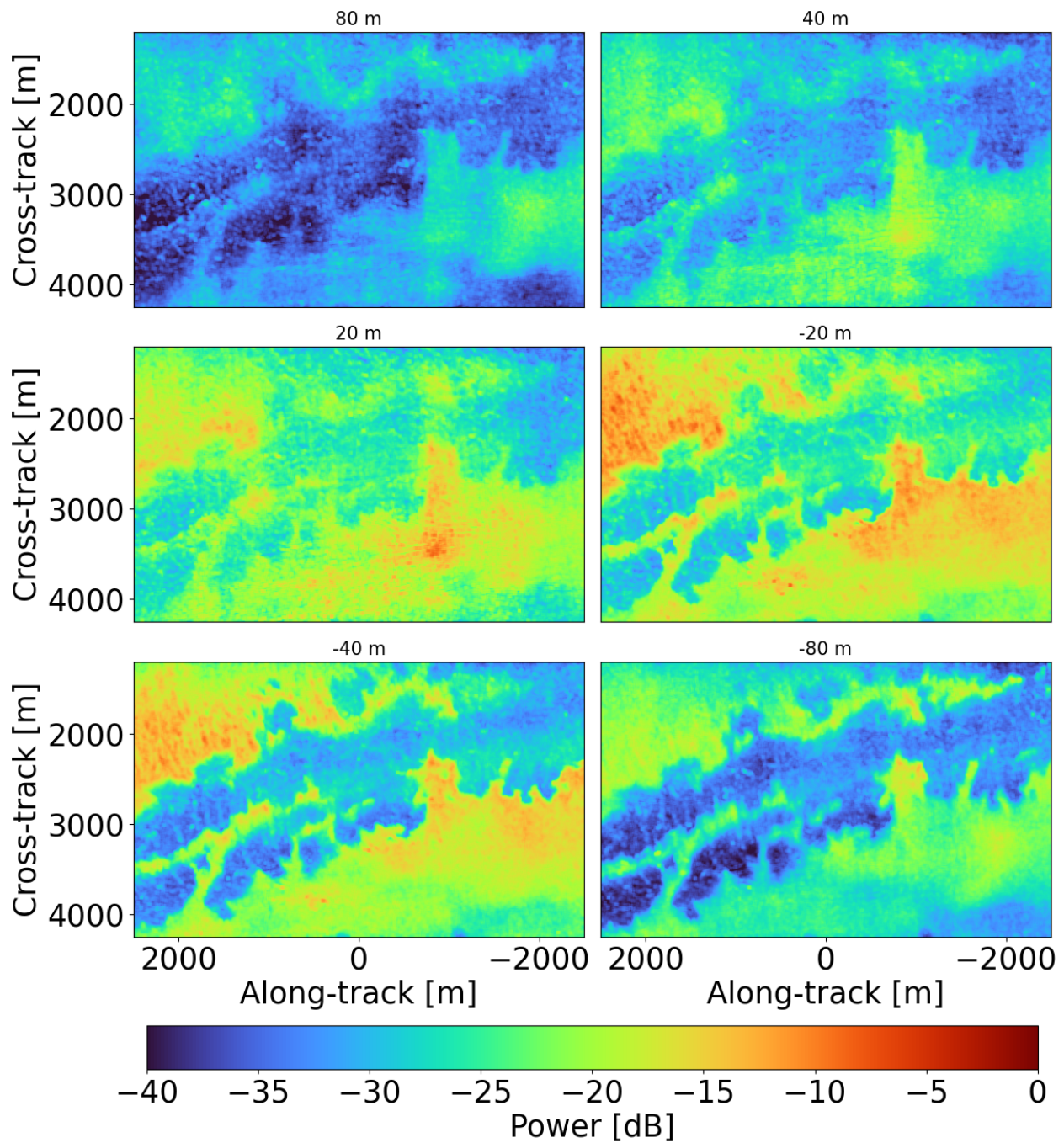


Figure 4.10: Tomographic sections at different heights with respect to the reference height for the Capon spectral estimator.

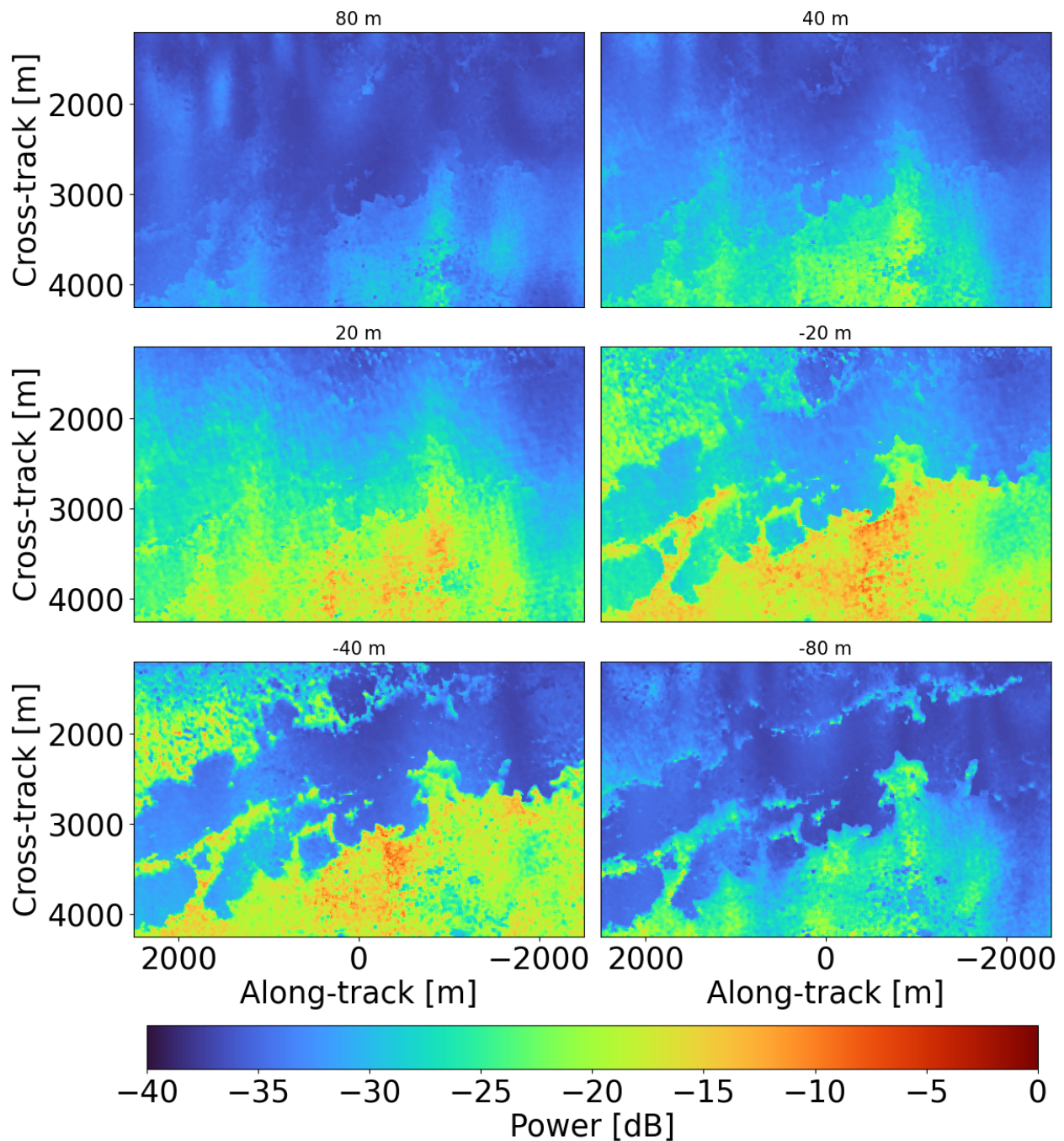


Figure 4.11: Tomographic sections at different heights with respect to the reference height for the MUSIC spectral estimator.

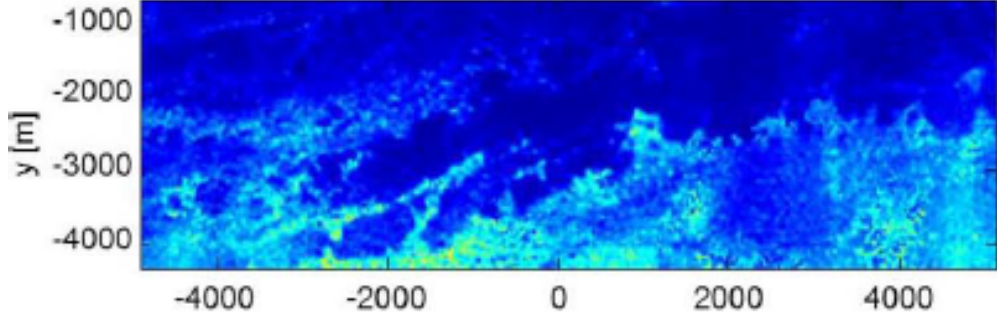
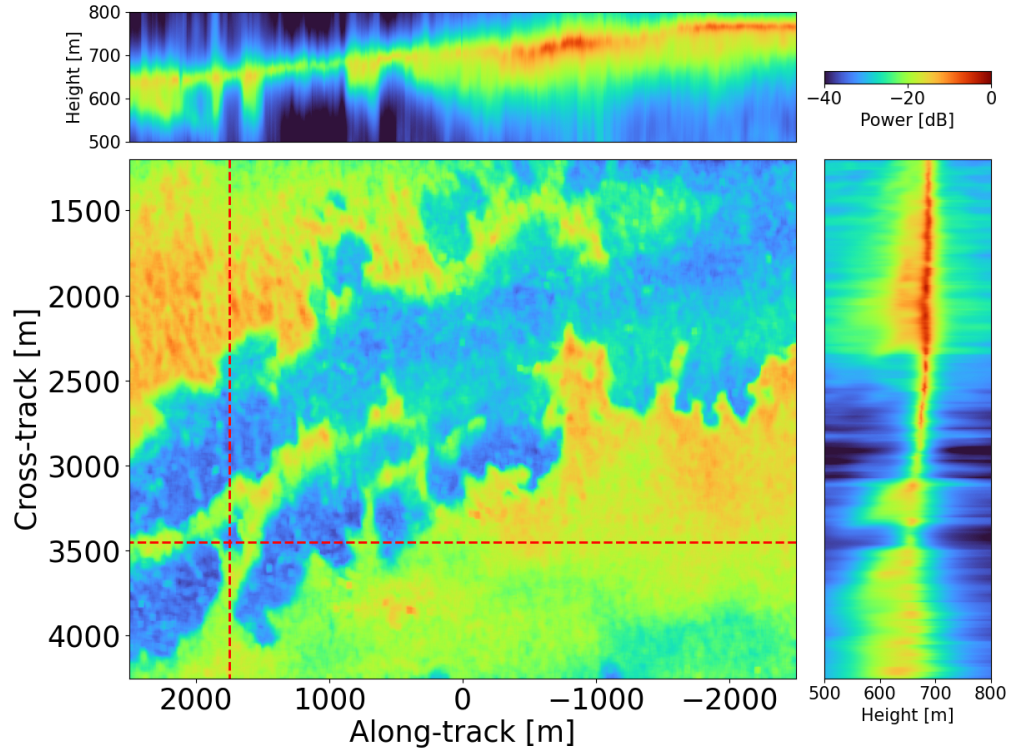


Figure 4.12: Tomographic section from [14] at -20 m, corresponding roughly to -40 m, assuming a simple refraction correction. Note that the power is on a linear scale.

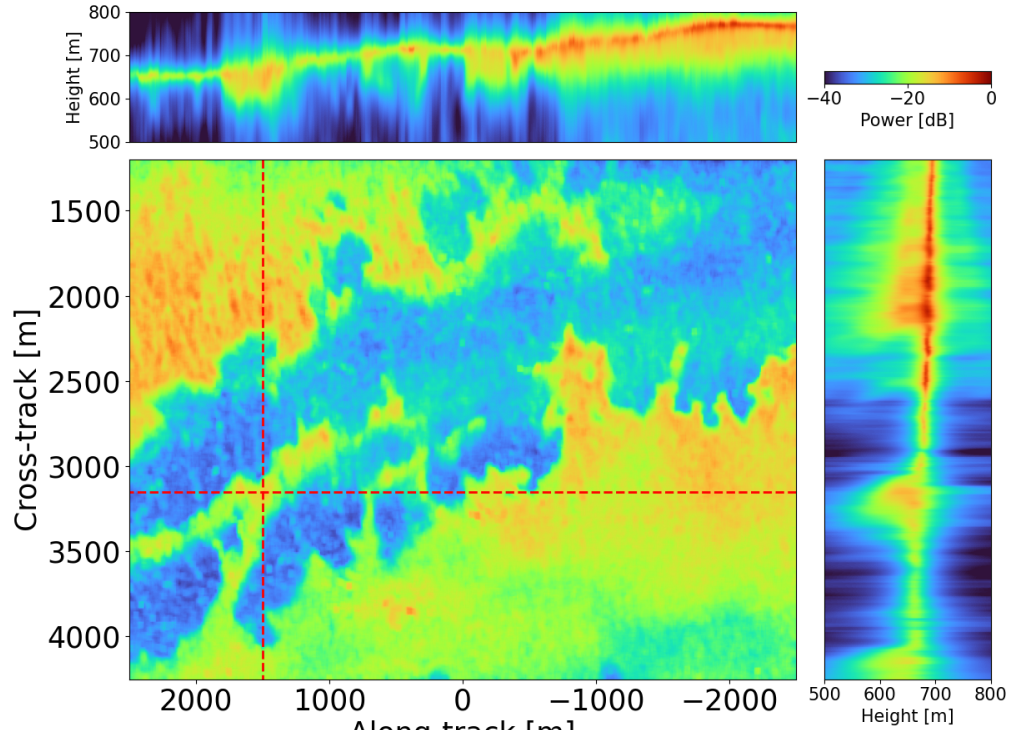
4.8 Feature analysis

In this section the two distinct river-like and flower-like subsurface signal are analyzed.

First, we look at the river-like feature in the south-western part of the image. Figure 4.13 shows Capon tomograms for two distinct locations on the feature together with the height cut at -40m. Looking at these tomograms, it is observed that the feature is indeed a subsurface feature and not a recess or crevasse in topography, as the height spectrum over the feature is continuous containing both a surface contribution and a subsurface contribution. The river-like feature is one of the features identified and discussed in [14]. As already indicated, the feature is identifiable on optical imagery from the scene as well, indicating the presence of a morphological feature in the glacier. On Figure 4.14, similar plots as above are shown for the flower-like feature. These shows that the feature appears thicker than even the surrounding low-resolution volumetric regions. Furthermore, a very faint feature is visible on the optical image in the area, where the flower-like feature is observed, which indicates that this is a morphological feature as well, however it is not as clear as for the river-like feature. Looking these tomograms the abrupt changes in penetration depth across the scene are also very apparent, as they appear almost instantaneous, signifying abrupt changes in the scattering mechanics throughout the scene. Finally, on Figure 4.15 a Google Earth image is shown in the SCH-coordinate system with the outlines of regions with volumetric backscatter superimposed. The outlines are generated using the segmentation presented later in Section 4.9, and the binary mask, for which the outlines are shown, are set as the regions where a signal is present 20 m below the surface. Although the features does not line up perfectly (likely due to poor geo-referencing of the Google Earth image), it is observed that the tomographic features and areas with volumetric scattering are somewhat correlated with features and structures observed in the optical image, relating the observed tomographic features to physical features in the ice sheet. However, since the optical image is not taken at the same time as the SAR data was acquired and due to poor geo-referencing, further analysis is not readily possible.

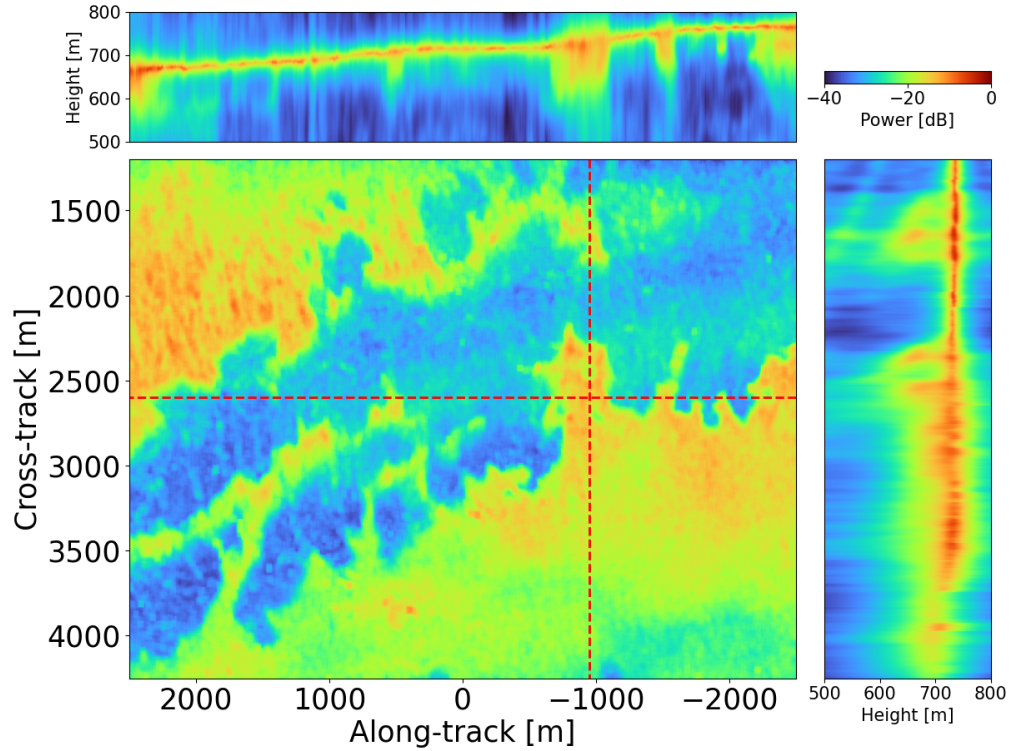


(a)

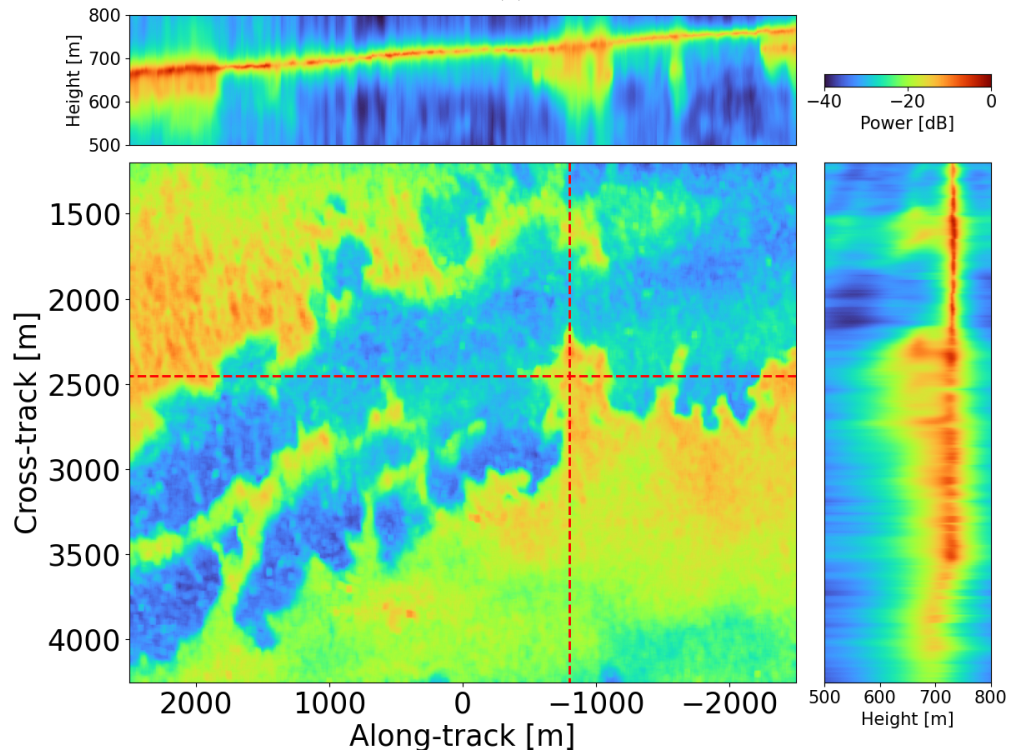


(b)

Figure 4.13: Capon tomograms intersecting the river-like feature. The central image is the signal present at 20 m below the surface. The two bordering images are tomographic sections along the indicated red dashed lines.



(a)



(b)

Figure 4.14: Capon tomograms intersecting the flower-like feature. The central image is the signal present at 20 m below the surface. The two bordering images are tomographic sections along the indicated red dashed lines.

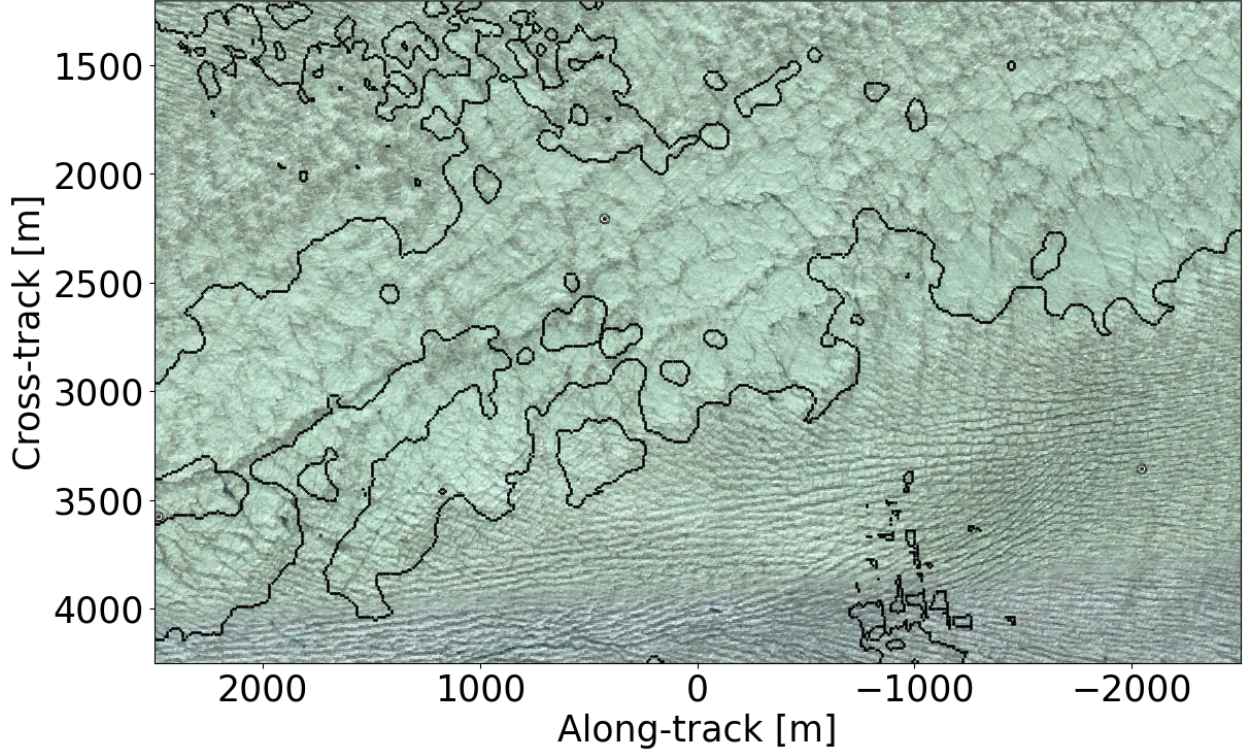


Figure 4.15

Figure 4.16: Google Earth image from the scene in August 2012 with the outline of the areas with volumetric scattering super-imposed (regions where a signal is present 20 m below the surface).

4.9 Scattering depth and deepest return

In this section, we look at the scattering depth, given as the difference between the assumed surface signal and the deepest return, and compare it to that presented in [14]. In this case, we have made a simple refraction correction in order for the values to be comparable. Assuming solid ice with $\varepsilon_r = 3$, the change in propagation velocity from air to ice will be 1.73. Therefore, all heights below the reference surface will be divided by this number. This is a very crude approximation and most likely not representative for the entire scene, but it makes the calculated scattering depths comparable.

To find the extent of the signal, we have used the MUSIC tomographic cube. For each along-track and cross-track position, the power-spectrum has been normalized to the maximum of that particular spectrum. Then, the cube has been low-pass filtered by convolving the cube with a three-dimensional Gaussian kernel with $\sigma = 2$. The upper bounds of the signal is found as the height bin containing the maximum spectral power, while the lower bounds of the signal is found as the deepest height bin with a spectral power larger than the median of the given spectrum + 9 dB. This segmentation method is found to work well through experimentation, but it is not expected to yield a perfect result. The result of this analysis is shown on Figure 4.17. It is clearly seen that the scattering depth shows the same patterns and features identified on the below-surface tomographic sections presented in Section 4.7. This is expected, as the scene is characterized by very distinct regions with and without volumetric scattering, more than different subsurface features. Furthermore, it is seen that the scattering depth is largest around the two features and apart from that in the far-range part of the scene, as a result of the low vertical resolution in this region. Finally, it is seen that this map is largely in agreement with that presented in [14], although they are not an exact match. The range and distribution of scattering depths are generally in agreement, and fits well with the expected 10-100 m penetration depth, but it seems that our calculated scattering depths are generally a bit

larger than those in [14]. However, since the exact methodology employed to generate this map is not available, it can be concluded that the two are reasonably matched, further validating our tomographic processor.

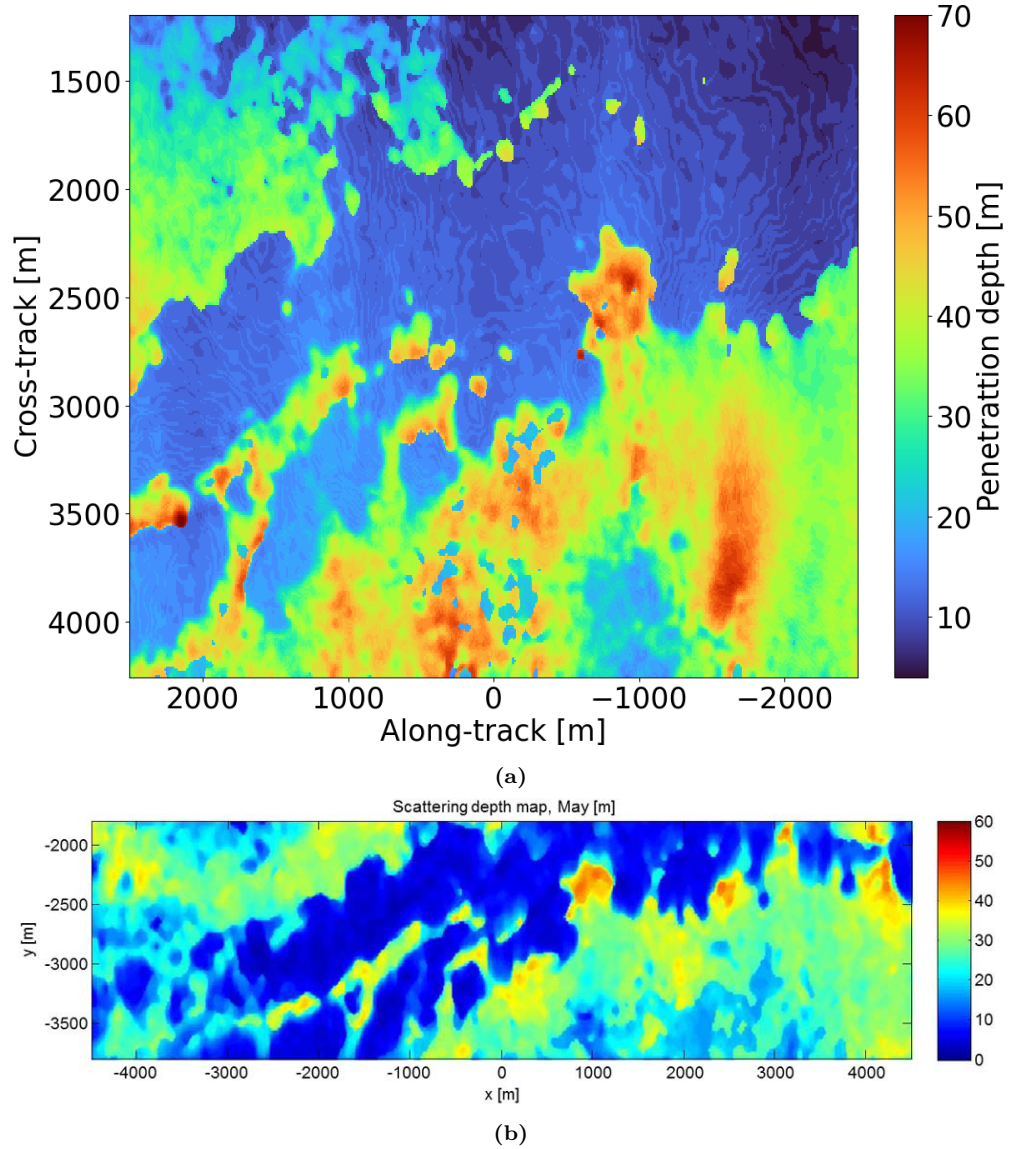


Figure 4.17: (a): Scattering depth map generated using our processor and segmentation method. (b): Scattering depth map presented in [14].

4.10 Future Works

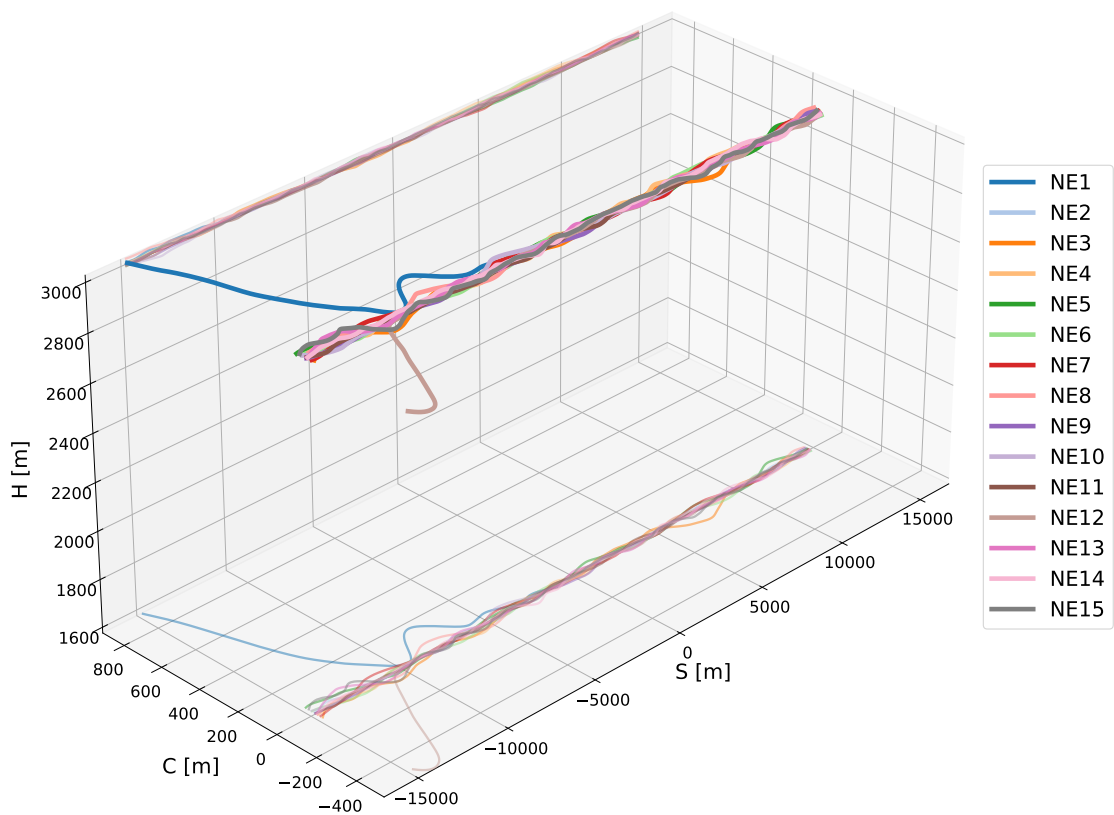
From 11 December 2023 to 14 February 2024, the POLARIS instrument was flown to gather polarimetric TomoSAR data from the Shackleton glacier and at Dome-C station in Antarctica with the goal of testing the suitability of the ice sheets around Dome-C for calibration of the upcoming P-band Earth Explorer mission, BIOMASS. Furthermore, the data at Shackleton ice shelf was gathered to test the feasibility of mapping the Antarctic ice sheets from airborne radar data as before this campaign, no P-band data had ever been acquired in Antarctica.

In this section, we test with simple simulated point target responses, whether or not SAR tomography can be performed on the acquired data, since the flight lines are subject to very large fluctuations and deviations from the nominal acquisition geometry, which might introduce significant artifacts to the subsequent tomographic images. The tomographic data over the Shackleton glacier was gathered from a north-east (NE) direction and a south-west (SW) direction. In both directions, data was acquired for 15 flight tracks. On Figure 4.18 the flight tracks for the two passes are shown. It is observed, how the flight tracks are indeed very unstructured with very large deviations, especially in the cross-track direction, and most notable in the North-east direction, where deviations up to 800 m are observed. It is also worth noting the much larger and unstable vertical baseline as compared to the data from SHR, which will give rise to larger normal baselines providing a much better vertical resolution, which is very desirable. Especially, since the low vertical resolution has been shown to be a major hindrance for the analysis of the data acquired over SHR.

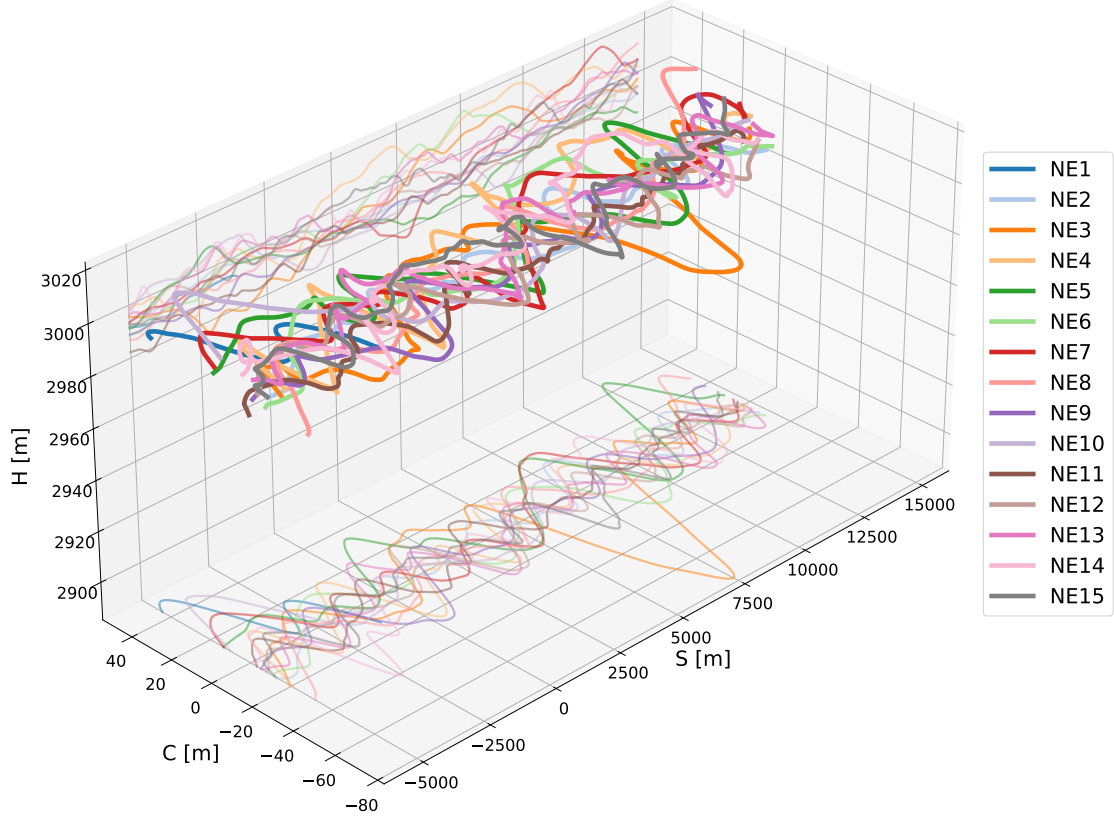
Fourier point target responses has been simulated for both directions from -15000 m to 15000 m in the along-track direction. These are shown on Figure 4.19. The target is assumed to be located at 2500 m cross-track and at a height of 500 m corresponding roughly to the mean glacier elevation. In the simulations the curvature of the earth has been taken into account. It is clearly observed, that the large fluctuations in acquisition geometry gives rise to some very peculiar artifacts, which are most noticeable in the north-east direction. However, it is also observed that tomographic processing should be possible for at least very large parts of the scene, though it might be necessary to exclude the regions with the strongest artifacts in order to gain meaningful results. Last, the vertical resolution is shown to be quite good throughout the scene for both direction, but it is subject to larger fluctuations.

Additionally, the fact that polarimetric data was acquired during this campaign allows the application of other complimentary SAR techniques such as Polarimetric SAR Interferometry, PolInSAR, using the Random Volume Under Ground model, providing additional information about the vertical distribution of scattering mechanism. This will, in principle, allow for a synthesis of the two techniques yielding a better understanding of subsurface scattering than what would be achieved with tomographic SAR or PolInSAR alone. Furthermore, the acquisition of polarimetric tomographic data allows for the application of model-based tomoSAR techniques, which, in theory, can make it possible to decompose the scattering mechanism into e.g. a surface and a ice shelf bottom component [30]. Thereby providing solid grounds for future work.

Furthermore, several improvements to the exiting tomographic framework could be added. First of all, refraction could be taken into account during the azimuth focusing, and this might indeed be needed in order to focus the scene correctly, in regions where large penetration depths are expected. Furthermore, a method for robustly correcting for the roto-translation due to phase calibration would also be a welcome improvement.



(a)



(b)

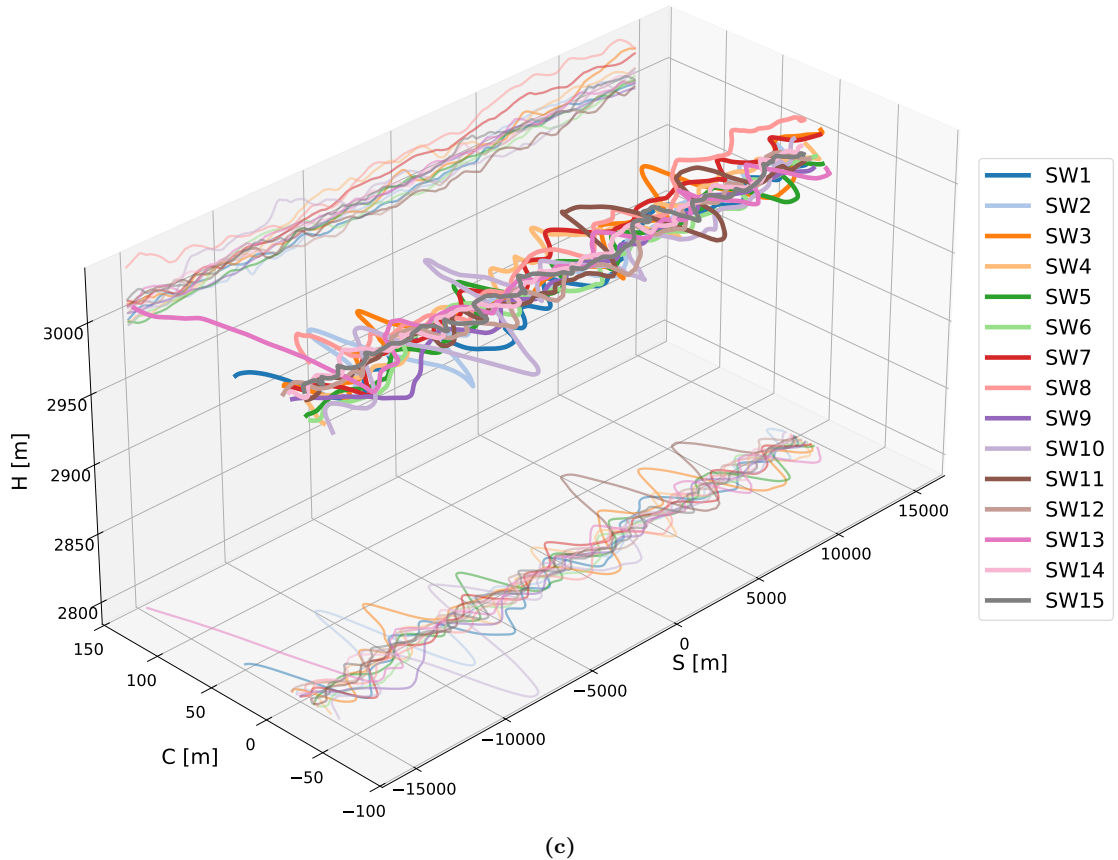


Figure 4.18: Flight tracks from Antarctica. (a) NE direction. (b) NE direction for S-coordinate -5km to 15km. (c) SW direction.

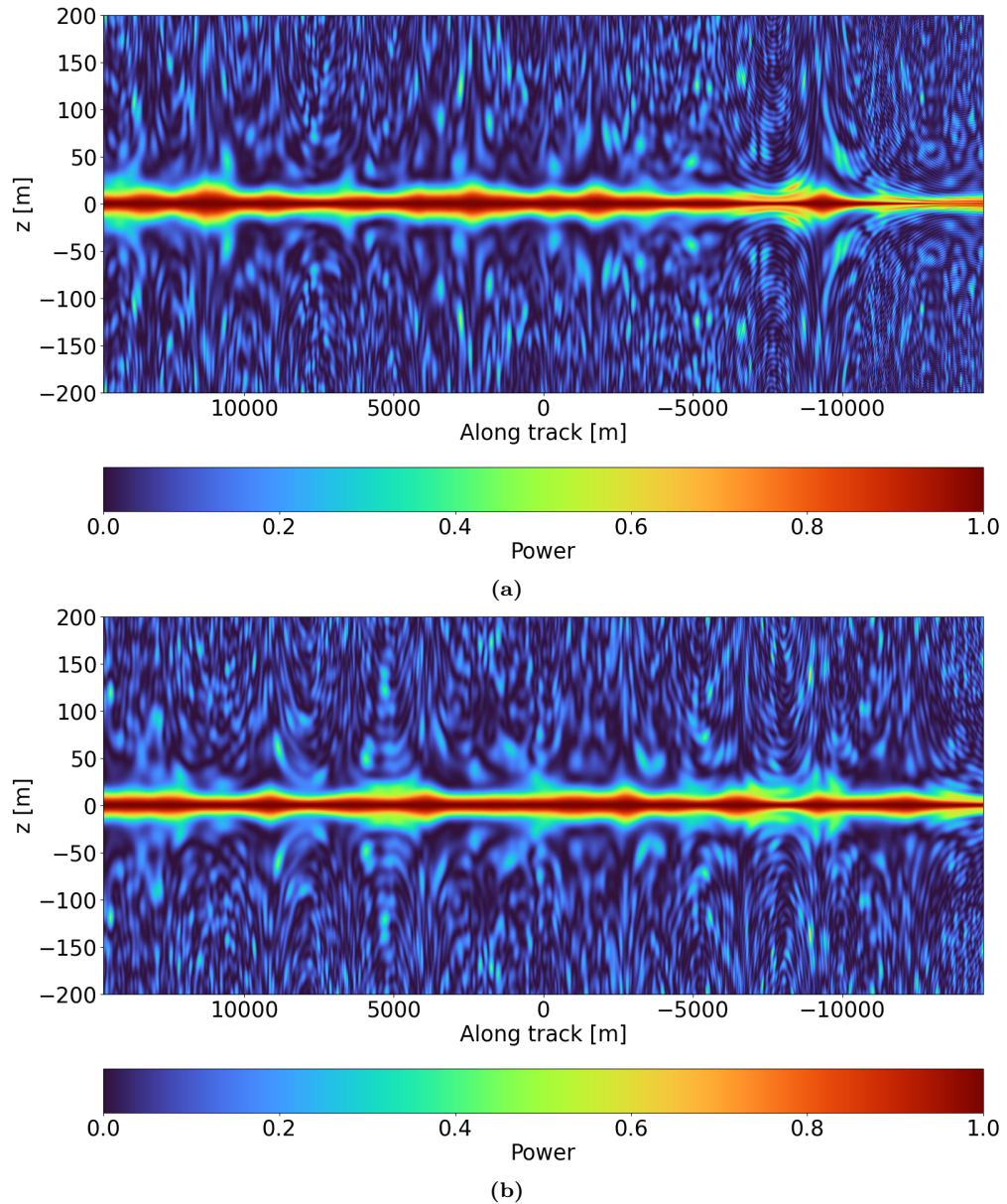


Figure 4.19: Simulated Fourier tomograms for the data collected over the Shackleton glacier. (a): NE acquisition. (b): SW direction

Chapter 5

Conclusion

In this work, a tomographic processing chain has been implemented. It is tested on level 0c single-polarization HH data acquired by the POLARIS SAR at the SHR site at the K-transect in Greenland acquired in May 2012. All processing steps has been documented, discussed and validated, including azimuth focusing with the Direct Back-projection algorithm, phase calibration with the Phase Center Double Localization algorithm, and finally tomographic processing using Fourier beamforming, Capon and MUSIC spectral estimators.

It has been shown that the implemented processor is indeed capable of generating tomographic cubes from the given multi-baseline SAR data. These have subsequently been validated in several ways. First, it has been shown that the Fourier beamformer behaves as expected through simulations using the real flight tracks at multiple cross-track distances (and thus ranges). In the same manner, it has been shown that the Fourier beamformer does not provide sufficient vertical resolution to resolve anything, but the surface response.

Second, the Capon and MUSIC spectral estimators has been compared at two different cross-track distances, in the higher and lower resolution part of the image. It has been shown that they behave as is expected according to theory. Namely, that the MUSIC spectral estimator provides better resolution at the expense of radiometric accuracy.

Third, tomographic sections and scattering depth has been shown and compared to those presented in [14], using the same dataset. It is shown that although the results from this work is not identical to those presented in the paper, the same general features and structures are reproduced. Small discrepancies are easily explained by differences in the methodology. These include the choice of DEM, focusing grid, azimuth resolution, and presumably most predominantly the implementation of phase calibration and the treatment of the errors introduced by this. Thus, it can be concluded that the implemented processing chain is sound, and the general framework can be reused for future work.

The presented tomographic imagery shows that the imaged scene is generally characterized by surface scattering and very shallow penetration in major regions. Most predominantly in a belt running approximately south-west to north-east, while volume scattering occurs in the north-western and south-eastern part of the image. However, two very distinct subsurface features appear in the image. These features are not only identifiable three years later, but they also coincide with feature identifiable on optical imagery, thus indicating that these features are related to physical features in the ice sheet. Furthermore, the changes in penetration depth has been shown to coincide roughly with changes on the surface as observed in the optical image. However, a more complete study of the correlation would require more knowledge about the physical properties of the ice sheet, especially since the data is acquired in May, where surface melt would be expected, which severely limits the penetration depth of radar waves.

Finally, simulated tomograms for polarimetric POLARIS data gathered at the Shackleton ice shelf in Antarctica has been generated in order to test the feasibility of tomographic processing of the acquired data. Here, it is shown that the simulated point target response is generally good with good vertical resolution due to larger vertical baselines when compared to the data from SHR. However, very large fluctuations in the flight geometry are present giving rise to significant artifacts. These artifacts may potentially hinder the validity of the tomographic results in specific parts of the scene. All things considered, TomoSAR processing seems feasible at Antarctica, thus laying the grounds for future work.

Bibliography

- [1] NASA. "Satellites see unprecedeted Greenland ice sheet surface melt". In: *NASA News release 12-249* (2012).
- [2] NASA. *nasa data peers into greenlands ice sheet*. URL: nasa.gov/content/goddard/nasa-data-peersinto-%20greenlands-ice-sheet/.
- [3] X. Wu. "Ice sheet bed mapping with airborne SAR tomography". In: *IEEE Trans. Geosci. Remote Sens* 49 (10 2011), pp. 3791–3802.
- [4] F. Gini and M. Montanari. "Layover solution in multibaseline SAR interferometry". In: *IEEE Trans. Aerosp. Electron. Syst* 38 (4 2002), pp. 1344–1356.
- [5] J. J. Mohr and A. Kusk. *SAR Light an introduction to Synthetic Aperture Radar*. Mar. 2006.
- [6] J. Dall. "Imaging Radar Speckle". 30350 Remote Sensing. Lecture material from DTU course. URL: <https://kurser.dtu.dk/course/30350>.
- [7] S. Hensley et al. *Improved Processing of AIRSAR Data Based on the GeoSAR Processor*. Tech. rep. 4800 Oak Grove Drive Pasadena, California 91109. MS 300-235: Jet Propulsion Laboratory, 2002.
- [8] J.P.M. Boncori. "Synthetic Aperture Radar Interferometry". 30350 Remote Sensing. Lecture material from DTU course. URL: <https://kurser.dtu.dk/course/30350>.
- [9] F. Gini, F. Lombardini, and M. Montanari. "Layover Solution in Multibaseline SAR Interferometry". In: *IEEE transactions on aerospace and electronic systems* 38.4 (2002), pp. 1344–1356.
- [10] L. Ferro-Famil. "Spectral Analysis (Specan) techniques". ESA Polarimetric Training Course 2023. Presentation material from ETA training course. Toulouse, 2023. URL: <https://polarimetrycourse2023.esa.int/>.
- [11] S. Tebaldini et al. "POLARIMETRIC SAR TOMOGRAPHY FOR THE CHARACTERIZATION OF FORESTED AREAS". In: *IGARSS 2021 - 2021 IEEE International Geoscience and Remote Sensing Symposium* (2021), pp. 1534–1537.
- [12] Tebaldini et. al. "Phase Calibration of Airborne Tomographic SAR Data via Phase Center Double Localization". In: *IEEE TRANSACTIONS ON GEOSCIENCE AND REMOTE SENSING* (2015).
- [13] Eindhoven University of Technology. *Parametric spectral estimation*. URL: https://spseducation.tue.nl/disciplines/statistical/statisticsignalprocessing_spectrum_parametric/.
- [14] Banda F., J. Dall, and S. Tebaldini. "Single and Multipolarimetric P-Band SAR Tomography of Sub-surface Ice Structure". In: *IEEE Transactions on Geoscience and Remote Sensing* 54.5 (May 2016).
- [15] U. Nickel. "Algebraic formulation of Kumaresan-Tufts superresolution method, showing relation to ME and MUSIC methods". In: *Iee Proceedings, Part F: Communications, Radar and Signal Processing* 135 (1 1988), pp. 7–10.
- [16] P. Stoica and R. Moses. "Spectral Analysis of Signals". In: Prentice Hall, Inc., 2005. Chap. Pisarenko and MUSIC methods.
- [17] Mianzhi Wang. *doatools.py*. <https://github.com/morriswmz/doatools.py?tab=readme-ov-file>. 2018.
- [18] S. Tebaldini. "SAR BASICS & SAR TOMOGRAPHY THEORY". ESA Polarimetric Training Course 2023. Presentation material from ETA training course. Toulouse, 2023. URL: <https://polarimetrycourse2023.esa.int/>.
- [19] Maciejewski et al. "Nonuniform sampling and spectral aliasing". In: *Journal of Magnetic Resonance* 199 (1 2009), pp. 88–93.

- [20] M. Gay and L. Ferro-Famil. “Penetration depth of Synthetic Aperture Radar signals in ice and snow: an analytical approach”. In: *Workshop Remote Sensing and Modeling of Surface Properties*. Mar. 2016.
- [21] Ivanenko Y. et al. “Interpolation Methods with Phase Control for Backprojection of Complex-Valued SAR Data”. In: *Sensors* (2022).
- [22] A. Kusk, J. Dall, and S. S. Kristensen. *POLARIS User Data Products*. Tech. rep. Version 13.02. Technical University of Denmark, Feb. 2013.
- [23] A. Kusk and J. Dall. *ICESAR 2012 Campaign Data Inventory*. Tech. rep. ESA Contract No. 4000106112 /12/NL/FK. Version 1.1. Technical University of Denmark, June 2013.
- [24] J. Dall et al. *Technical Assistance during the 2012 ICESAR Validation Campaign; Final Report*. Tech. rep. 4000106112/12/NL/FK. Technical University of Denmark, Politecnico di Milano, and Utrecht University, June 2013.
- [25] German Aerospace Center. *TanDEM-X - Digital Elevation Model (DEM) - Global, 90m*. URL: <https://download.geoservice.dlr.de/TDM90/>.
- [26] A. Kusk and J. Dall. “SAR FOCUSING OF P-BAND ICE SOUNDING DATA USING BACK-PROJECTION”. In: *International Geoscience and Remote Sensing Symposium proceedings* (2010).
- [27] Jeff M. Phillips. “Mathematical Foundations for Data Analysis”. In: University of Utah, 2021. Chap. 6 Gradient Descent, pp. 125–142.
- [28] Kaderábek et al. “Comparison of Four RTK Receivers Operating in the Static and Dynamic Modes Using Measurement Robotic Arm”. In: *Sensors* (2021).
- [29] Parella et al. “COMPLEMENTARITY AND POTENTIAL OF POLSAR AND TOMOSAR FOR GLACIER SUBSURFACE CHARACTERIZATION”. In: *2021 IEEE International Geoscience and Remote Sensing Symposium IGARSS*. 2021.
- [30] Hossein Aghababaee and Mahmod Reza Sahebi. “Model-Based Target Scattering Decomposition of Polarimetric SAR Tomography”. In: *IEEE TRANSACTIONS ON GEOSCIENCE AND REMOTE SENSING* 56 (FEBRUARY 2018).
- [31] E.J. Krakiwsky and D.B. Thomson. *Geodetic Position Computations*. Feb. 1974.

Appendix A

SCH Coordinate Conversions

A.1 SCH to ECEF

Formulas in this appendix are based on [7], but rewritten for improved notation clarity. Some intermediate calculations are also explained in greater detail.

Mapping coordinates, (S, C, H) , are converted to ECEF coordinates, (x, y, z) , through an intermediate rectangular coordinate system, (x', y', z') , given by

$$\begin{bmatrix} x' \\ y' \\ z' \end{bmatrix} = \begin{bmatrix} (R_a + H) \cos\left(\frac{C}{R_a}\right) \cos\left(\frac{S}{R_a}\right) \\ (R_a + H) \cos\left(\frac{C}{R_a}\right) \sin\left(\frac{S}{R_a}\right) \\ (R_a + H) \sin\left(\frac{C}{R_a}\right) \end{bmatrix} \quad (\text{A.1})$$

To understand what R_a is, one has to understand that the radar mapping coordinates are defined relative to a sphere approximating the ellipsoid locally at some reference point¹ (θ_0, λ_0) . This approximating sphere has a radius, R_a , which is the radius of the curvature in the along track direction, and is given by

$$R_a = \frac{R_N(\lambda_0) R_M(\lambda_0)}{R_N(\lambda_0) \cos^2(\eta_0) + R_M(\lambda_0) \sin^2(\eta_0)} \quad (\text{A.2})$$

where η_0 is the heading of the radar platform, $R_N(\lambda_0)$ is the radius of curvature in the prime vertical at the reference latitude λ_0 , and $R_M(\lambda_0)$ is the radius of curvature in the meridian at the reference². Expression (A.2) is also referred to as the Euler radius of curvature in differential geometry [31]. The intermediate (x', y', z') -coordinates are converted to ECEF (x, y, z) -coordinates through a transformation to East North Up coordinates, (e, n, u) , as

$$\begin{bmatrix} x \\ y \\ z \end{bmatrix} = \mathbf{M}_{enu}^{xyz} \mathbf{M}_{x'y'z'}^{enu} \begin{bmatrix} x' \\ y' \\ z' \end{bmatrix} + \mathbf{o}_{x'y'z'}^{xyz} \quad (\text{A.3})$$

The transformation matrices are given by

$$\mathbf{M}_{enu}^{xyz} = \begin{bmatrix} -\sin(\theta_0) & -\sin(\lambda_0) \cos(\theta_0) & \cos(\lambda_0) \cos(\theta_0) \\ \cos(\theta_0) & -\sin(\lambda_0) \sin(\theta_0) & \cos(\lambda_0) \sin(\theta_0) \\ 0 & \cos(\lambda_0) & \sin(\lambda_0) \end{bmatrix}, \quad \mathbf{M}_{x'y'z'}^{enu} = \begin{bmatrix} 0 & \sin(\eta_0) & -\cos(\eta_0) \\ 0 & \cos(\eta_0) & \sin(\eta_0) \\ 1 & 0 & 0 \end{bmatrix} \quad (\text{A.4})$$

and the translation vector is

$$\mathbf{o}_{x'y'z'}^{xyz} = \mathbf{p} - R_a \mathbf{u}|_{xyz} \quad (\text{A.5})$$

¹The notation used for latitude and longitude varies in scientific literature. In this section, we use the naming convention found in [7], meaning θ denotes the geographic longitude, and λ denotes the geographic latitude.

²Both R_N and R_M are readily found in relevant literature.

The vector \mathbf{p} is the position vector from the center of the ellipsoid to the reference point (θ_0, λ_0) given by

$$\mathbf{p} = \begin{bmatrix} R_N(\lambda_0) \cos(\lambda_0) \cos(\theta_0) \\ R_N(\lambda_0) \cos(\lambda_0) \sin(\theta_0) \\ R_N(\lambda_0) (1 - e^2) \sin(\lambda_0) \end{bmatrix} \quad (\text{A.6})$$

where e^2 is the squared first eccentricity of Earth, R_a is given in (A.2), and $\mathbf{u}|_{xyz}$ is the local "Up" vector (from ENU coordinates) converted to ECEF coordinates, which is found as

$$\mathbf{u}|_{xyz} = \mathbf{M}_{enu}^{xyz} \begin{bmatrix} 0 \\ 0 \\ 1 \end{bmatrix} \quad (\text{A.7})$$

It is straightforward to convert from SCH to ECEF coordinates as (A.1) through (A.7) only requires knowledge of the reference point (θ_0, λ_0) and the heading η_0 . However, for computing ranges and angles it is sufficient to convert to the intermediate rectangular coordinate system, (x', y', z') in (A.1), and perform calculations in this system [23].

A.2 ECEF to SCH

The inverse conversion from (x, y, z) -coordinates to (s, c, h) -coordinates is rather simple. From (A.3) it is seen that

$$\begin{bmatrix} x' \\ y' \\ z' \end{bmatrix} = (\mathbf{M}_{enu}^{xyz} \mathbf{M}_{x'y'z'}^{enu})^{-1} \left(\begin{bmatrix} x \\ y \\ z \end{bmatrix} - \mathbf{o}_{x'y'z'}^{xyz} \right) \quad (\text{A.8})$$

where $(\cdot)^{-1}$ is the matrix inverse. The intermediate coordinates can be referred back to (S, C, H) -coordinates according to (A.1). It can be shown that this involves a stepwise calculation, where first the c -coordinate is computed as

$$C = R_a \cdot \tan^{-1} \left(\frac{z'}{\sqrt{x'^2 + y'^2}} \right) \quad (\text{A.9})$$

and then the remaining two coordinates are given by

$$S = R_a \cdot \sin^{-1} \left(\frac{y'}{z'} \tan \left(\frac{C}{R_a} \right) \right) \quad (\text{A.10})$$

$$H = \frac{z'}{\sin \left(\frac{C}{R_a} \right)} - R_a \quad (\text{A.11})$$

